Important Notice

UNIVERSITY OF CALGARY

Prestack Vp/Vs scanning and automatic PS-to-PP time mapping using multicomponent seismic data

by

Osareni Christopher Ogiesoba

A THESIS

SUBMITTED TO THE FACULTY OF GRADUATE STUDIES
IN PARTIAL FULFILLMENT OF THE REQUIREMENTS FOR
THE DEGREE OF MASTER OF SCIENCE

DEPARTMENT OF GEOLOGY AND GEOPHYSICS

CALGARY, ALBERTA

DECEMBER, 2003

THE UNIVERSITY OF CALGARY

FACULTY OF GRADUATE STUDIES

The undersigned certify that they have read, and recommended to the Faculty of Graduate Studies for acceptance the thesis entitled "Prestack Vp/Vs scanning and automatic PS to PP time mapping using multicomponent seismic data " submitted by Osareni Christopher Ogiesoba in partial fulfillment of the requirements for the degree of Master of Science.

_____

Supervisor, R. R. Stewart, Geology and Geophysics

_____

L. R. Lines, Geology and Geophysics

_____

M. Lamoureux, Mathematics and Statistics

Date:

ABSTRACT

This thesis discusses the development, testing, and application of prestack methods that scan for the average vertical velocity ratio γ_0, and the stacking velocities of multicomponent seismic (MCS) data using a converted-wave (PS) non-hyperbolic traveltime equation. The procedure entails computing semblance as a function of two variables namely, the PS velocity Vps and γ_0, with respect to the PS zero-offset time t_{ps0}. The results are displayed in 2D and 3D plots. The scanning procedure is tested using numerical data sets and real MCS data sets from the Blackfoot Field in southern Alberta. The algorithms work well with either the shot gathers or the asymptotic conversion point (ACP) gathers. The accuracy increases with increasingly fine sampling of each variable. It is observed that the γ_0-log from the scanning procedure, agrees very well with the V_p/V_s values from the well log of Well-09-08. In addition, when this γ_0 estimate is used for PS-to-PP time mapping, the time difference between the computed and actual PP time at the target level is found to be 20 ms; being an error of less than 6%.

ACKNOWLEDGEMENTS

I would like to thank Dr. Rob R. Stewart for his guidance throughout the period of work. My thanks go to Kevin Hall for his systems support and to Gary Margrave for introducing me to Matlab computing. Finally, I am grateful to the students and other members of the CREWES Project and also, to the sponsors of CREWES.

TABLE OF CONTENTS

LIST OF TABLES AND FLOW CHARTS

LIST OF FIGURES

LIST OF SYMBOLS

γ_0	Average vertical velocity ratio
V_p/V_s	Average vertical velocity ratio
ε	Thomsen anisotropy parameter
δ	Thomsen anisotropy parameter
η	Effective anisotropy parameter defined by Alhkalifah and Tsvankin (1995)
σ	Thomsen anisotropy parameter
γ_{eff}	The parameter that controls PS propagation in layered media (Defined by Thomsen, 1999)
t_{p0}	P-wave zero-offset traveltime
t_{s0}	S-wave zero-offset traveltime
t_{ps0}	PS-wave zero-offset traveltime
V_{p0}	P-wave vertical average velocity
V_{s0}	S-wave vertical average velocity
V_{psrms}	PS-wave root mean square (RMS) velocity

V_{prms}	P-wave root mean square (RMS) velocity
V_{srms}	S-wave root mean square (RMS) velocity
V_p^{nmo} or simply V_p	P-wave moveout velocity (stacking velocity)
V_s^{nmo} or simply V_s	S-wave moveout velocity (stacking velocity)
V_{ps}^{nmo} or simply V_{ps}	PS-wave moveout velocity (stacking velocity)
PP	Incident P-wave to reflected P-wave
SS	Incident S-wave to reflected S-wave
PS	Incident P-wave to reflected S-wave.
t_{pav}	P-wave total one-way time
t_{sav}	S-wave total one-way time
t_{ps}	PS-wave total one-way time

Symbols not defined here but are used in this thesis, are defined wherever they occur.

Chapter 1

Introduction

1.1 Why converted-wave (PS-wave) exploration?

Since the beginning of exploration seismology, P-waves have been the main seismic method employed by the exploration seismologists in the search for hydrocarbons. There is no doubt that this method has been very successful. In fact, many of the world's hydrocarbon reservoirs that have been found to date have been discovered by the P-waves technique. In this regard, P-wave surveying will likely remain the dominant tool in the search for hydrocarbons for some time to come (Stewart et al., 2003). However, when it comes to determining the reservoir characteristics from seismic data, one finds that P-waves alone are often not adequate in providing all the answers. Also, now that the easy-to-find (structurally trapped) reservoirs, both on land (onshore) and shallow water environments have decreased, it has become apparently necessary to look for alternate methods to complement the P-wave method in our search for the stratigraphically trapped reservoirs both on land as well as the deep waters.

Explorationists have begun to find this complementary technique in the use of S-waves. The deliberate search for hydrocarbons using the S-waves method dates back to the early 1960's ((Tatham and McCormack, 1991; Garotta, 2000). Interpretation of S-wave data from Gardner and Harris (1968), relating V_p/V_s anomalies to gas saturation, and the experimental studies of Pickett (1963) relating V_p/V_s values to lithology, helped to fan the flames of S-waves exploration (Tatham and McCormack, 1991). By 1976, Conoco, in conjunction with three other companies formed a special S-wave exploration team; acquiring S-waves data using specialized S-waves sources, in the basins of Texas,

New Mexico, North Dakota, California, Wyoming, Oklahoma and Louisiana. Results of these surveys are reported in the literature (Ensley, 1984; Winterstein and Hanten, 1985; Roberson and Pritchett, 1985; Tatham, 1985; Tatham and Krug, 1985; Alford, 1986; Winterstein, 1986; Anno, 1987; Corbin et al., 1987).

Though the S-waves (SS) method offered some advantages such as shear-wave birefringence, shear-wave anisotropy and symmetric raypath geometry that facilitates CMP stacking, it was not very successful due to some associated problems. First, S-waves sources are expensive and scarce. Secondly, the method is not easily applicable in some environments such as marine, transition zones, muskeg and environmentally sensitive areas (Stewart et al., 2003). But what led to the P-S method of exploration? The answer to this question lies in the natural phenomenon of wave propagation; in acquiring P-waves data, the P-wave energy, propagating at an angle from the vertical, is partitioned, on impinging on an interface separating two layers of different elastic properties, into other wave types (Figure 1.1).

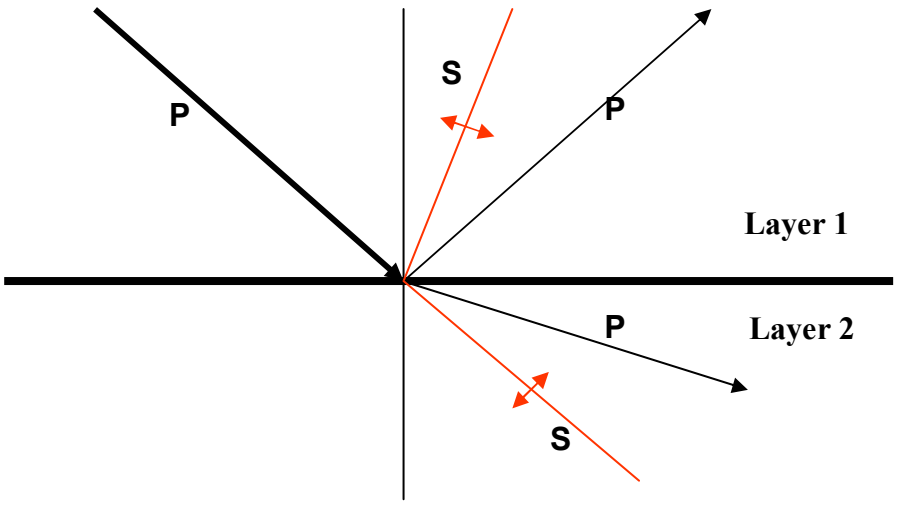

Figure 1.1. Incident P-wave is partitioned into reflected P-wave, refracted

P-wave, reflected and refracted S-waves energies.

Geophysicists exploited this phenomenon and developed 3-component sensors to record the S-wave events. This led to the P-S wave method. This partitioning of wave energy provides an inexpensive way of generating and recording S-wave data compared to SS-wave method that required specialized and expensive S-wave source-generating equipments. Furthermore, SS-wave seismic sections are often noisy and can have lower resolution. In addition to this, the SS recording times are about double or triple those of P-waves and some 30% longer than PS waves (Stewart et al., 2003). All put together, S-waves surveys usually cost more than PS acquisition (Kendall and Davis, 1996). This is not all; with the multicomponent recording, both P- and PS-waves data are acquired simultaneously (Tatham and McCormack, 1991); the two sets of data can be used to address a variety of interpretational problems.

So what are the benefits accruing from converted (PS) waves. Several workers have considered the benefits of using converted waves notably (Tatham and McCormack, 1991, Garotta, 2000; Stewart et al., 2003). In addressing the merits of PS method, Stewart et al., 2003; Garotta, 2000, noted that this is inherently linked to the different mode of propagation of the P- and S-waves; the physical entity (the divergence of the vector displacement) that actually propagates as the P-wave in isotropic medium is a scalar quantity, while the physical entity (the curl of the vector displacement) that propagates as the S-wave, is a vector quantity. Thus, the S-wave may inherently contain more information than the P-wave (Tatham and McCormack, 1991). This implies that recording both wave modes together invokes a situation akin to using multiple simultaneous equations, and hence we can address multiple unknowns.

From the foregoing, the PS-wave method can, in conjunction with P-wave technique, be used in solving several exploration problems which, hitherto could not be addressed with the P-wave alone. What are these exploration problems? Many authors (e.g.; Garotta, 2000, Kristiansen, 2000, Stewart et al., 2003) have discussed the application of converted-waves; these include but not limited to:

- Imaging shale diapirs, and mud volcanoes, reflectors within and beneath gas-bearing sediments and targets beneath salt bodies and basalt layers
- Imaging interfaces with low P-wave impedance contrast but significant S-wave impedance change
- Using P-S attributes and interval V_p/V_s analysis for lithology discrimination (e.g., sand/shale, dolomite/anhydrite)
- Investigating anisotropy for improved processing as well as for revealing fracture density and orientation

Many of these benefits are either proven or considered possible (Stewart, et al., 2003). In this thesis, an example of imaging due to higher velocity contrast is discussed.

Sand-shale boundaries may produce poor P-wave velocity contrast; while there can be significant S-wave velocity contrast. This is the case for the Alba turbidite channel reservoir in the North Sea, shown in Figures 1.2a and 1.2b. The top of the reservoir could not be seen clearly with the P-wave reflections. However, the P-wave sonic does appear to identify the interpreted oil-water contact. The S-wave sonic on the other hand, clearly shows the top of the reservoir suggesting a lithology change at this level. Because of the higher shear mode contrast, a PS-wave data was acquired by the operating company (Macleod et al., 1999b). The comparison in Figure 1.2b shows the usefulness of PS-wave

exploration in delineating reservoir boundaries. In this Figure, the reservoir boundary is at about 4.0 seconds PS time (Macleod et al., 1999b).

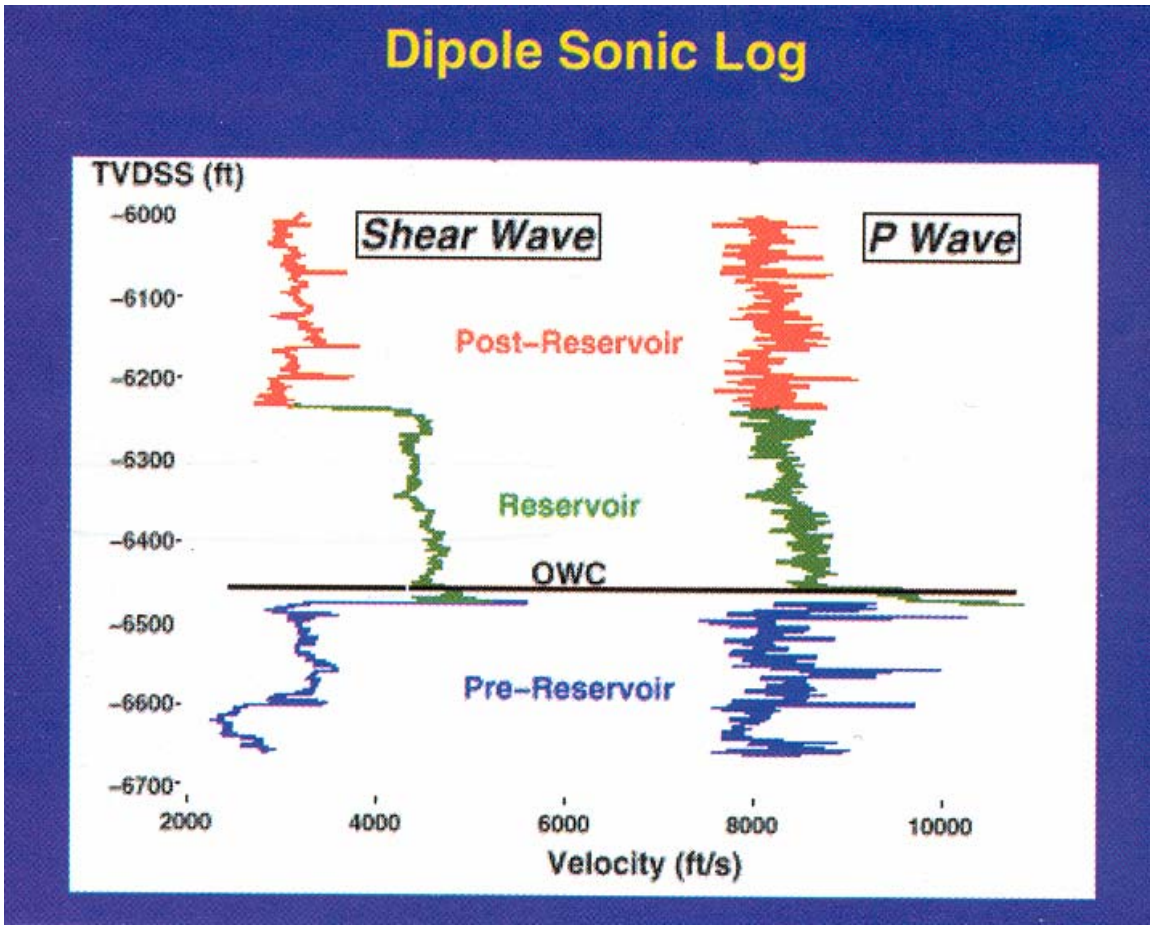

Figure. 1.2a. The S-wave sonic shows higher velocity contrast than the P-wave sonic at the top of the reservoir (Macleod et al., 1999b)

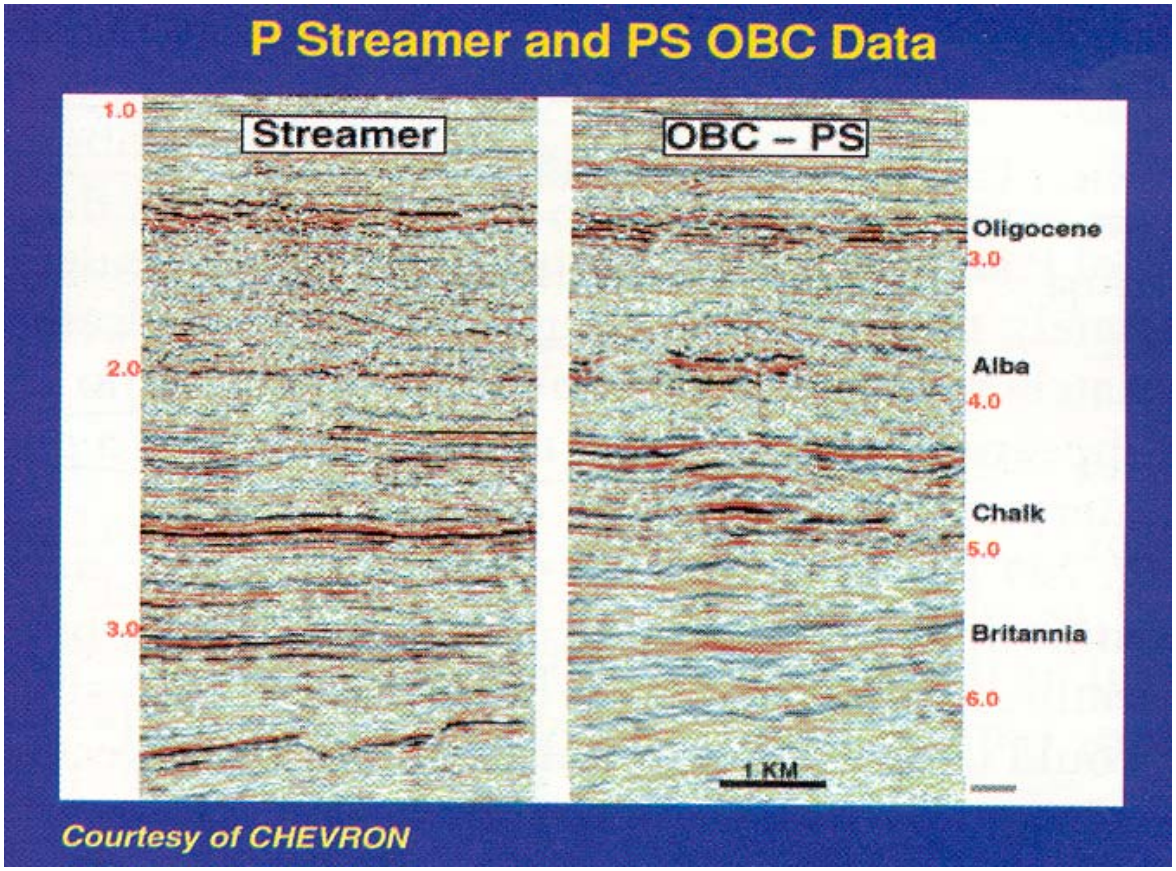

Figure. 1.2b. The PS data clearly outlines the reservoir at about 4.0 seconds PS time. (Macleod et al., 1999b).

Although the several benefits of PS-wave exploration makes it very appealing to the exploration community, it is saddled with several major challenges; one of these, if not correctly tackled, would render PS-wave exploration a tantalizing mirage. This problem is the asymmetrical ray-path geometry of PS-wave reflection which makes PS moveout gather formation for the purpose of velocity analysis a difficult task. Unlike the P-wave (PP) ray-path that is symmetric about the reflection point, the PS ray-path is not. An additional difficulty is that, transforming the PS stacked data to P-wave times for the purpose of correlation and interpretation is not straight forward because the parameter

with which to transform is usually not known; using the wrong parameter could lead to incorrect interpretations. This parameter is known as the average vertical velocity ratio γ_0. Because of the strategic importance of γ_0 in PS-wave exploration, finding γ_0 constitutes a crucial step in converted-wave data processing and interpretation. To give an insight into how PS moveout depends on γ_0, the fundamentals of PS-wave exploration is discussed hereunder.

1.2 Fundamental of PS-wave exploration

Some authors (e.g., Nefedkina, 1980; Behle and Dohr, 1985; Chung and Corrigan, 1985; Frasier and Winterstein, 1986; Tessmer and Behle, 1988; Yilmaz, 2001), have discussed the geometry of PS-wave raypath and the problems associated with the gathering of converted-wave data of common conversion points. As shown in Figure 1.3, there are two reflection arrivals at the receiver location R associated with the P-wave and PS raypaths. The reflection point C at which the P-wave is converted to S-wave is displaced in the lateral direction by some distance *d* away from the reflection point M, where the P-wave is reflected and is recorded by the same receiver R as the converted S-wave (Figure 1.3). This implies that, for a horizontally layered earth model, the P-wave reflection points coincide with the midpoint location M (Figure 1.4); while in the case of the PS-wave, the conversion points do not. Rather, the points follow a curved trajectory (Figure 1.5). Consequently, CMP sorting that is applicable to P-wave survey, in which traces in the same gather have the same midpoint coordinate, does not apply to PS-wave survey.

Binning the PS data into common conversion point CCP, (i.e. depth-dependent γ_0 binning) gathers requires knowledge of the conversion-point coordinate X_c (Appendix 1). The expression for the conversion point can be written as (Yilmaz, 2001):

$$X_c = \frac{\sqrt{\gamma_0^2 + (\gamma_0^2 - 1)\frac{X_c^2}{Z^2}}}{1 + \sqrt{\gamma_0^2 + (\gamma_0^2 - 1)\frac{X_c^2}{Z^2}}} X , \qquad (1.1)$$

where,

Xc = the conversion point coordinate distance from the source,

Z = depth from surface to the reflector,

γ_0 = average vertical velocity ratio, and

X = offset distance (distance between the shot S and receiver R).

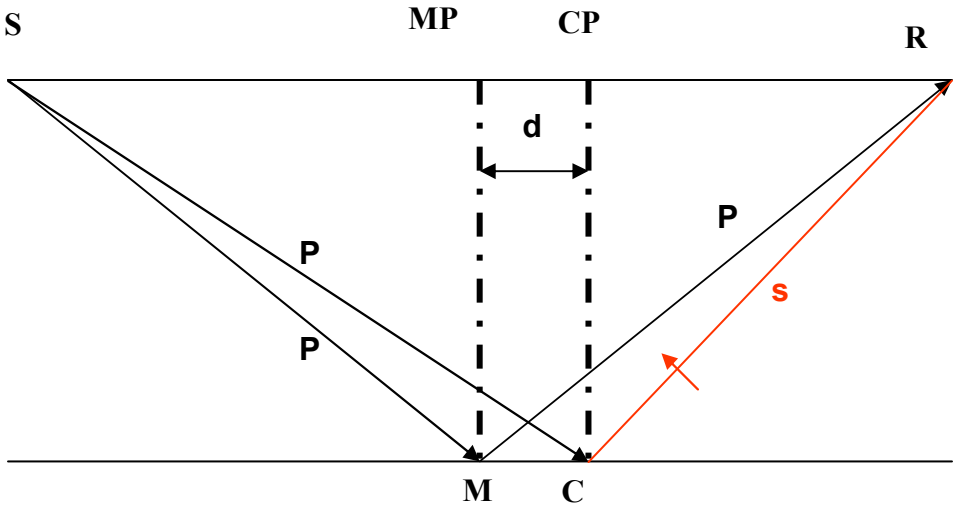

Figure 1.3. PP and PS raypath; the red line shows the S-wave converted from P-wave (red arrow indicate first motion for impedance increases). MP is the midpoint, while CP is the conversion point; i.e., point at which the P-wave is converted to S-wave.

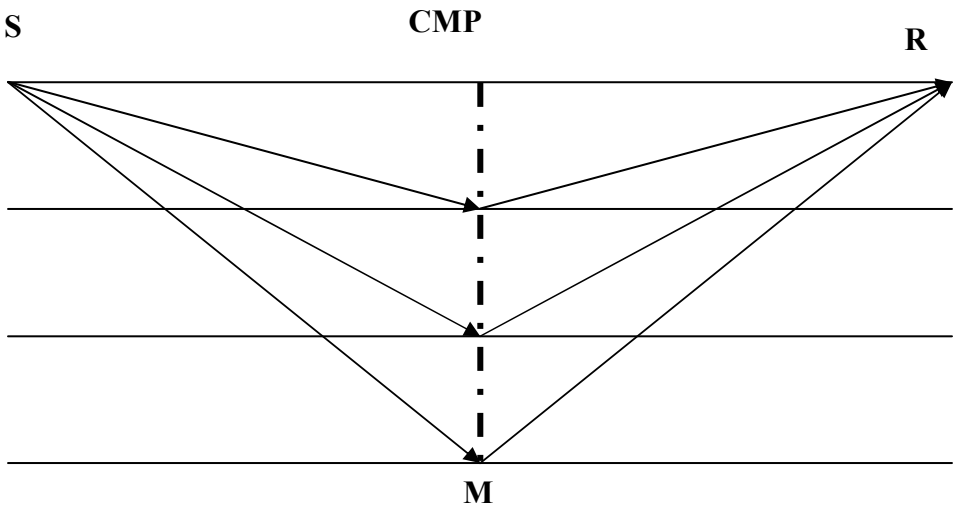

Figure 1.4. Traces in CMP gather have common midpoint.

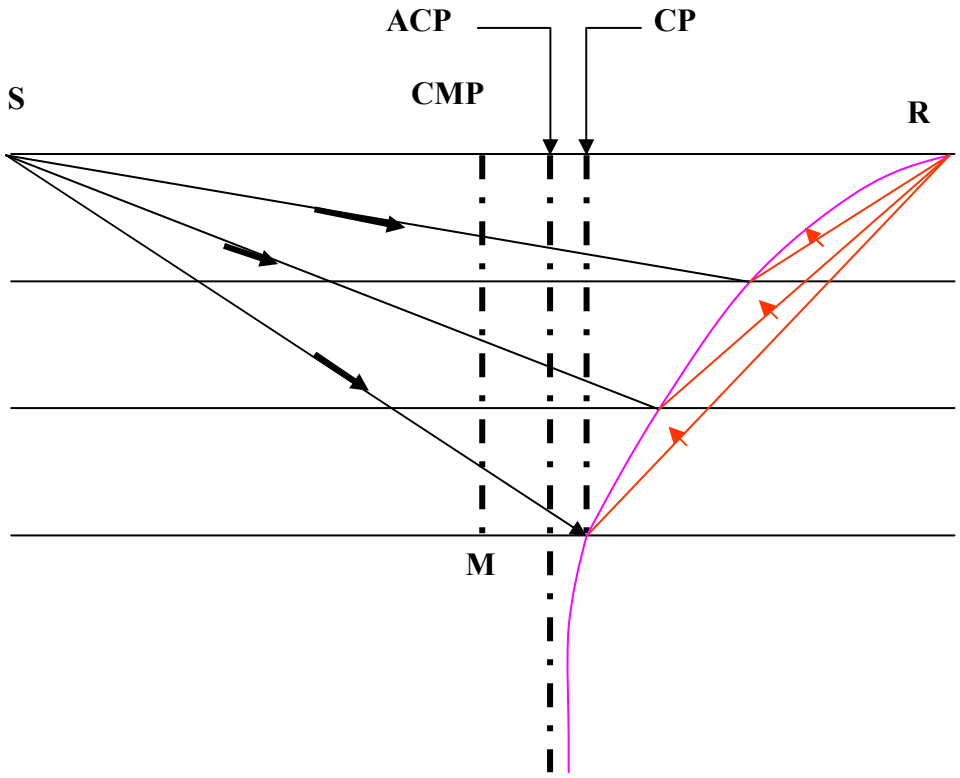

Figure 1.5. The conversion (PS reflection) point follows a curved trajectory

At infinite depth, the CP location reaches an asymptotic conversion point (ACP) (Fromm et al., 1985). In the limit as $Z \to \infty$, equation (1.1) gives the ACP coordinate X_c with respect to the source location:

$$X_c = \left(\frac{\gamma_0}{1+\gamma_0} \right) X . \qquad (1.2)$$

CCP binning can be performed using ACP coordinate given by equation (1.2). However, more accurate result will be obtained using equation (1.1) (Tessmer and Behle, 1988; Zhang and Robison, 1992). For CCP binning, X_c depends on γ_0 and depth; while for the ACP, X_c depends on γ_0 only. In both cases, the importance of γ_0 can clearly be seen. Yilmaz (2001) noted that unless a value of γ_0 is assumed, CCP binning requires velocity analysis of PS data to determine γ_0. To perform PS-wave velocity analysis, an appropriate PS-wave traveltime equation is a must. A PS-wave traveltime equation as derived by Yilmaz (2001) is reviewed in Appendix 1. In Chapter 2, a PS traveltime equation in homogeneous and isotropic media based on Tsvankin and Thomsen (1994) formulation is discussed; also, the validity as well as the sensitivity of the derived equation are presented. Also addressed in this chapter, is the dual-parameter-scanning algorithm development. Finally, the application of the scanning code using numerical examples is presented. The Chapter ends with a summary of the main points.

In Chapter 3, I discuss the application of the method using real data sets from the Blackfoot oil field in southern Alberta. The values of scanned velocity ratios are compared with well log results. Chapter 4 focuses on the conclusions and discussions from the body of this thesis.

1.3 Hardware and software used.

The work presented in this thesis was generated on a Sun Microsystems network owned and operated by the CREWES Project of the Department of Geology and Geophysics at the University of Calgary. Seismic data processing was carried out in Promax environment; while the numerical models were created using the GX2 raytracing package at the CREWES Project, and the ANIVEC (a frequency-wave number based modeling package) used at WesternGeco, Denver. The two algorithms developed in this thesis and other necessary codes utilized in this work were written in Matlab; applications of the algorithms and PS to PP mapping were executed in Matlab. Figures were also generated in Matlab. These were screen-captured using XV and Matlab figure exporting utility. Figure editing was performed using Microsoft Power Point; while Microsoft Word was used for the documentation.

Chapter 2

Converted-wave (PS) Traveltime Equations and Vps-γ_0 Scan

2.1 Introduction

In the introductory section of this thesis, the need for PS-wave exploration and its fundamentals were discussed. It was noted that PS-wave methodology does offer several benefits; but certain problems, such as determining γ_0, stand between us and the realization of these many advantages. Because of this, recovery of γ_0 has become a crucial step in multi-component data processing and interpretations. Several authors have used different methods for the recovery of γ_0; for example, Gaiser (1996) developed a post-stacked cross-correlation method. The method is automatic and is based on correlating PP and PS stacked data sets. Thomsen (1999) suggested visually correlating events of the same structural attitude on both PP and PS stacked section; this too, is also a post-stack method. Li et al. (1999; 2001) attempted using a prestack method via velocity analysis but concluded that it was not possible to recover γ_0 using semblance analysis. Stewart et al. (2003) alluded to a time-isochron method using interpreted PP and PS sections. Like Gaiser's method, this too is a post-stack method that depends on correlating PP and PS events. The post-stack methods can work well but may fail with complicated sections, when PP and PS data have very different wavelets, or events of opposite polarity. And as noted by (McCormark et al., 1984; Garotta, 1985; Tessmer and Behle, 1988), these post-stack methods can introduce errors due to miscorrelation. For example, problems caused by different tuning effects with respect to thin beds for different wave types can lead to miscorrelation of PP and PS stacked data sets. Furthermore, effects of anisotropy and insufficient S-wave static corrections can as well

lead to miscorrelation (Tessmer and Behle, 1988). Also, in areas of flat-lying geology, like in Western Canada, events can look the same. Also, different statics and datums may significantly shift the sections from each other; therefore, recognizing similar structures on the PP and PS sections becomes a problem. In view of these, there is need to find an alternate prestack solution to the problems associated with P- and PS-wave correlation. In this chapter, I present a prestack method of estimating γ_0 via velocity analysis using a converted-wave, non-hyperbolic traveltime equation. In Chapter 1, I briefly touched on the importance of γ_0 in multicomponent seismic exploration. Discussed hereunder is an overview of γ_0 and its relationship with some isotropic and anisotropic parameters.

2.2 Average vertical velocity ratio γ_0 and its role in PS-wave exploration

2.2.1 Definition of γ_0

The average vertical velocity γ_0 is defined as the ratio of the average P-wave velocity to the average S-wave velocity, measured at zero-offset time for a given reflector depth (Garotta, 2000).

Mathematically, it is expressed as:

Tessmer and Behle (1988), Thomen (1999), $$\gamma_0 = \frac{V_{p0}}{V_{s0}}. \qquad (2.1)$$

where V_{p0} and V_{s0} are respectively the average P-wave and S-wave velocities at zero-offset time. In the pure-mode case and for a given reflector (Thomsen, 1999; Garotta, 2000), we have:

$$\gamma_0 = \frac{t_{s0}}{t_{p0}}, \qquad (2.2)$$

where t_{p0} and t_{s0} are respectively the P-wave and the S-wave zero-offset traveltimes.

In the PS-mode case (Tessmer and Behle, 1988; Yilmaz, 2001), [Appendix 1]:

$$\gamma_0 = \left(\frac{2t_{ps0}}{t_{p0}} \right) - 1, \tag{2.3}$$

where t_{ps0} is the PS-wave zero-offset traveltime.

2.2.2 The role of γ_0 in PS-wave exploration

The importance of γ_0 in PS-wave exploration cannot be over-stressed. It determines the location at which the P-wave converts to S-wave. Thus it dictates the emergence distance (offset) in multicomponent data acquisition. In anisotropic media, it combines with ε and δ to control the conversion point location (Yang and Lawton, 2001). However, it alone acts as the parameter with which to transform PS stacked data to P-wave times and vice versa; whether isotropic or anisotropic. While γ_0 acts as independent parameter, some, if not all vertical traverse isotropy (VTI) parameters depend on it. The following expressions attest to this statement:

$$\gamma_{eff} = \frac{\gamma_2^{\,2}}{\gamma_0}, \tag{2.4}$$

where, γ_{eff} is the parameter that controls PS-wave propagation in layered media (Thomsen, 1999); and γ_2 is expressed as:

$$\gamma_2 = \frac{V_p^{\,nmo}}{V_s^{\,nmo}}, \tag{2.5}$$

where V_p^{nmo} and V_s^{nmo} are respectively the P-wave and S-wave moveout velocities (stacking velocities). But since V_s^{nmo} cannot be directly measured during PS-wave acquisition, γ_{eff} has to be found by some other ways; thus, Thomsen (1999) derived:

$$\gamma_{eff} = \left((1+\gamma_0) \left(\frac{(V_{ps}^{nmo})^2}{(V_p^{nmo})^2} \right) - 1 \right)^{-1}, \tag{2.6}$$

where, V_{ps}^{nmo} and V_p^{nmo} are respectively the PS- and P-wave moveout velocities. Therefore, $\gamma_{eff,}$ which accounts for the effects of layering on PS-wave propagation in layered media, depends on γ_0. Also, considering the S-wave VTI parameter σ, Tsvankin and Thomsen (1994) showed that it can be written as

$$\sigma = \gamma_0^{\,2}(\varepsilon - \delta), \tag{2.7}$$

where, ε is the VTI parameter that controls the P-wave horizontal velocity, and δ is the parameter that controls the P-wave near vertical velocity. Tsvankin and Alkhalifah (1995) showed that the VTI parameter (effective anisotropy parameter) η that controls P-wave propagation is written as:

$$\eta = \frac{(\varepsilon - \delta)}{(1+2\delta)}, \tag{2.8}$$

Li et al. (1999) showed that the effective anisotropy parameter η can be written as:

$$\eta = \frac{\sigma}{\gamma_2^{\,2}(1+2\sigma)}, \tag{2.9}$$

where, all other parameters are as defined above. Combining equations (2.4) and (2.7) to (2.9), gives:

$$\sigma = \frac{\gamma_0 \gamma_{eff} \eta}{(1 - 2\gamma_0 \gamma_{eff} \eta)}, \tag{2.10}$$

Following Li et al. (1999), equation (2.9) can be expressed as:

$$\eta = \frac{\gamma_0^{\,2}(\varepsilon - \delta)}{\gamma_2^{\,2}(1 + 2\gamma_0^{\,2}(\varepsilon - \delta))}. \tag{2.11}$$

Dividing the numerator and the denominator of the right hand side of equation (2.11) by (1+2δ) we have,

$$\eta = \frac{\gamma_0^{\,2}\eta}{\gamma_2^{\,2}(\frac{1}{1+2\delta} + 2\gamma_0^{\,2}\eta)}. \tag{2.12}$$

By making the assumption that $\delta << 1$ (weak anisotropy), so that:

$$\frac{1}{(1+2\delta)} \cong 1, \tag{2.13}$$

and also using equation (2.4), equation (2.12) becomes,

$$\eta \cong \frac{\gamma_0 - \gamma_{eff}}{2\gamma_0^{\,2}\gamma_{eff}}. \tag{2.14}$$

From the foregoing, it can be seen that most VTI parameters depend on γ_0.

PS-wave capability in determining lithology, and anisotropy alluded to in the introductory section of this thesis, is directly related to the variations in the physical parameter γ_0. Several case studies dealing with the use of γ_0 variation in lithologic identification, reservoir pay thickness, and anisotropy determinations, have been reported in the literature (Jolly, 1956; Toksoz et al., 1976; Lash, 1980; Banik, 1984; Ensley, 1984; McCormark et al., 1985; Robertson et al., 1985; Tatham and Krug, 1985; Tatham, 1985; Corrigan et al., 1986; Winterstein, 1986; Robertson, 1987; Pardus et al., 1990; Stewart et al., 2003). Tsvankin and Alkhalifah (1995) reported on the use of η in identifying

reservoir sands in offshore Zaire. That this is possible can be seen directly from equation (2.14) in which, η depends entirely on γ_0.

By rearranging equation (2.3), Tessmer and Behle (1988) and Yilmaz (2000) showed that (Appendix 1):

$$t_{p0} = \frac{2t_{ps0}}{1+\gamma_0}. \qquad (2.15)$$

Thus, knowing the γ_0 function, equation (2.15) provides the means by which, PS-wave stacked data can be transformed to P-wave times. From the foregoing, the importance of γ_0 in multi-component seismic data can clearly be seen; but how do we recover it robustly from moveout analysis? This is the challenge that I will address in the following section.

2.3 Converted-wave traveltime equation in homogeneous and isotropic media

In Appendix 1, I reviewed the PS-wave double square root (DSR) traveltime equations developed by Yilmaz (2001). These equations expressed PS traveltime in terms of S- and P-wave velocities and do not contain the PS-wave stacking velocity. Tsvankin and Thomsen (1994) developed PS-wave traveltime equation that is applicable to homogeneous, isotropic and anisotropic media from which the PS-wave stacking velocities can be derived. In this thesis, I closely follow their development to derive a dual-parameter scanning algorithm that can be used to scan for the PS-wave stacking velocities as well as the velocity ratios γ_0.

According to Tsvankin and Thomsen (1994), the PS-wave traveltime equation can be written as:

$$t_{ps}{}^{2}(x) = t_{ps0}{}^{2} + \frac{x^2}{V_{ps}{}^{nmo^2}} + \frac{A_4 x^4}{1 + A_5 x^2}, \tag{2.16}$$

where, x = offset, and A_4 and A_5 are coefficients that relate to the medium; all other variables are as defined previously. Thomsen (1999) showed that in a homogeneous and isotropic medium, the coefficients A_4 and A_5 can be approximated as:

$$A_4 = \frac{-(\gamma_0 - 1)^2}{4(\gamma_0 + 1) t_{ps0}{}^{2} V_{ps}{}^{nmo^4}}, \tag{2.17}$$

$$A_5 = \frac{-A_4 V_{ps}{}^{nmo^2}}{(1 - \frac{V_{ps}{}^{nmo^2}}{V_p{}^{nmo^2}})}, \tag{2.18}$$

Combining equations (2.16) to (2.18) yields Thomsen (1999):

$$t_{ps}{}^{2}(x) = t_{ps0}{}^{2} + \frac{x^2}{V_{ps}{}^{nmo^2}} - \left(\frac{(\gamma_0 - 1)^2 (V_p{}^{nmo^2} - V_{ps}{}^{nmo^2})}{4(V_p{}^{nmo^2} - V_{ps}{}^{nmo^2})(\gamma_0 + 1) t_{ps0}{}^{2} V_{ps}{}^{nmo^4} + (\gamma_0 - 1)^2 V_p{}^{nmo^2} V_{ps}{}^{nmo^2} x^2} \right) x^4 . \tag{2.19}$$

It is impracticable to use equation (2.19) for velocity analysis since it contains three unknown variables: $V_p{}^{nmo}$, $V_{ps}{}^{nmo}$, and γ_0. Thus, to simplify the expression, I utilized the Tessmer and Behle (1988) approximation:

$$V_{ps}{}^{nmo^2} \cong \frac{V_p{}^{nmo^2}}{\gamma_0}, \tag{2.20}$$

Equation (2.20) is based on the assumption of horizontally layered and isotropic earth; and $V_p{}^{nmo}$ and $V_{ps}{}^{nmo}$ are respectively the P- and PS-wave moveout velocity. Though this is an approximation, it does give an error of less than 10% in some PS-wave velocity tests (Li et al., 2001). Substituting (2.20) into (2.19) gives:

$$t_{ps}{}^{2}(x) = t_{ps0}{}^{2} + \frac{x^2}{V_{ps}{}^{nmo^2}} - \left(\frac{(\gamma_0 - 1)^2}{4(\gamma_0 + 1)t_{ps0}{}^{2}V_{ps}{}^{nmo^4} + \gamma_0(\gamma_0 - 1)V_{ps}{}^{nmo^2}x^2} \right), \qquad (2.21)$$

Can equation (2.21) be used effectively to describe converted-wave (PS-wave traveltimes)?

2.4 Validity of PS traveltime equation

I tested the validity of the derived traveltime equation by first creating model synthetic seismic records from ANIVEC. The model consists of a single-layer isotropic medium Figure 2.1. The synthetic seismic records obtained are shown in Figure 2.2. To see how the synthetics generated using equation (2.21) compare with those from ANIVEC, I adopted the following procedure:

1. First generate a wavelet using some dominant frequency.
2. Compute traveltimes employing the derived equations and using the following parameters that were obtained from the models :

(a) zero offset-times t_{ps0} from the various layers,

(b) the V_{ps} associated with the layers,

(c) the velocity ratios to each layer,

(d) and the offset values.

3. Next assign the wavelet amplitude to the computed traveltimes. Here, in this case, the wavelet amplitude represents the reflectivity.
4. Finally, plot the seismic traces.

The results of the above procedure are shown in Figures 2.2 and 2.3. Figure 2.3 shows the superposition of the traces from ANIVEC shown in black, over the traces generated using equation (2.21). The match is quite reasonable even at the far offsets.

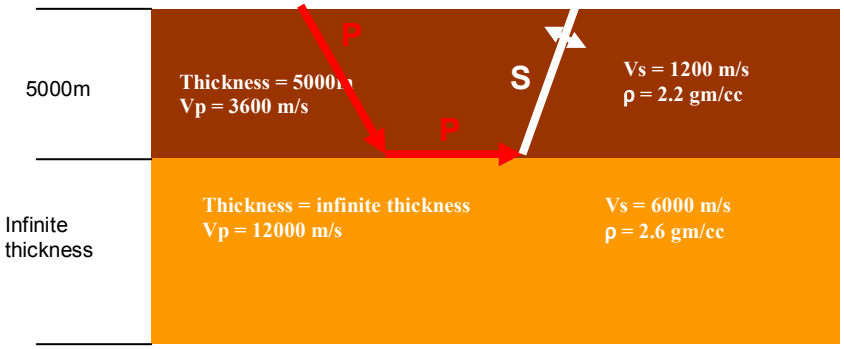

Figure 2.1. Geologic model used in testing equation (2.21)

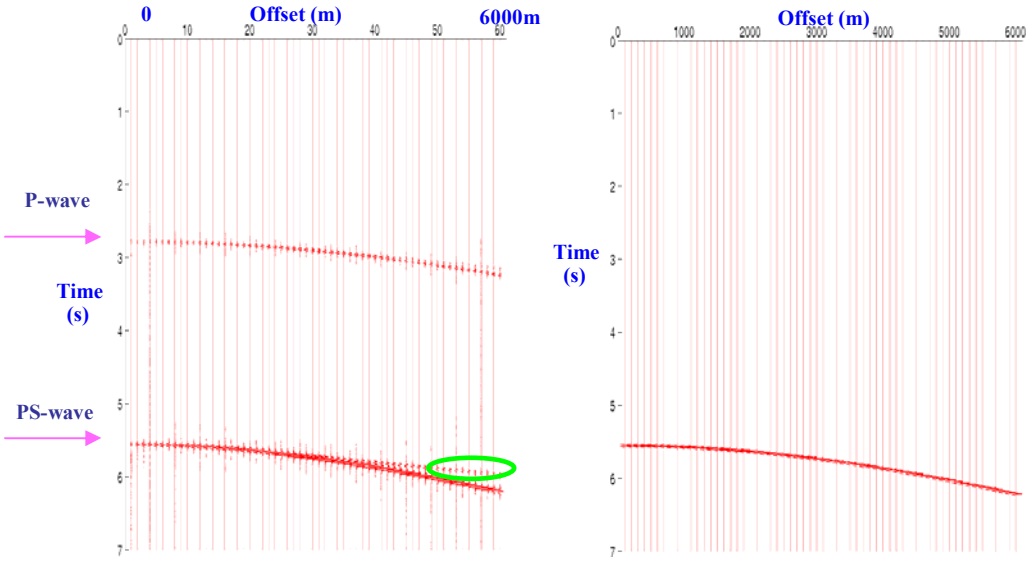

Figure 2.2. Shown above, are the shot records (horizontal component) from the ANIVEC modeling package (left), and (right) the synthetic seismograms from equation (2.21). The event circled in green is a P-P-S-wave refracted event with a moveout velocity of about 11520 m/s. (i.e. P-wave refracted event that is delayed by the S-wave velocity; see Figure 2.1 for explanation) The P-wave primary event occurs at 2.78 sec.

Also, the numerical traveltime values from ANIVEC and the synthetic obtained using equation (2.21) are compared in Tables 2.1 and 2.2. Table 2.1 shows the comparison of traveltimes for the first 10 offsets, while Table 2.2 shows the comparison for the last 10 offsets. The average percentage error between the traveltimes obtained using equation (2.21) and those from ANIVEC for the first 10 offsets is 0.04%; while the error from the last 10 offsets is 0.4%. This comparison shows that the values from equation (2.21) and those from ANIVEC are quite close.

2.5 Sensitivity test

Having tested the validity of the traveltime equation for this straightforward case, a sensitivity analysis was carried out to see how the variations in γ_0 and V_{ps} affect moveout. This test was performed by generating traveltime curves, first at constant γ_0 while varying the PS-wave velocity; and secondly, by fixing the PS-wave velocity and varying γ_0. The results of this test are shown in Figure 2.4. From this Figure, it can be seen that moveout changes significantly with variations in velocity. On the other hand, the changes in moveout due to γ_0 variations are less dramatic compared to those observed in velocity variations. This implies that moveout is more sensitive to velocity than γ_0. In spite of this, moveout still has enough sensitivity due to γ_0 variations to be exploited to scan for γ_0 via velocity analysis.

Also, the changes in the P-wave and S-wave velocities under the above two conditions were investigated using equation (2.20). It was found that at constant γ_0 value but varying V_{ps}, both the P-wave and S-wave velocities increase gradually as V_{ps} increases, (Table 2.3 and Figure 2.5). On the other hand, at constant PS-wave velocity but

varying γ_0 value, the P-wave velocities still show a gradual increase as γ_0 increases, but the S-wave velocities show a gradual decrease as γ_0 increases (Table 2.4 and Figure 2.5). The behavior of these curves is dependent on equation (2.20).

Table 2.1. Comparison of traveltimes: from ANIVEC and equation (2.21) for the first 10 offsets. Average error is -0.04%

Method	Offset 1	Offset 2	Offset 3	Offset 4	Offset 5	Offset 6	Offset 7	Offset 8	Offset 9	Offset 10
Eqn. (2.21)	5.5558	5.5564	5.5575	5.5589	5.5608	5.5631	5.5658	5.5689	5.5724	5.5764
ANIVEC	5.5720	5.5760	5.5760	5.5760	5.5800	5.5840	5.5880	5.5920	5.5960	5.6000

Table 2.2. Comparison of traveltimes: from ANIVEC and equation (2.21) for the last 10 offsets. Average error is -0.4%

Method	Offset 1	Offset 2	Offset 3	Offset 4	Offset 5	Offset 6	Offset 7	Offset 8	Offset 9	Offset 10
Eqn. (2.21)	6.0508	6.0687	6.0868	6.1052	6.1238	6.1426	6.1616	6.1809	6.2003	6.2199
ANIVEC	6.2520	6.2800	6.3040	6.3320	6.3600	6.3840	6.4120	6.4400	6.4680	6.4960

Table 2.3. Variation of V_p and V_s due to the variation of V_{ps} but constant γ_0

γ_0	P-wave velocities from varying V_{ps} (m/s)				S-wave velocities from varying V_{ps} (m/s)			
2.2	1187	2453	2483	3073	539	1115	1128	1397
2.8	1339	2767	2800	3466	478	988	1000	1238
3.0	1386	2864	2899	3588	462	955	966	1196
4.0	1600	3307	3347	4143	400	827	837	1036
V_{ps} =	800	1654	1674	2071	800	1654	1674	2071

Table 2.4. Variation of V_p and V_s due to the variation of γ_0 but constant V_{ps}

V_{ps}	P-wave velocities from varying γ_0				S-wave velocities from varying γ_0			
800	1187	1339	1386	1600	539	478	462	400
1653.5	2453	2767	2864	3307	1115	988	955	827
1673.5	2482	2800	2899	3347	1128	1000	966	837
2071.6	3073	3466	3588	4143	1397	1238	1196	1036
γ_0 =	2.2	2.8	3.0	4.0	2.2	2.8	3.0	4.0

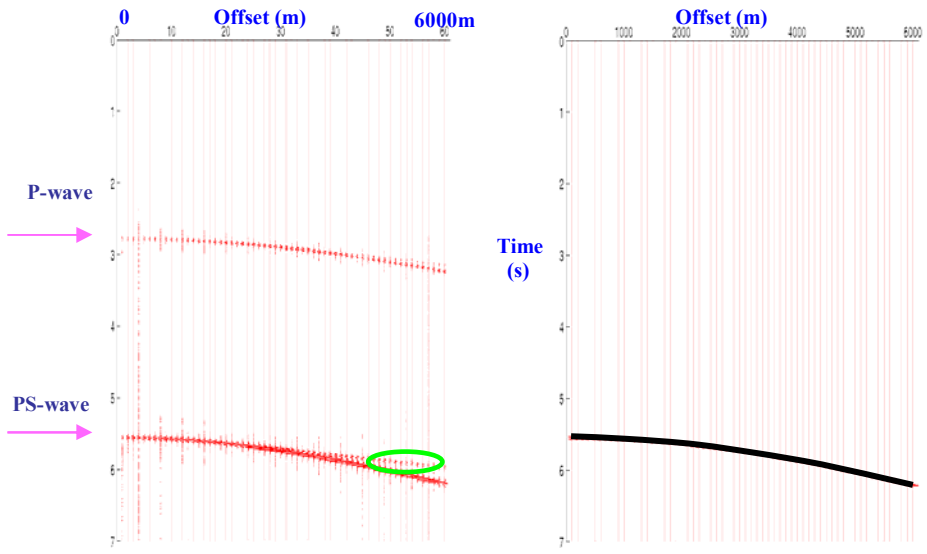

Figure. 2.3. Comparison of the shot record from ANIVEC (left) with the synthetic record from equation (2.21) (right). The black curve is the digitized curve from ANIVEC shot record. The fit is reasonable even at the far offsets. The event circled in green is a P-wave first multiple.

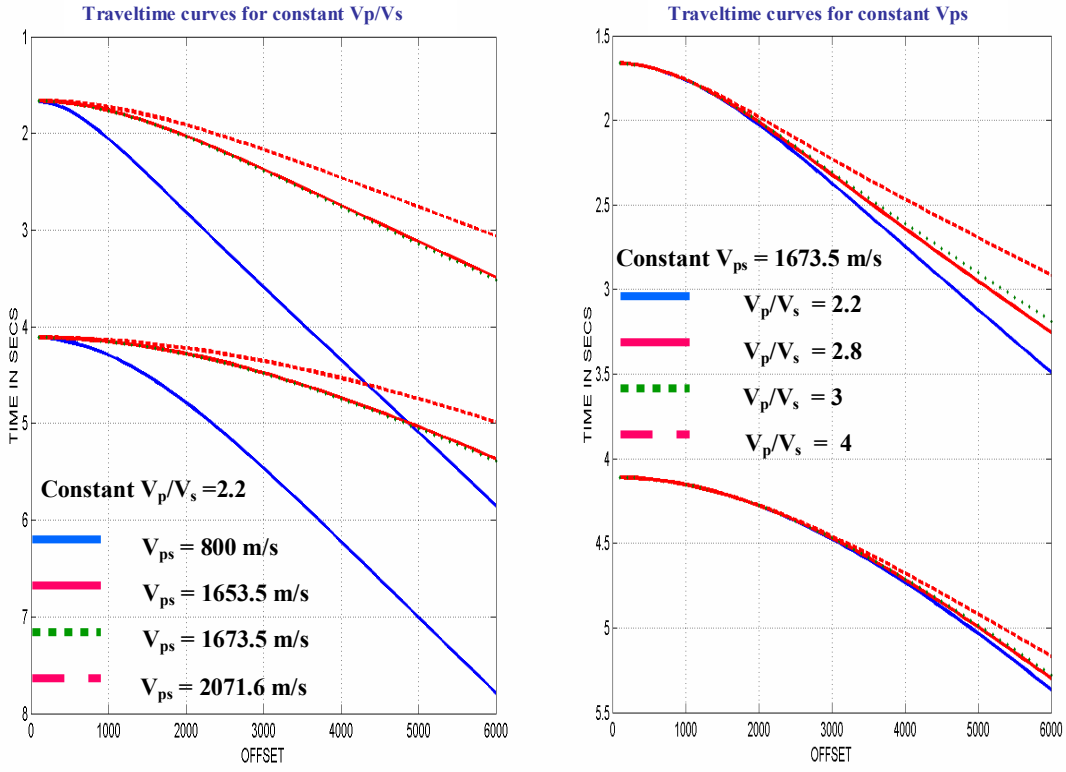

Figure 2.4. Sensitivity test: on the left are traveltime curves for variable velocities with fixed γ_0; while the graph to the right, shows traveltime curves for variable γ_0 with fixed velocity. Doubling V_{ps} causes considerable change in V_p and V_s; but doubling γ_0 causes much less change in V_p and V_s (see Figure 2.5)

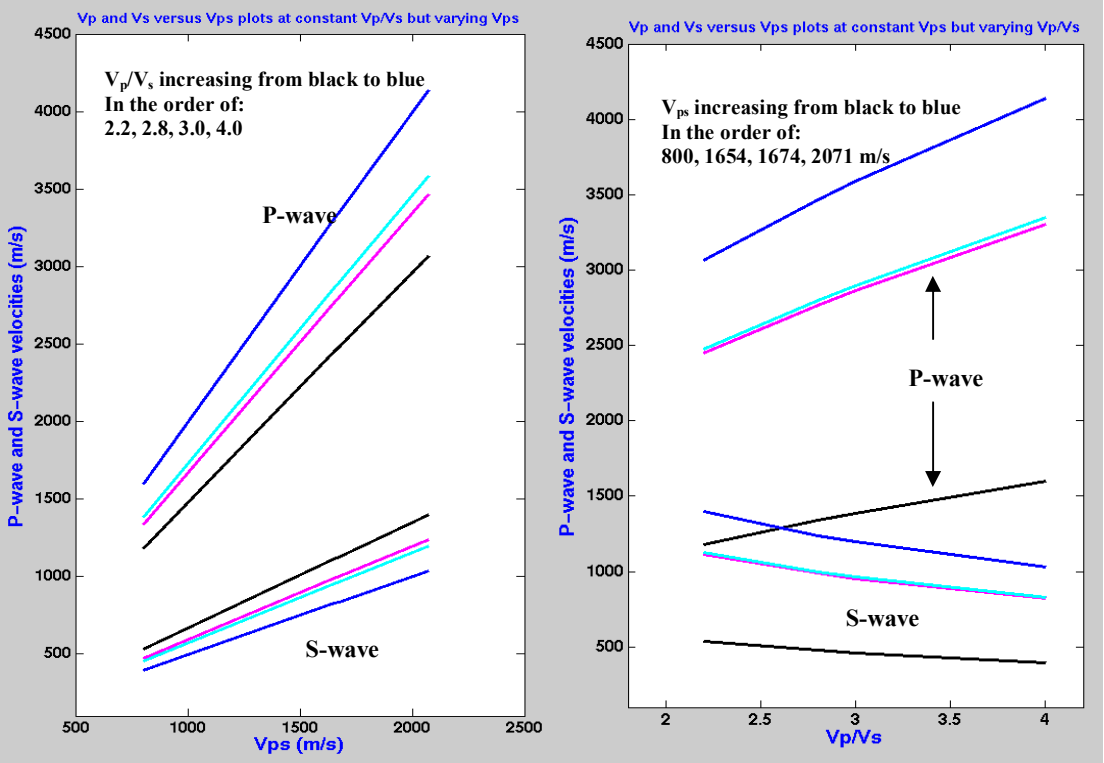

Figure 2.5. Plots of V_p and V_s versus V_{ps}; and V_p and V_s versus V_p/V_s.

On the left, the plots of the computed P- and S-wave velocities are plotted against PS-wave velocities. The velocity values were obtained by fixing γ_0 and varying V_{ps} . The graph to the right shows the plots of the computed P- and S-wave velocities plotted against γ_0 values. The velocity values were obtained by fixing V_{ps} and varying γ_0.

2.6 Dual-parameter scanning algorithm development and the scanning procedure

Two schemes are described; both are based on the same concept but one is slightly modified. Common to both schemes is the semblance computational method in which semblance is computed as a function of three variables namely: V_{ps}, γ_0, and PS-wave

zero-offset traveltime t_{ps0}. Below is a review of semblance analysis as formulated by Tanner and Koehler (1969) incorporating equation (2.21).

2.6.1 Semblance computation

The semblance coefficient is a statistical measure introduced into velocity analysis by Taner and Koehler (1969). Simply stated, it is defined as the normalized output/input energy ratio, where the output trace is a simple compositing or sum of the input traces (Neidell and Taner, 1971). Mathematically, the semblance coefficient SC can be stated as:

$$SC = \frac{\sum_{j=k-(N/2)}^{k+(N/2)} \left(\sum_{i=1}^{M} f_{i,j(i)} \right)}{M \sum_{j=k-(N/2)}^{k+(N/2)} \sum_{i=1}^{M} f^{2}{}_{i,j(i)}}, \qquad (2.22)$$

where, k is the time of the event calculated using the traveltime equation [in this case, equation (2.21)], N is the window length within which semblance is calculated, M is the number of traces, i is the channel (in this case the offset), and j is the time sample, and $f_{i,j(i)}$ is the seismic amplitude at offset i, and at time sample, j. Using equations (2.21) and (2.22), a Matlab code was developed to compute semblance as a function of PS velocity, velocity ratio (γ_0), and zero-offset, two-way time; i.e. semblance = SC(V_{ps}, γ_0, t_{ps0}) . To execute the code, a range of values of PS velocities and velocity ratios are scanned with respect to each zero-offset time. In a manner akin to routine velocity analysis, values corresponding to maximum semblance are extracted.

After computing semblance as described in the foregoing, the next step is to extract γ_0. To do this, I adopted the scanning methods described below.

2.6.2 Timeslice Method

The raw data consists of either an ACP gather or a shot gather generated from a modeling package, or from real data sets. To search for γ_0 the following steps are involved:

- Compute the semblance volume defined by t_{ps0}, V_{ps0}, and γ_0 using equation (2.21) as shown schematically in Figure 2.6.
- Next, compute the average semblance from the volume by summing semblances obtained from the above step (i.e., summing along the γ_0 axis) and dividing by the number of γ_0. The output is placed onto the time-velocity plane (Figure 2.6, red dots). The final result is a 2D semblance display.
- Display the shot gathers, 2D and 3D semblance side by side.
- From the 2D semblance, pick stacking velocities at major stratigraphic boundaries to derive the velocity function. This step would provide a sparse set of times of maximum 2D semblance as against every time sample. These sparse set of times would reduce the number of timeslices to be generated; and hence, speed up the scanning process.
- Then slice the 3D semblance volume at picked times; and from each timeslice (V_{ps}-γ_0-plane), identify the γ_0, value that corresponds to the picked value Vps at maximum semblance (Figure 2.7). In Figure 2.7, the green dots represent maximum semblance.

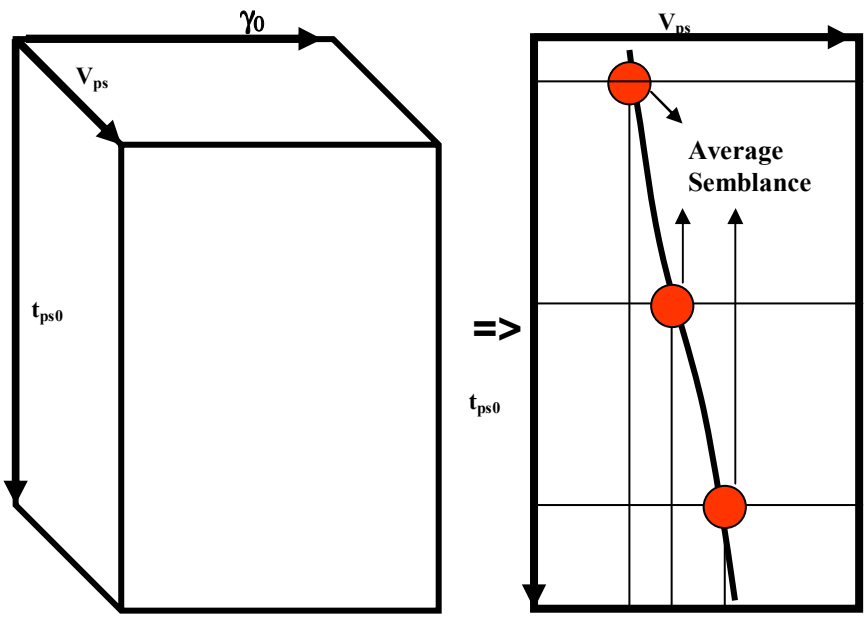

Figure 2.6. Schematic illustrating the Timeslice Method: on the left is the 3D semblance volume from which the 2D average semblance (right) is obtained.

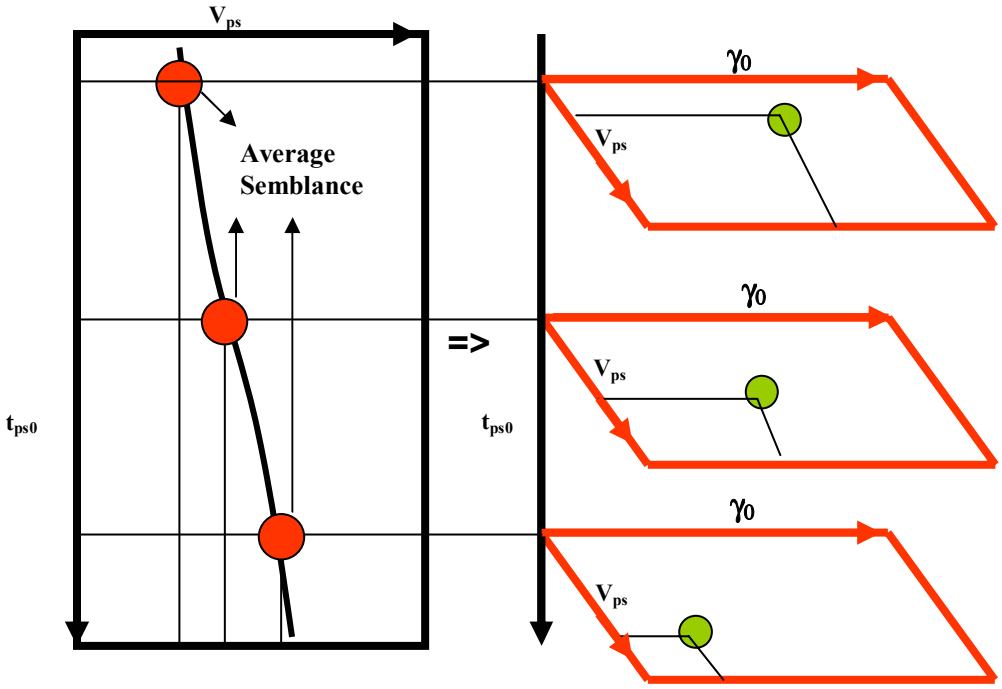

2D average semblance Timeslice at picked zero-offset times

Figure 2.7. Schematic illustrating the Timeslice Method: on the left is the 2D average

semblance; while on the right, are timelices (γ_0-V_{ps}-planes) at picked zero-offset times.

2.6.3 The Log-type Method

The computational method involved in this scheme is conceptually the same as the Timeslice Method; however, it does differ in that, instead of using the entire volume at once, it is subdivided into sub-volumes (Figure 2.8), and 3D semblance volume computation is performed for each sub-volume.

The algorithm to search for γ_0 is designed as follows:

- Divide the entire volume into sub-volumes; the number of volumes will depend on the range of γ_0 values contained in each volume.

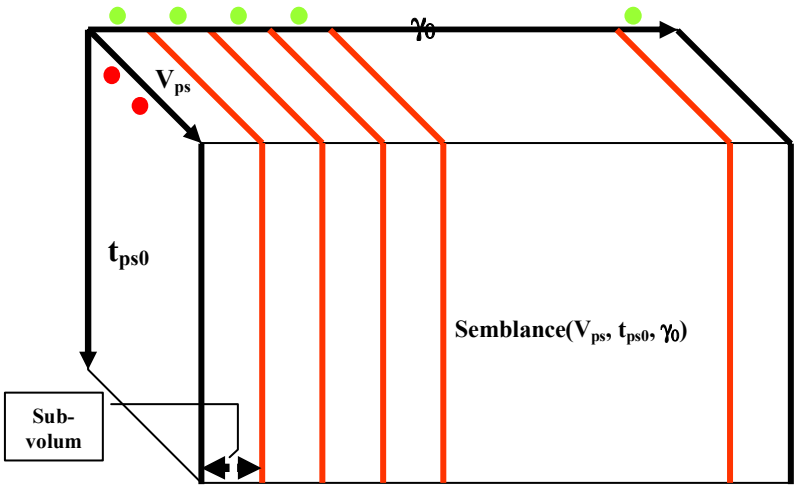

Figure 2.8. This figure demonstrates the concepts that underlie the Log-type γ_0 scanning method. The red dots represent semblance values on the semblance panel; while the green dots represent average γ_0 value for each sub-volume.

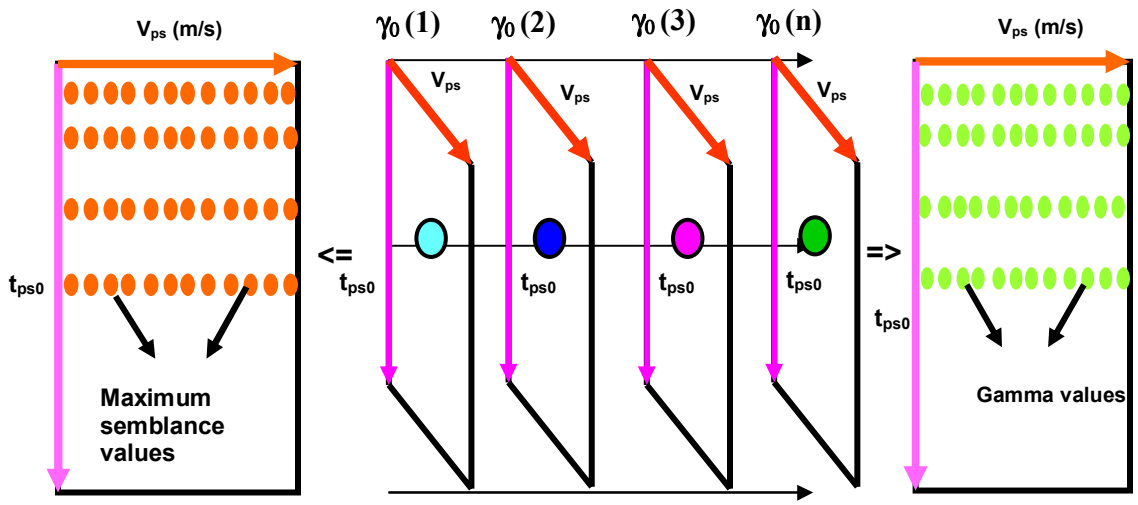

Figure 2.9. Schematic illustrating the Log-type Method; in the center plot, each panel represents the 2D velocity semblance from the different sub-volumes. The differently colored dots cyan, blue, purple, and green represent different semblance values on the different 2D semblance panels, from which the maximum is selected at each zero-offset time and corresponding V_{ps}. The selected value is output onto the final 2D semblance panel (left panel). The γ_0 value that corresponds to the selected maximum semblance is output onto the γ_0-panel (right panel).

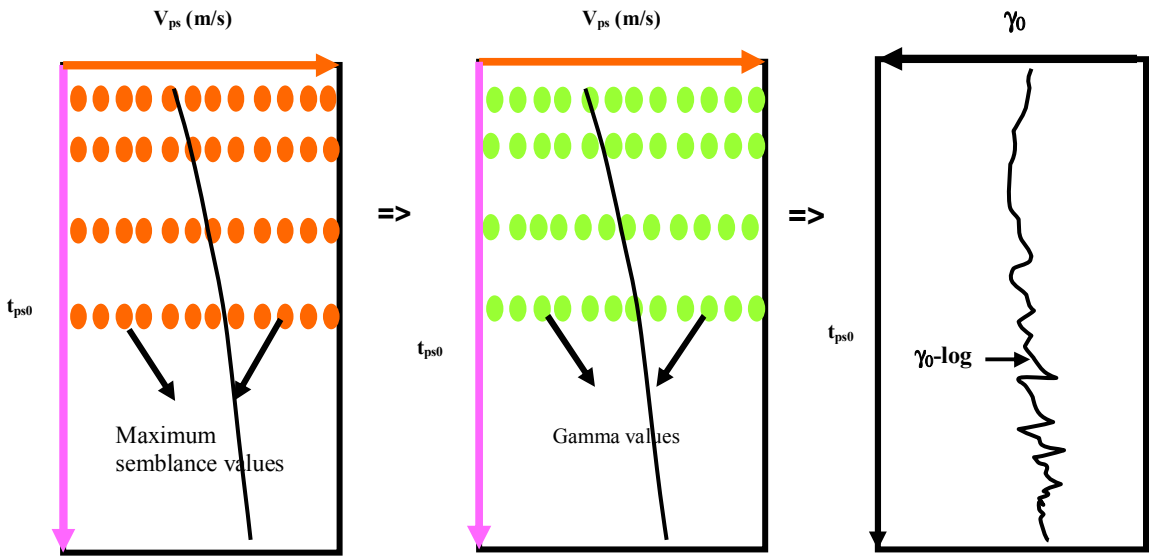

Figure 2.10. Schematic illustrating the Log-type Method: the left panel shows the final 2D velocity semblance panel; on it, is the picked velocity function. The center panel shows the output γ_0-panel on which the velocity function is superimposed. γ_0 values encountered by the function are automatically plotted against corresponding PS-wave zero-offset time to give the γ_0-log (right panel).

- Compute the 3D semblance volume within each sub-volume, and output a 2D semblance panel as outlined in the timeslice method.
- The γ_0 corresponding to this 2D semblance panel will be the average γ_0 used within the sub-volume. That is, if there are say 20 sub-volumes, there will be 20 average γ_0 values corresponding to 20 semblance panels.
- Next, for each time-velocity coordinate pair, search for maximum semblance amongst all the 20 panels. The γ_0 value that corresponds to the maximum semblance is output onto a γ_0 panel; while the maximum semblance value is

output onto a semblance panel. The end result will be a final 2D velocity semblance panel and a 2D γ_0 panel (Figure 2.9).

- From the final 2D velocity semblance panel, pick velocity-time pairs that correspond to maximum semblance. Interpolate picked values according to the time sampling rate to obtain a continuous time-velocity coordinate pairs.
- These interpolated velocity-time coordinate pairs are transferred onto the γ_0 panel from whence, corresponding γ_0 values are automatically picked and plotted to give a continuous γ_0-time log (Figure 2.10).

Based on the concepts described above, Matlab codes were written and applied to numerical and real data sets to scan for stacking velocities and γ_0.

2.7 Application: single layer isotropic model using the Timeslice Method

The geologic model shown in Figure 2.1 was used to test the timeslice method. A single synthetic shot gather was generated using the ANIVEC. The maximum spread length was 6000m while the trace spacing was 100m. The shot gather was then exported to Matlab for semblance analysis and velocity ratio extraction. Figures 2.11 to 2.13 demonstrate the results from this experiment. In Figure 2.11, the seismic section, the 2D velocity semblance as well as the 3D semblance are shown. Figure 2.12 shows the 2D velocity semblance with the red arrow pointing to the location of maximum semblance. At this location, the picked stacking velocity (2100 m/s) agrees with the computed velocity (2078 m/s) at the corresponding time of 5.56 seconds. Figure 2.13 shows the timeslice at 5.56 seconds. On the V_{ps}-γ_0 plane, the location of maximum semblance can be seen; at

this location, the corresponding stacking velocity and γ_0 values are respectively 2100 m/s and 2.93.

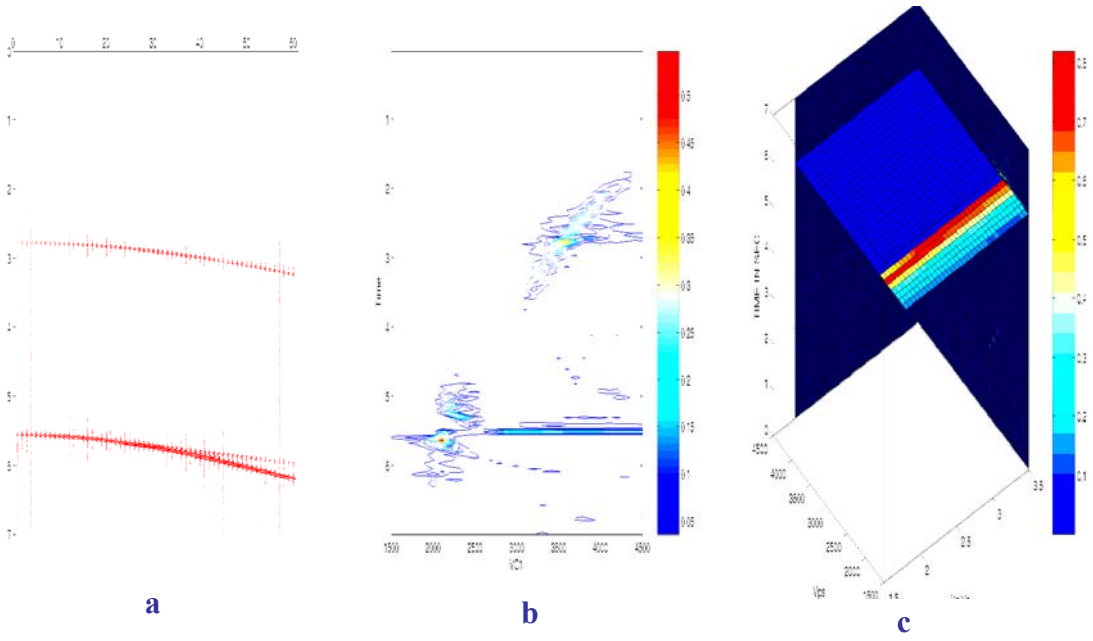

Figure. 2.11. The plots labeled a, b, c are respectively the seismic record, 2D and 3D time-velocity semblances.

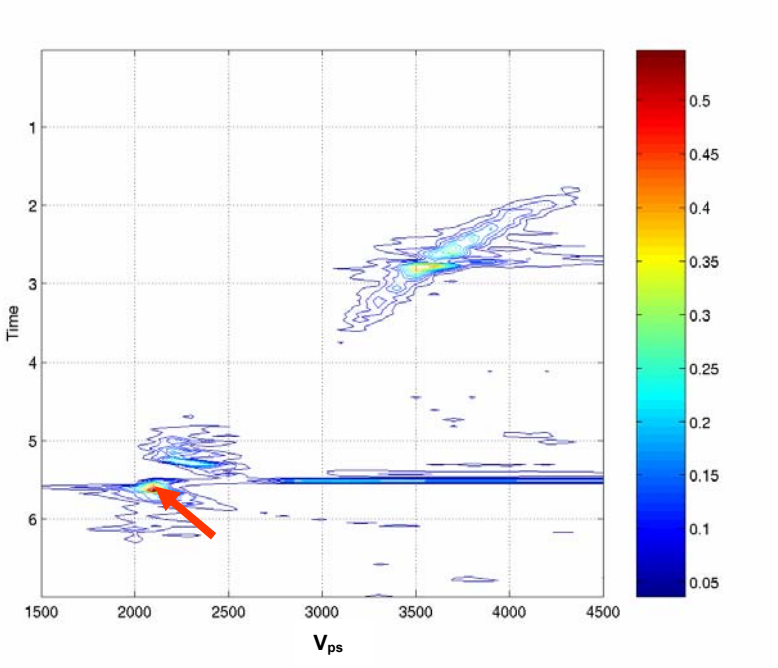

Figure 2.12. 2D velocity semblance; the red arrow indicates maximum semblance. The semblance values shown in this display are the average semblance values obtained as described in section 2.6.2.

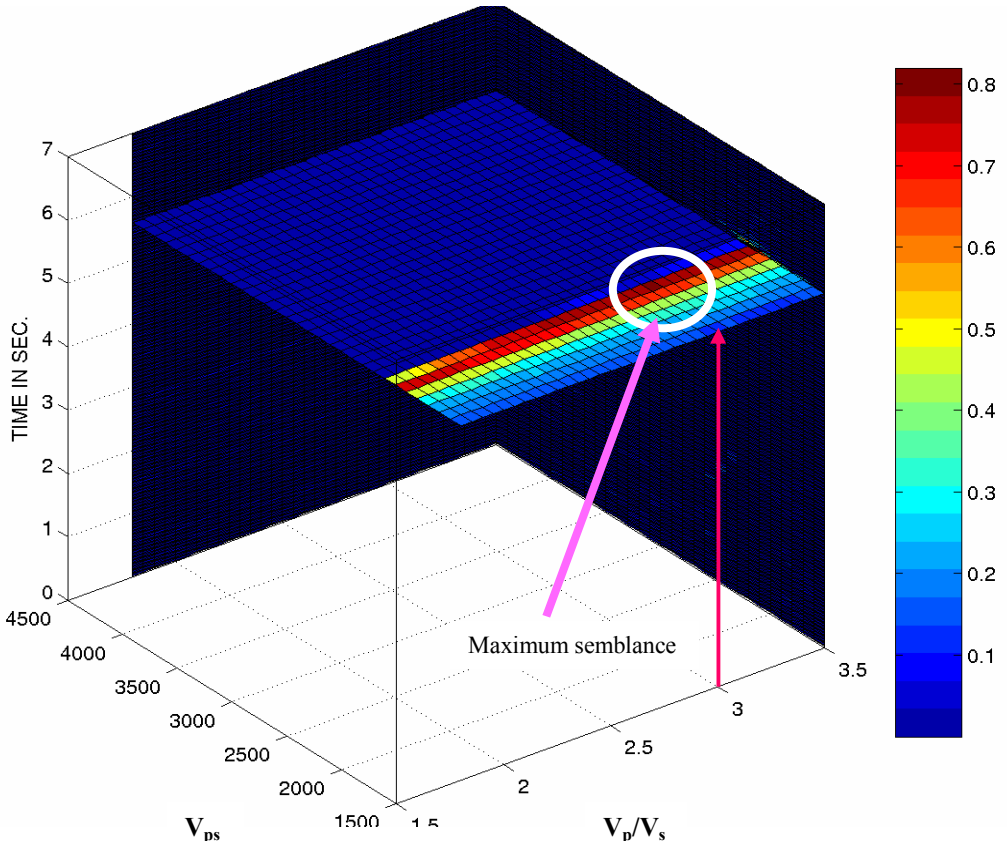

Figure 2.13. Timeslice at 5.56 seconds; stacking velocity and V_p/V_s values corresponding to maximum semblance are 2100 m/s and 2.93 respectively.

2.7.1 Error analysis

The errors incurred in velocity and γ_0 are shown in Table 2.5. From the table, the error in both stacking velocity and γ_0 are respectively 1.0 and 2.4%.

Table 2.5: Error analysis from single layer using the timeslice scanning method

γ_0*	V_{ps}* (m/s)	γ_0**	V_{ps}** (m/s)	Error in γ_0 (%)	Error in V_{ps} (%)
3.0	2078	2.93	2100	2.4	1.0

The * indicate input values, while the ** indicate scanned values.

2.8 Application: multilayer isotropic model

In the multi-layer case, both the Timeslice and the Log-type γ_0 scanning methods were performed. The procedures used in this project are summarized in Flow chart 2.1. Each step is briefly described.

2.8.1 Geologic modeling in GX2

A geologic model, composed of three layers was constructed using GX2 modeling package. The model with its physical attributes is shown in Figure 2.14. Computed average vertical velocity ratios using equation (2.2) as well as the two-way traveltimes are shown in Table 2.6; while the computed RMS velocities are shown in Table 2.7. Model maximum spread length and receiver spacing are respectively 4000m and 100m; depth to the deepest reflecting interface is 3600m. The synthetic shots gathers was generated using a Ricker wavelet of 30 HZ dominant frequency. A total of 41 shots were acquired with a split-spread shooting pattern.

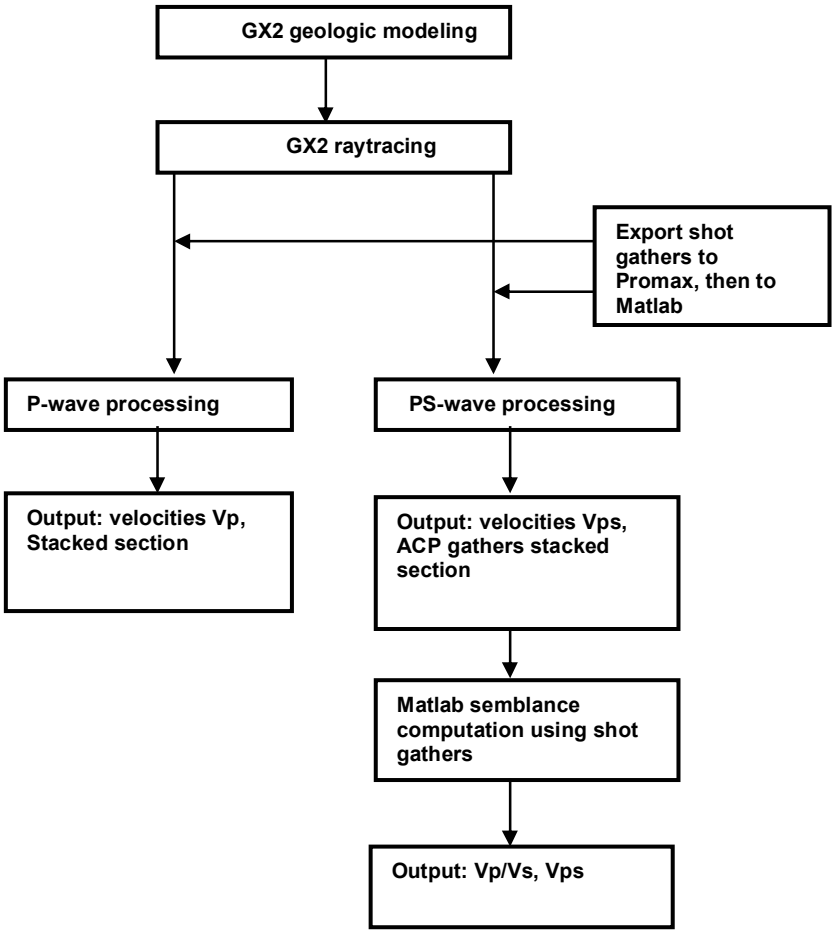

Flow chart 2.1. Schematic diagram showing experimental procedures

Figure 2.15 shows the P- and PS-wave shot records; in both sections, the far offset traces exhibit a phase change/ post-critical angle events. The shot gathers were exported to Promax seismic processing environment from where a PS-wave shot gather was later exported to Matlab for semblance computation and velocity ratio extraction. Before processing the data in Promax, semblance computation and γ_0 extraction was performed by first deploying the Timeslice method.

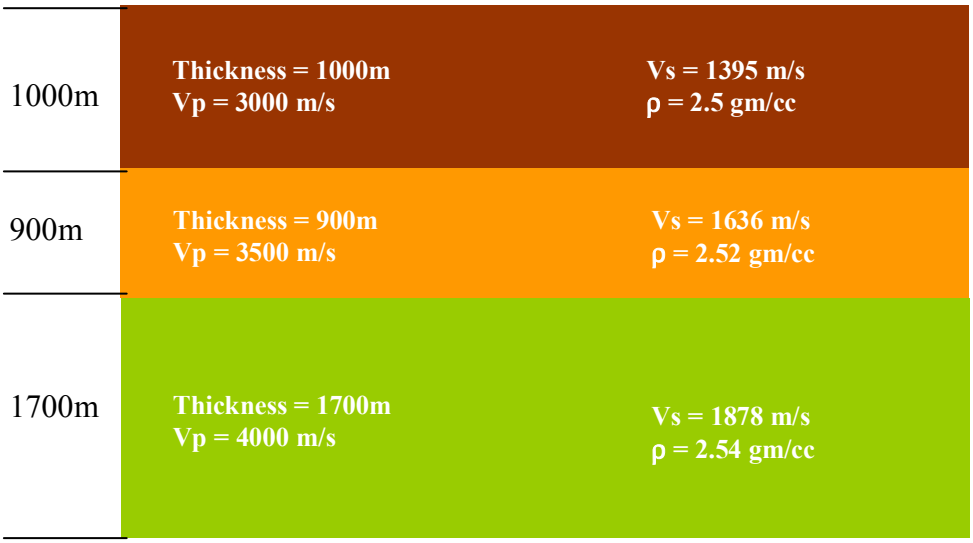

Figure 2.14. A 3-layer geologic model used in GX2 to generate synthetic shot gathers for multi-layer application.

P-wave and S-wave RMS velocities were computed using the following Dix's equation:

$$V_{rms}^{\ 2} = \frac{\sum_{i=1}^{N} t_i v_i^{\ 2}}{\sum_{i=1}^{N} t_i}, \tag{2.23}$$

where Vrms, is the P-wave or the S-wave RMS velocities, while the subscript i refers to the interval time and interval velocity; N refers to the number of intervals.

The results from equation (2.23) are fed into equation (2.24) shown below, to compute the PS-wave RMS velocities.

$$V_{psrms} = \left[\frac{t_{pav} V_{prms}^{\ 2} + t_{sav} V_{srms}^{\ 2}}{t_{ps}} \right]^{0.5}, \tag{2.24}$$

where the subscripts *ps, psrms, pav, prms, sav,* and *srms* refer respectively to PS-wave total one-way time, PS-wave RMS velocity, P-wave total one-way time, P-wave RMS velocity , S-wave total one-way time and S-wave RMS velocity. Results from equations (2.23) and (2.24) are shown in Table (2.7). In this thesis, heterogeneity within the layers is considered to be negligible; hence, the stacking velocities V_p^{nmo} , V_s^{nmo} and V_{ps}^{nmo} are assumed to be respectively equal to the RMS velocities V_{prms} , V_{srms} , and V_{psrms} (Al Chalabi, 1974) .

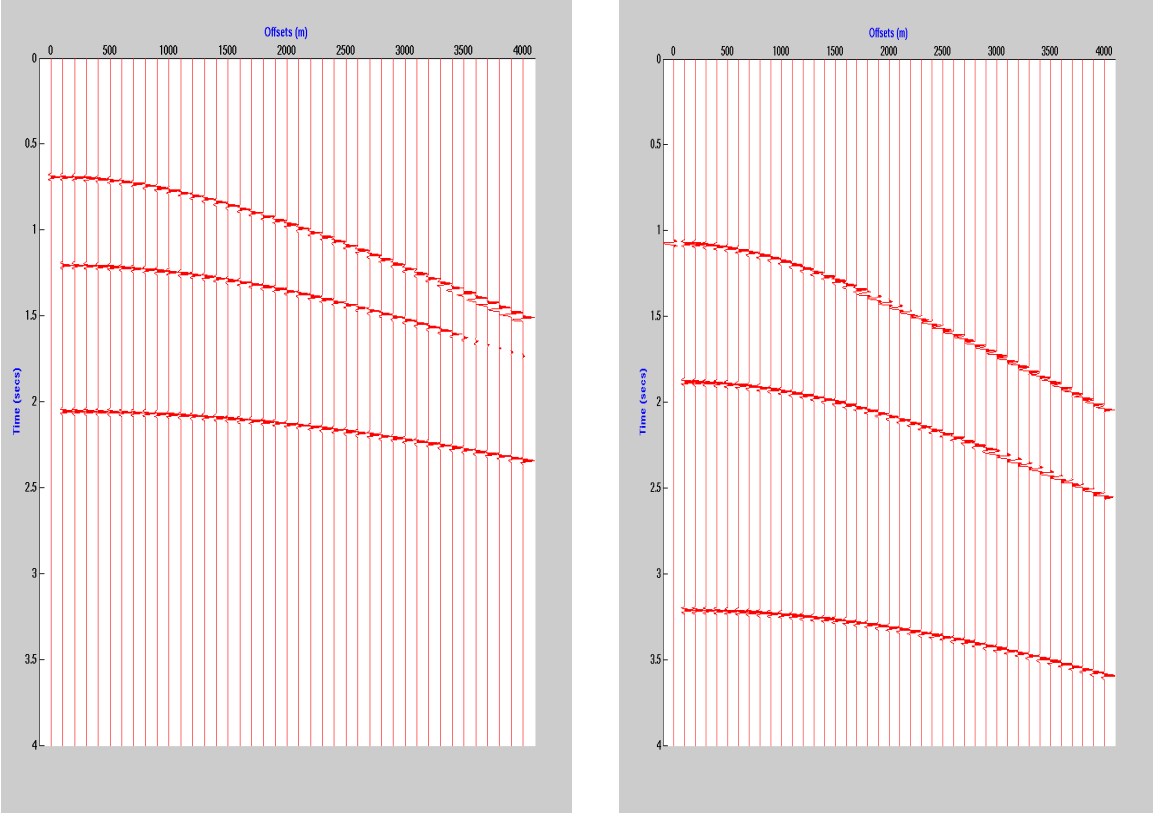

PP shot record PS shot record

Figure. 2.15. Both the PP and PS shot records exhibit post-critical angle events at the far-offsets.

Table 2.6: Computed traveltimes and average vertical velocity ratios γ_0

Thickness	t_{p0} 2-way total (in seconds)	t_{s0} 2-way total (in seconds)	t_{ps0} 2-way total (in seconds)	t_{s0} total/t_{p0} total (γ_0)
1000	0.6666	1.4334	1.0500	2.15
900	1.1808	2.5340	1.8574	2.15
1700	2.0308	4.3446	3.1877	2.14

Table 2.7: Vertical velocities and the computed RMS velocities to the different layers

Thickness	V_{p0} (m/s)	V_{s0} (m/s)	V_{prms} (m/s)	V_{srms} (m/s)	V_{psrms} (m/s)
1000	3000	1395	3000	1395	2046
900	3500	1636	3227	1504	2203
1700	4000	1878	3571	1670	2442

2.8.2 Timeslice Method: multi-layer case

Having exported the PS-wave shot record into Matlab, I performed the 3D semblance volume computation using the Timeslice algorithm. The input into the code are the seismic shot record, a range of regularly sampled γ_0 values (2 to 2.25 at 0.005 interval), a range of PS-wave velocity values (1900-2600 m/s) sampled at 100m/s interval and, a range of regularly sampled PS-wave zero-offset times. γ_0 scanning is done in two stages: first compute the volume and the 2D velocity semblance, secondly, export the volume to the algorithm that does the slicing and produce the 3D display. From the 2D semblance display, stacking velocities and the corresponding zero-offset times are picked at

maximum semblance. At the picked times, timeslices (V_{ps}-γ_0-planes) are then generated. The results of these processes are shown in Figures 2.16 to 2.23

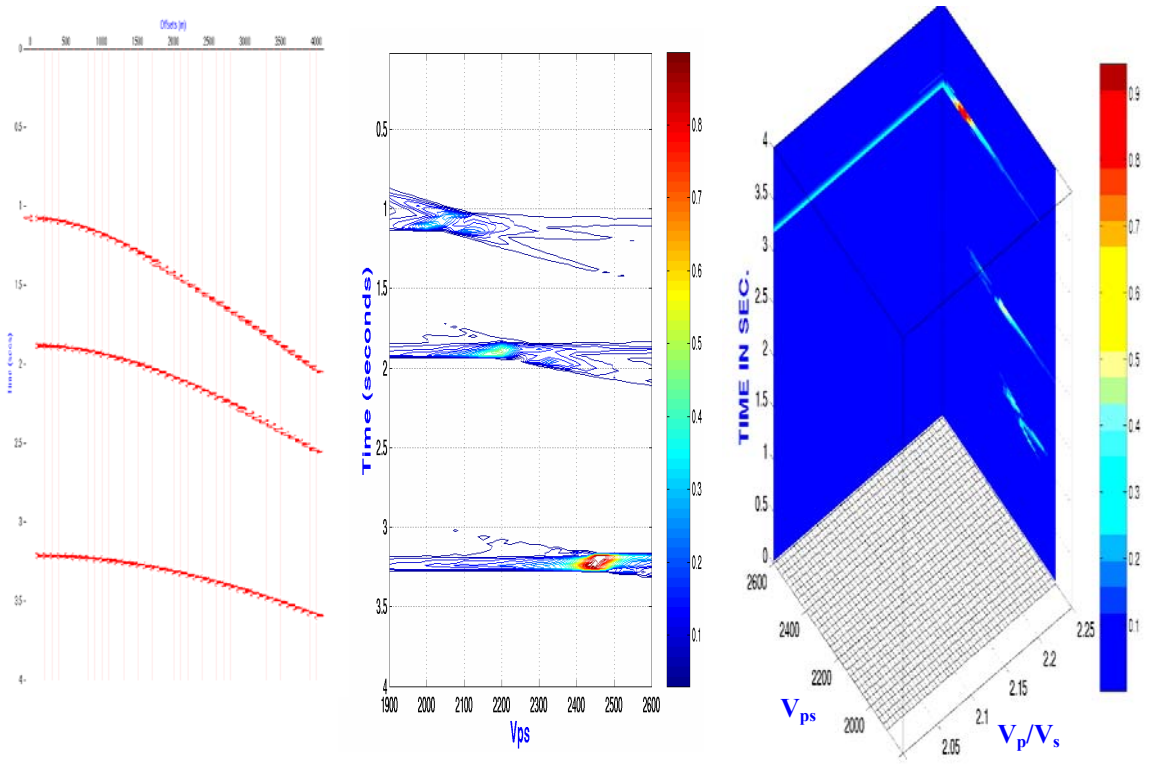

Figure. 2.16. The seismic section (left), 2D semblance (center), and 3D semblance (right) displayed side by side.

2.8.2.1 Results from Timeslice Method: multi-layer case

Figure 2.16 shows the display of the PS seismic section, 2D velocity semblance and the 3D semblance (volume). Shown in Figure 2.17, are the locations of the picked stacking velocities indicated by the black arrows. Figure 2.18 shows the timeslice at the first horizon at time 1.05 seconds. To extract γ_0 values, I identified the stacking velocity at this level on the V_{ps}-γ_0-plane along the velocity axis; with this value as a guide, I followed the

γ_0 axis to the location of maximum semblance. Then I read off the corresponding γ_0 value. At horizon 1, the picked stacking velocity is 2050 m/s and the corresponding γ_0 is 2.08 (Figures 2.18). However, the location of maximum semblance is not very clear. Therefore, to accentuate it, the colorbar is rescaled to reflect the semblance values along this axis. Doing so, the location of maximum semblance becomes clearer (Figure 2.19). This process was carried out for the other two levels. Figures 2.20 to 2.23 show the results at horizons 2 and 3. At horizons 2 (Figures 2.20 and 2.21), the picked stacking velocity is 2200 m/s; and the corresponding γ_0 value is 2.025. Figures 22 and 23 show the results obtained at horizon 3; velocity and γ_0 values are respectively 2450 m/s, 2.035.

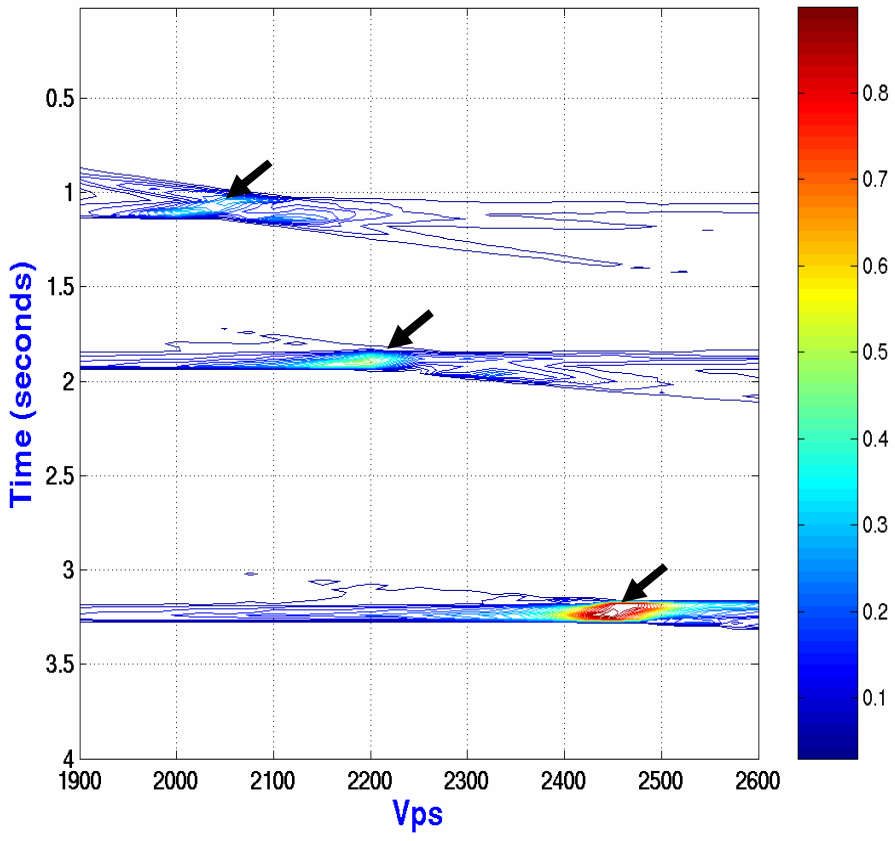

Figure. 2.17. 2D velocity semblance; the black arrows indicate maximum semblance.

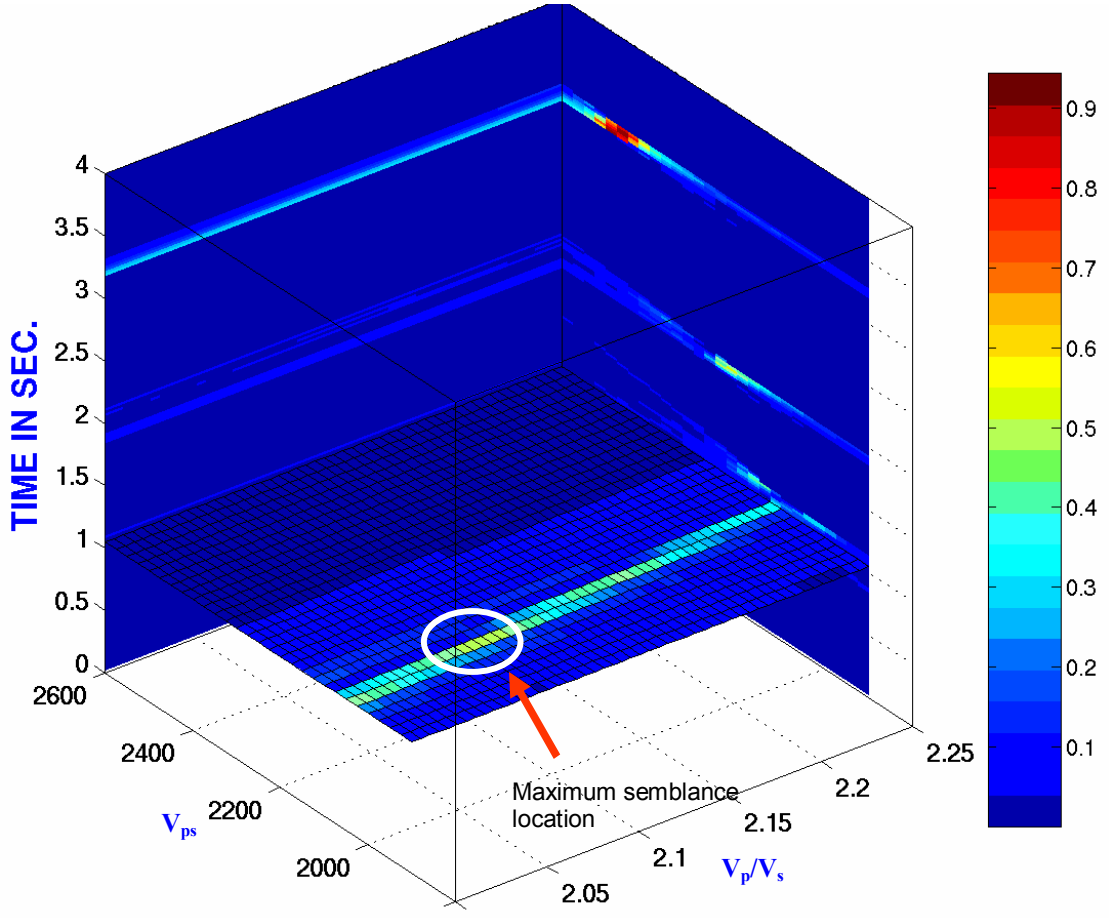

Figure. 2.18. Timeslice at 1.05 seconds (horizon 1) prior to colorbar rescale The red arrow indicates the location of maximum semblance which corresponds to a stacking velocity of 2050 m/s; the corresponding γ_0 value is shown in Figure 2.19.

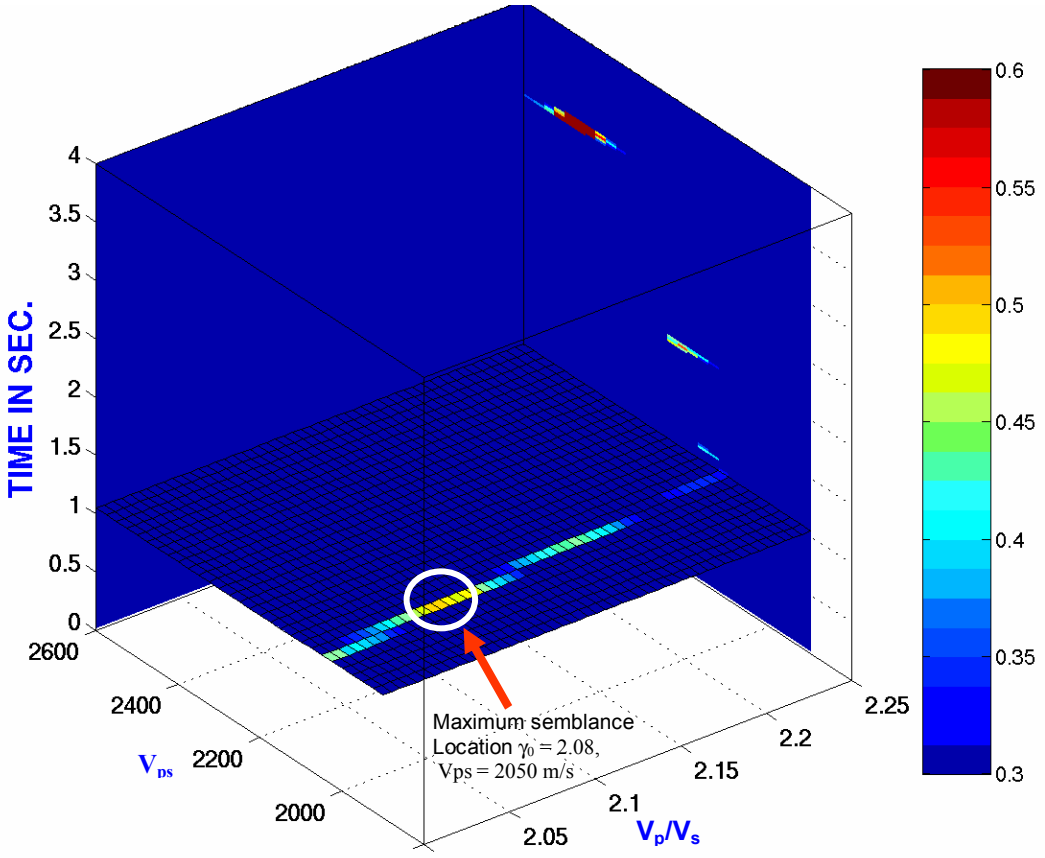

Figure. 2.19. Timeslice at 1.05 seconds (horizon 1) after colorbar rescale

The red arrow indicates the location of maximum semblance which corresponds to a stacking velocity of 2050 m/s; and a γ_0 value of 2.08

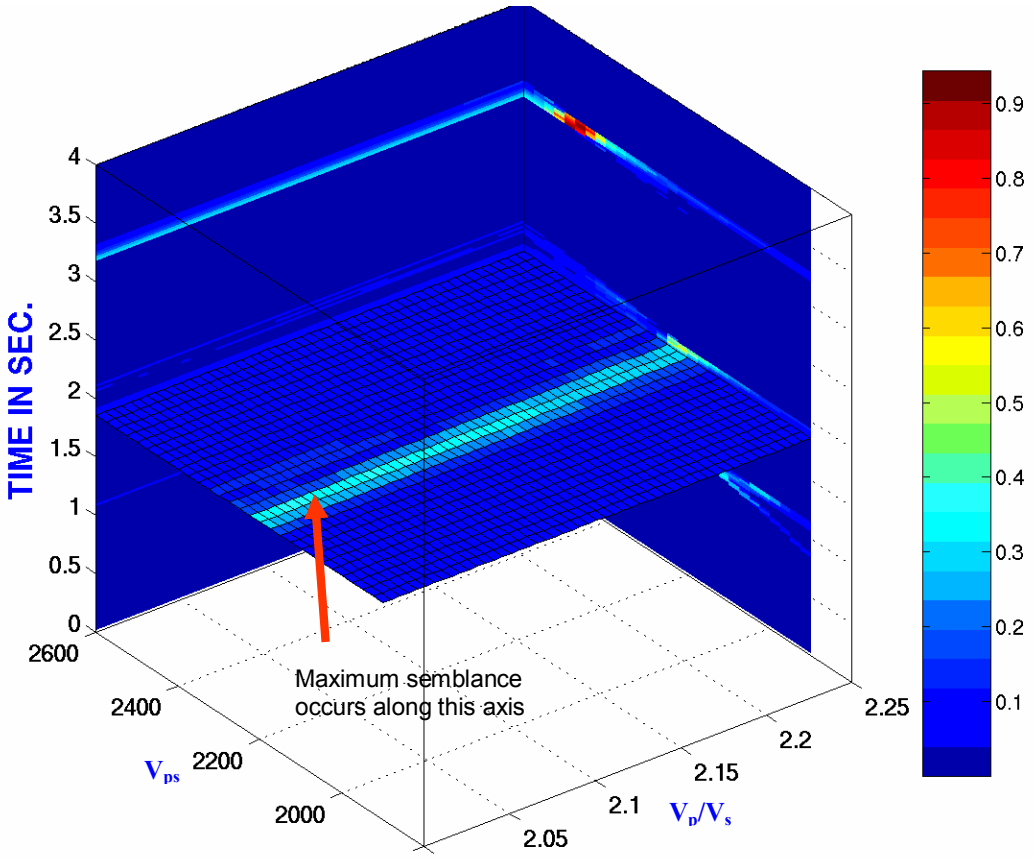

Figure. 2.20. Timeslice at 1.8574 seconds (horizon 2) prior to colorbar rescale The red arrow indicates the location of maximum semblance which corresponds to a stacking velocity of 2200 m/s; the corresponding γ_0 value is shown in Figure 2.21.

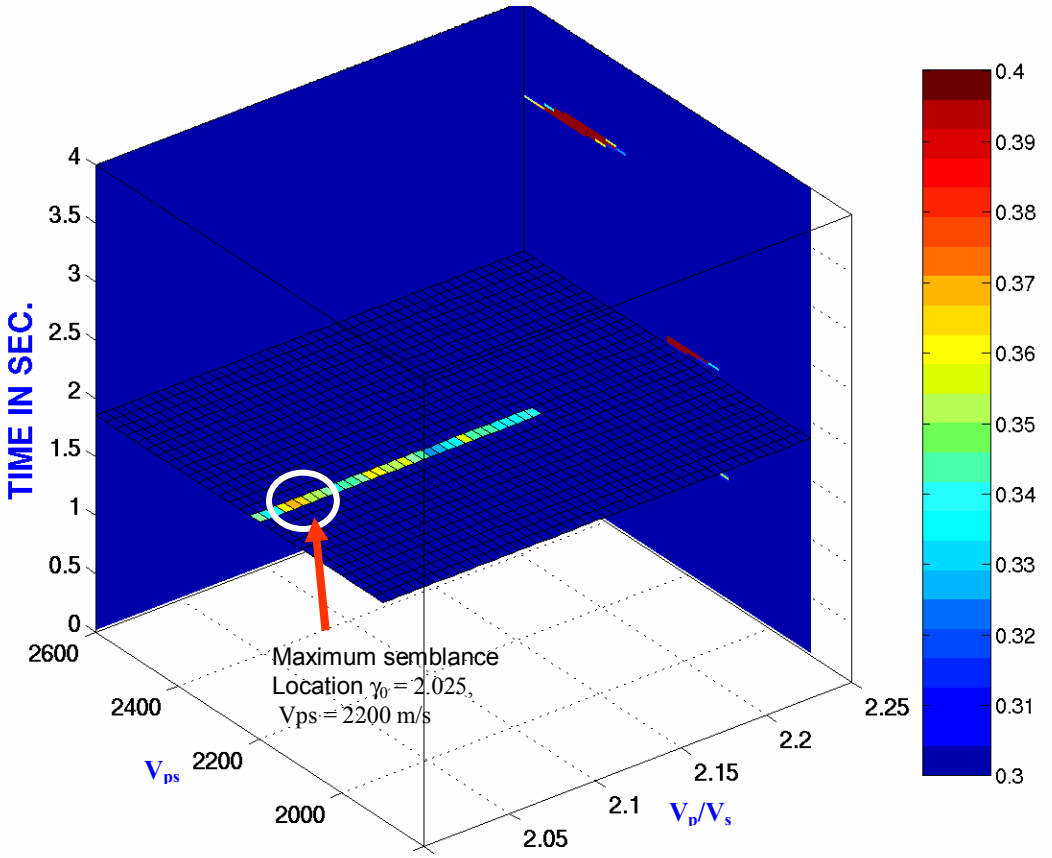

Figure. 2.21. Timeslice at 1.8574 seconds (horizon 2) after colorbar rescale

The red arrow indicates the location of maximum semblance which corresponds to a stacking velocity of 2200 m/s; and a γ_0 value of 2.025

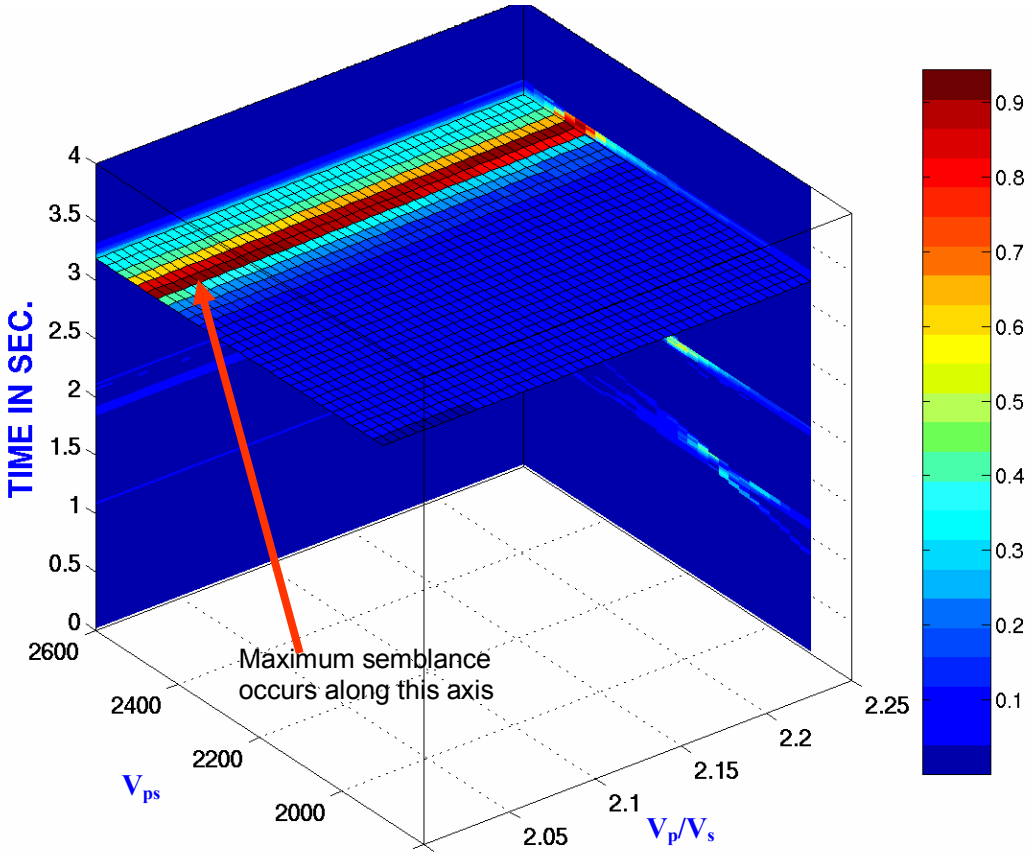

Figure. 2.22. Timeslice at 3.1877 seconds (horizon 3) prior to colorbar rescale

The red arrow indicates the axis along which maximum semblance occurs.

The corresponding stacking velocity is 2450 m/s; the corresponding γ_0 value is shown in Figure 2.23

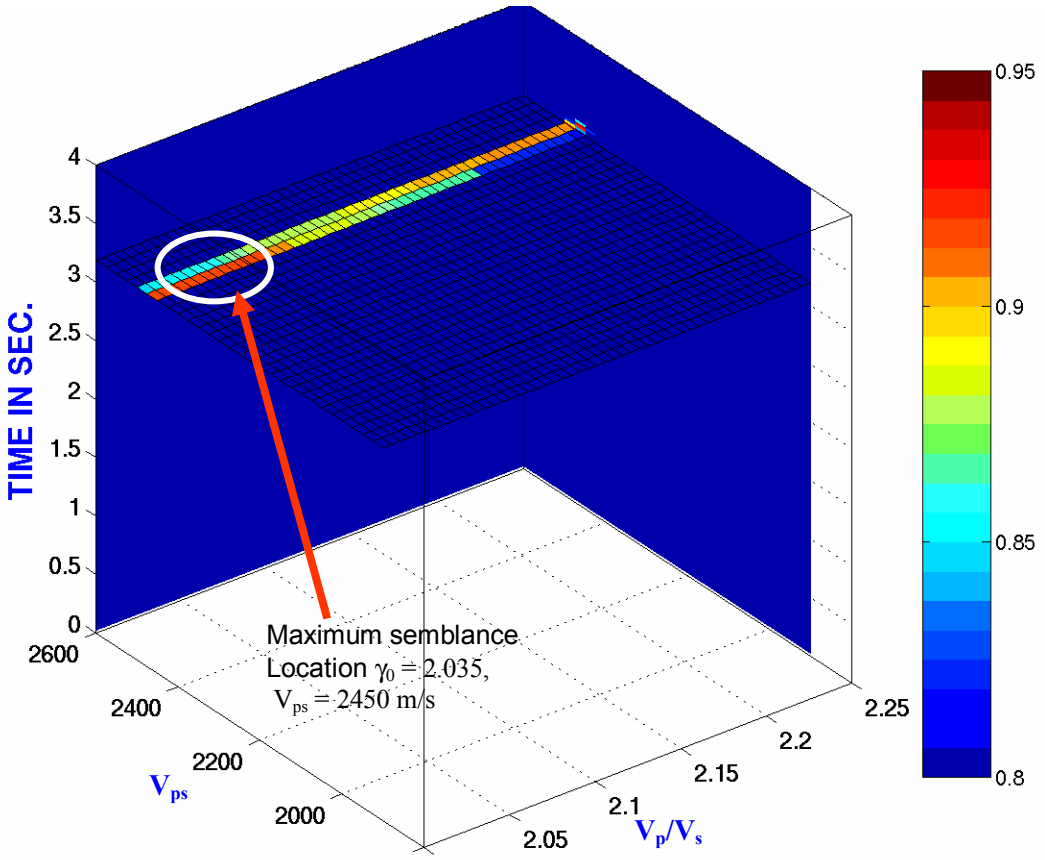

Figure. 2.23. Timeslice at 3.1877 seconds (horizon 3) after colorbar rescale

The red arrow indicates the location of maximum semblance which corresponds to a stacking velocity of 2450 m/s; and a γ_0 value of 2.035. In this figure, since the location of maximum semblance is not a single point, the midpoint of the red cells is taken as maximum semblance location. The value of γ_0 at this point is taken as the scanned γ_0.

2.8.2.2 Timeslice Method: multi-layer case error analysis

The differences between the input velocity ratios and the scanned values are tabulated in Table 2.8; and this difference varies from -3% at the shallow level to -6% at the second level. Table 2.9 shows the error between the scanned velocities and the input velocities.

Table2. 8: Timeslice Method: multilayer case γ_0 error analysis

Horizon	Scanned γ_0	Input γ_0	Difference	% Difference
1	2.08	2.15	-0.07	-3
2	2.025	2.15	-0.125	-6
3	2.035	2.14	-0.105	-5

Table2. 9: Timeslice Method: multilayer case velocity error analysis

Horizon	Scanned Vps(m/s)	Input Vps(m/s)	Difference	% Difference
1	2050	2046	+4(m/s)	+0.2
2	2200	2203	-3(m/s)	-0.1
3	2450	2450	0	0

2.8.3 Log-type Method: multi-layer case

The basic concepts involved in this method, has been outlined (2.6.3) above. Here, instead of computing a single large semblance volume, N smaller volumes (where N is the number of volumes) are computed. The output from this analysis consists of N 2D velocity semblance panels, from which a final 2D velocity semblance is formed. The ultimate results are: a final 2D velocity semblance panel and the 2D color-coded γ_0 panel; both panels have the same PS velocity and time axes. In this experiment I subdivided the whole semblance volume into 10 sub-volumes corresponding to 10 γ_0 values ranging

from 2.0 to 2.26 and sampling at 0.005. Results from 3, out of the 10 2D semblance panels are displayed in Figures 2.24; while the final 2D velocity semblance is shown in Figure 2.25. From the final 2D semblance, I picked the stacking velocities and the corresponding times. As already explained in (2.6.3), these velocity-time coordinate pairs exist on the 2D γ_0 panel. However, since the algorithm is not fully automatic yet, I have to transfer the picked values to the code that automatically spills out the corresponding γ_0 values and plots the γ_0-function (γ_0-time log). Displayed in Figure 2.26 are the final 2D velocity semblance and the 2D γ_0 panels. Figure 2.27 shows the 2D velocity semblance panel, 2D γ_0 panel and the γ_0-time log displayed side by side. In this simple multi-layer model, the γ_0-time log is a series of spikes at the various levels; the scanned γ_0 values starting at the shallowest to the deepest level are: 2.1600, 2.230, and 2.210. From Figure 2.24, it can be seen how moveout velocity varies due to variations in γ_0.

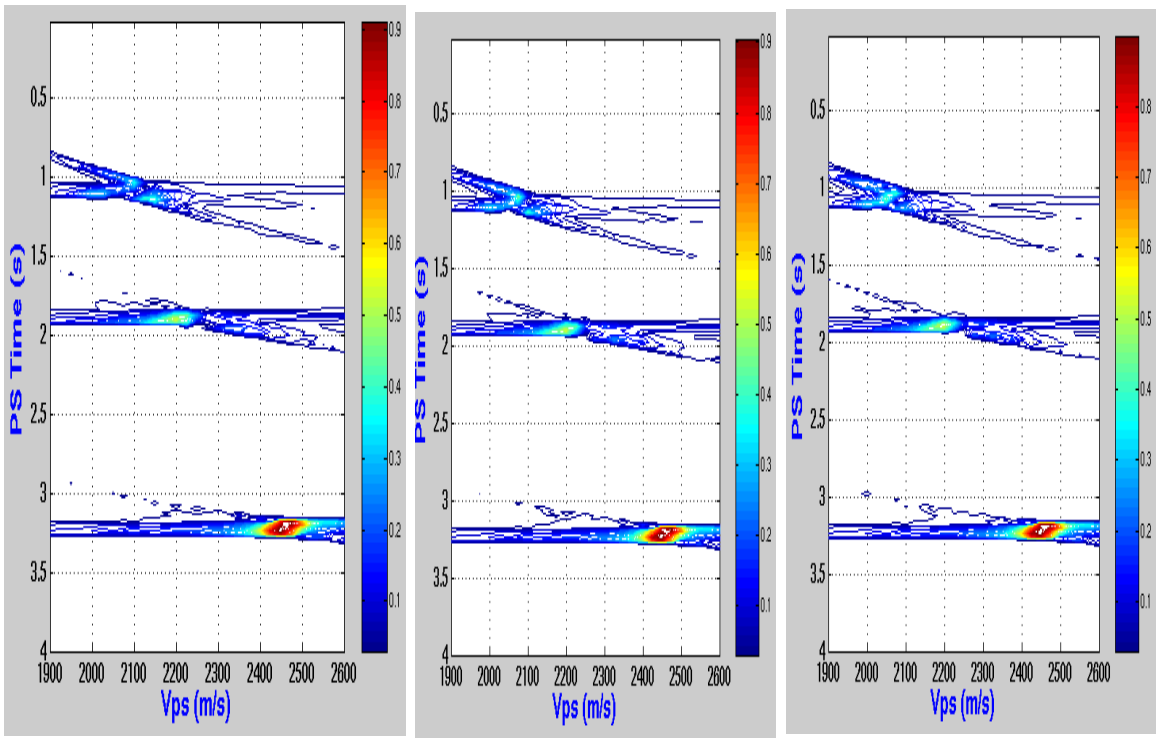

Sub-volume 1: Vp/Vs = 2.01

Sub-volume 4: Vp/Vs = 2.085

Sub-volume 6: Vp/Vs = 2.135

Figure 2.24. 2D velocity semblance from sub-volumes 1, 4, and 6; notice the progressive increase (from left to right) in maximum semblance at the various levels. Moveout velocity variation is very pronounced at the shallowest level in all the sub-volumes. At the 3 horizons, there is better focusing of maximum semblance in sub-volume 6, and the intensity appears to be higher than it is in the sub-volumes 1 and 4.

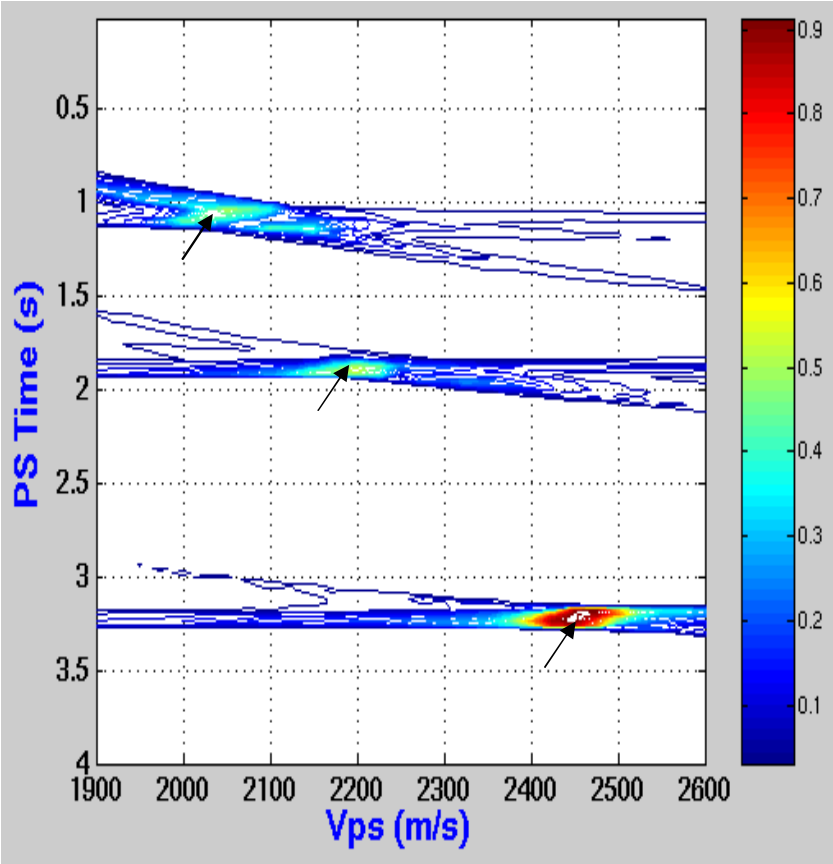

Final 2D velocity semblance

Figure 2.25: Final 2D velocity semblance panel; the black arrows indicate location of maximum semblance.

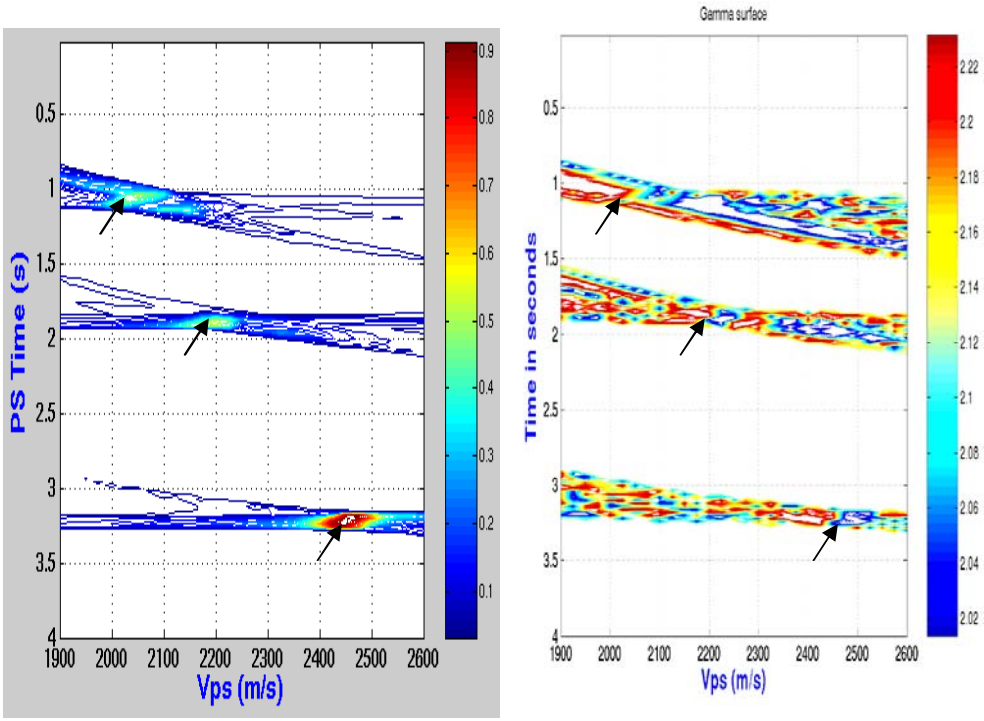

Final 2D semblance γ_0 2D contour

Figure 2.26: This figure displays the final 2D velocity semblance and a color-coded contoured 2D γ_0 panels. The black arrows indicate location of maximum semblance; the corresponding stacking velocities and γ_0 values (Vps, γ_0) at the horizons are: (2040 m/s, 2.1600); (2200 m/s, 2.230); (2450 m/s, 2.2100).

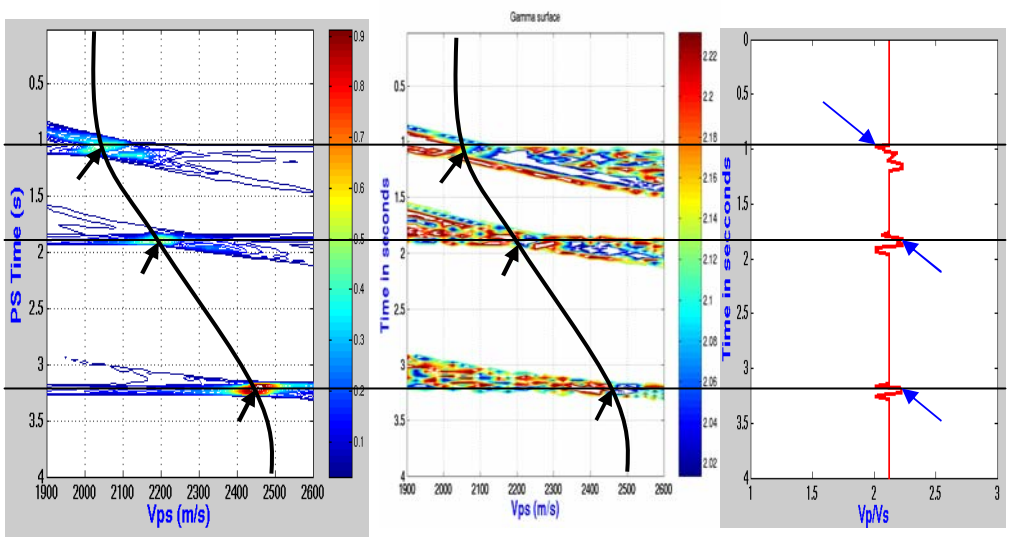

Final 2D semblance γ_0 2D contour γ_0-time log

Figure 2.27: Display of final 2D velocity semblance panel, 2D γ_0 color-coded contoured panel, and γ_0-time log. The γ_0 values at the three horizons (1 to 3) are respectively, 2.1600, 2.23 and 2.21; and the respective stacking velocities are 2040 m/s, 2200 m/s, and 2450 m/s. Superimposed on the 2D semblance and γ_0 panels is the velocity function picked on the velocity semblance panel. The blue arrows indicate the γ_0 values location on the γ_0-time log panel (extreme right)

The results obtained from the Log-type method are summarized in Table 2.10.

Table 2.10: Summary of results from the Log-type Method (multi-layer case)

Horizon	PS-wave times (s)	PS-wave velocities	Scanned γ_0
1	1.0500	2040 m/s	2.1600
2	1.8574	2200 m/s	2.2300
3	3.1877	2450 m/s	2.2100

2.8.3.1 Log-type Method: multi-layer case error analysis

The differences between the input velocity ratios and the scanned values are tabulated in Table 2.11; these vary from +0.5% at he shallow level to +4% at the second level.

The errors in velocities are shown in Table 2.12.

Table 2.11: Log-type Method: multilayer case γ_0 error analysis

Horizon	Scanned γ_0	Input γ_0	Difference	% Difference
1	2.1600	2.15	+0.01	+0.5
2	2.230	2.15	+0.08	+4.0
3	2.2100	2.14	+0.07	+3.0

Table2. 12: Log-type Method: multilayer case velocity error analysis

Horizon	Scanned Vps(m/s)	Input Vps(m/s)	Difference	% Difference
1	2040	2046	+4(m/s)	-0.3
2	2200	2203	-3(m/s)	-0.1
3	2450	2450	0	0

Having extracted velocity ratios, the next stage is to use the scanned values to transform PS stacked data to P-wave times. In this regard, I had to process the data sets to obtain PP and PS stacked sections. Processing was carried out in Promax.

2.8.4 Processing in Promax environment

Two processing sequences were under taken in Promax, one for the P-wave, and the other for the converted (PS) -wave. Both sequences are shown in Flow Chart 2.2. The two processing sequences are about the same except for the ACP binning step performed in processing the converted wave data. The following is a brief description of each step.

2.8.4.1 Geometry definition.

Geometry definition is a crucial step in Promax. Acquisition geometry will have to be redefined using appropriate code. This process will ensure that CDP points are allocated to their correct positions in order to achieve the correct fold. Once this is done, the next step is to sort the data into CDP gathers.

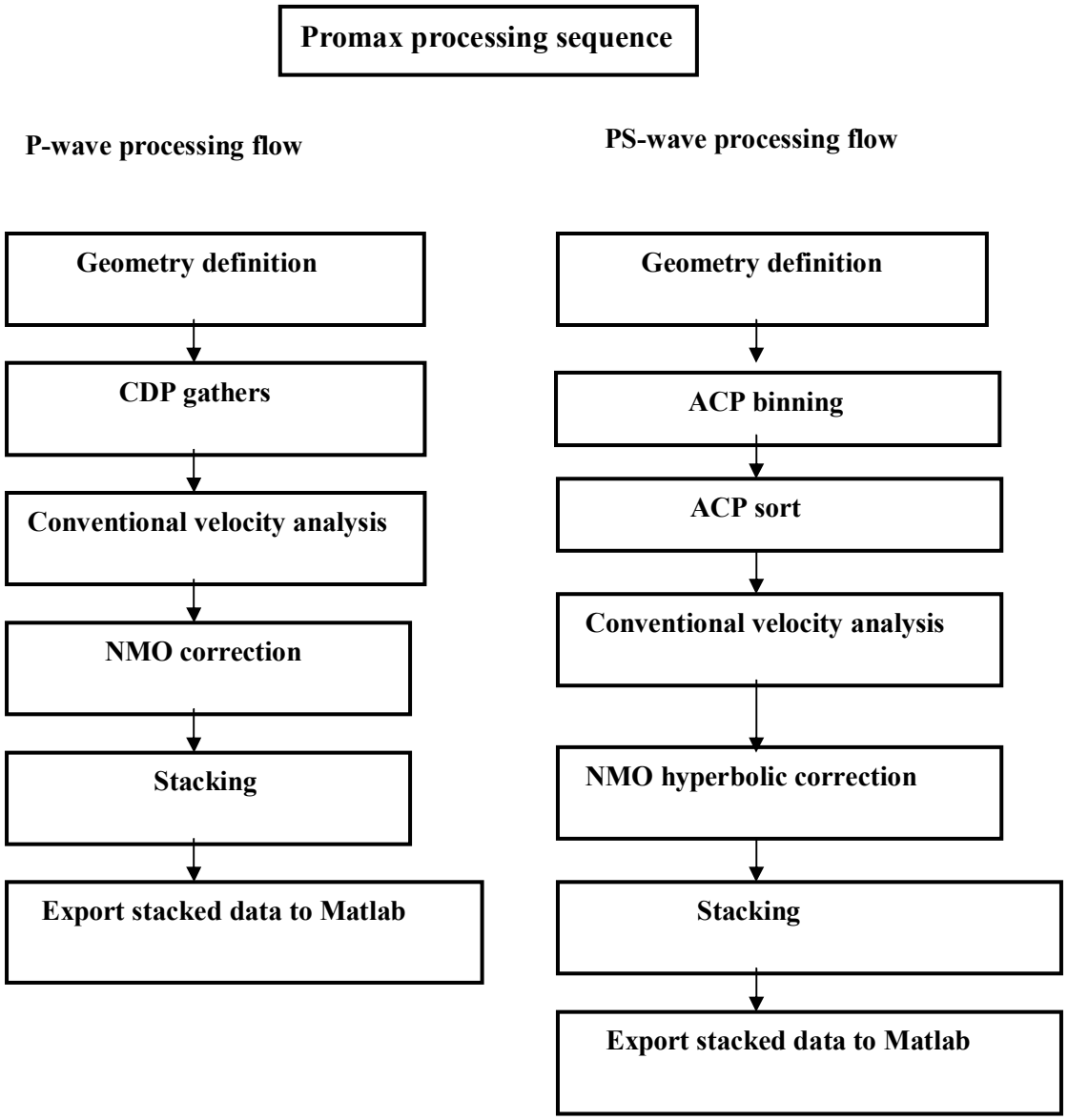

Flow Chart 2.2. Schematic diagram showing Promax processing sequence

2.8.4.2 CDP gathers/ACP binning:

CDP gathers were formed using pertinent information from the geometry. These were then displayed to see if there was any error. Figure 2.28 (a) and 2.28 (b) show traces from CDP 200 for the P-wave and P-S-wave respectively. In the case of the converted wave, the data was sorted using the asymptotic common conversion point ACP method (see Appendix 1). To form the ACP binning, a velocity ratio of 2.1 was used to compute the

conversion point. Having performed this step, the traces with reverse polarity were corrected using the trace header maths. These two processing steps, that is, ACP binning and trace-reverse, were carried out before sorting into ACP gathers.

2.8.4.3 Velocity analysis:

This entails picking the correct stacking velocities from the semblance display. Figures 2.29 (a) and 2.29 (b) are outputs from P-wave velocity analysis. Figure 2.29 (a) is analysis at CDP 200 before NMO correction, while Figure 2.29 (b) is the result after NMO was applied. Figures 2.30 (a) and 2.30 (b) are those of the converted wave from ACP 200.

2.8.4.4 NMO correction and stacking

NMO corrections were applied using the stacking velocities derived above after which, the data set was stacked to obtain the stack sections. Figures 2.31 (a) and 2.31 (b) are the P-wave and PS-wave stacked sections after processing. The stacked data sets were exported to Matlab where PS to PP transformation was performed.

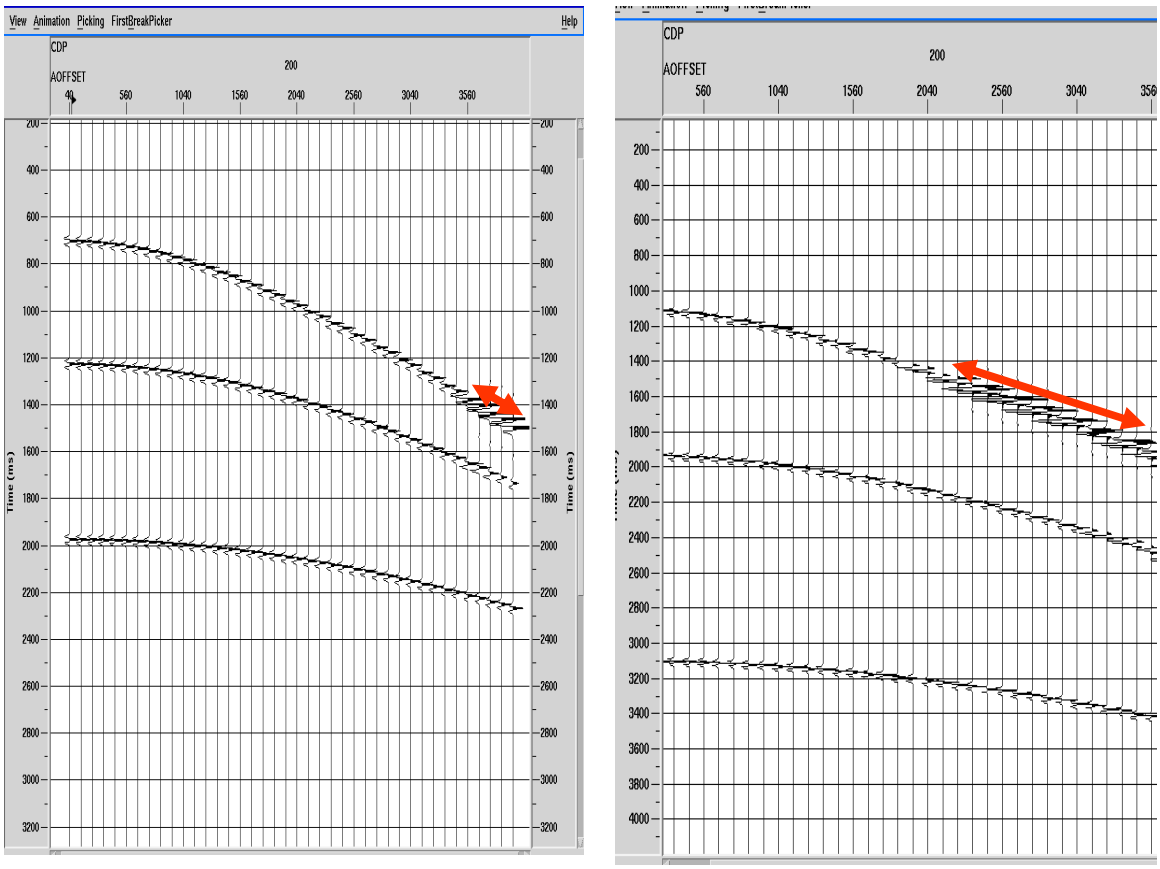

(a) (b)

Figure 2.28. PP CDP gathers at location 200 (a), and PS ACP gathers also at location 200 (b). In Promax, ACP locations are treated as CDP locations. The red double-headed arrows indicate post-critical angle events. It is more pronounced in the case of PS data. These however, were muted before performing velocity analysis and stacking.

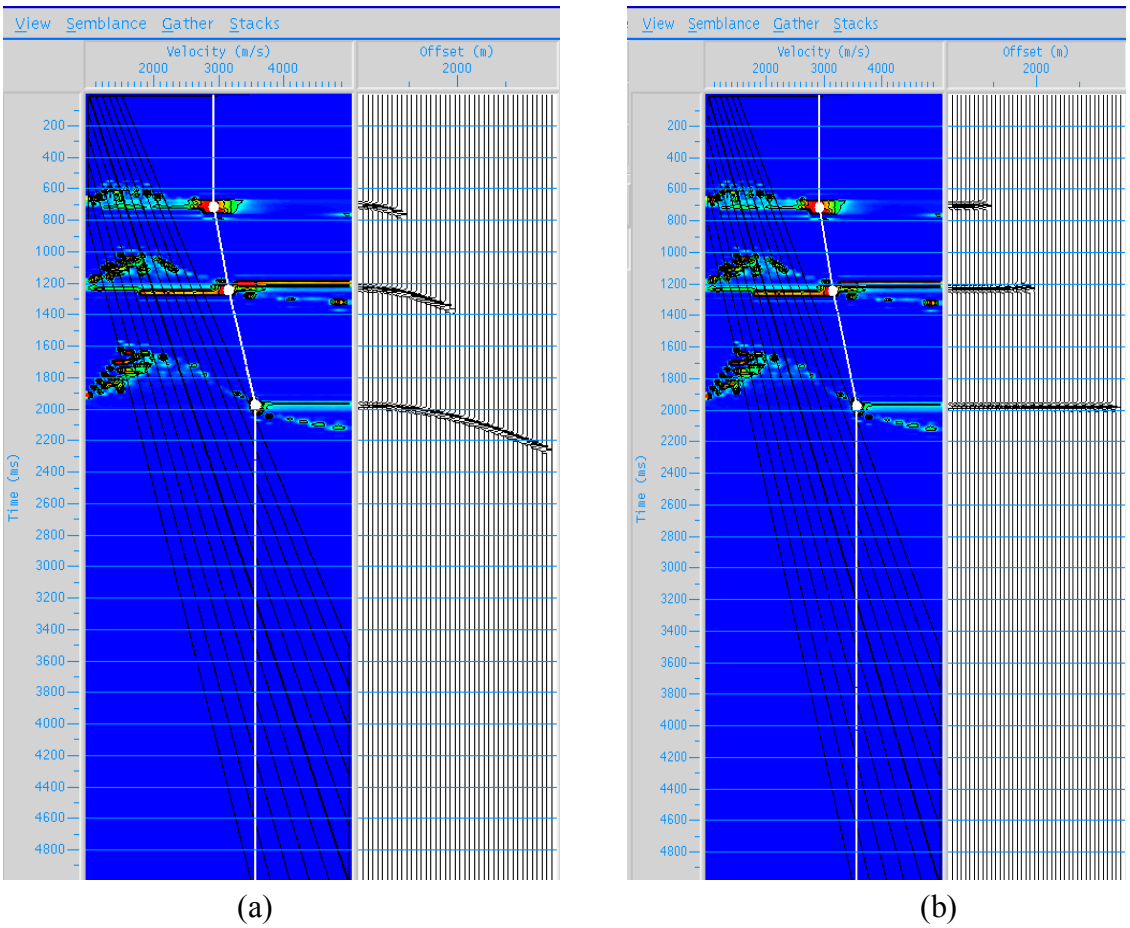

(a) (b)

Figure 2.29. PP velocity analysis and NMO correction; (a) before, (b) after NMO correction

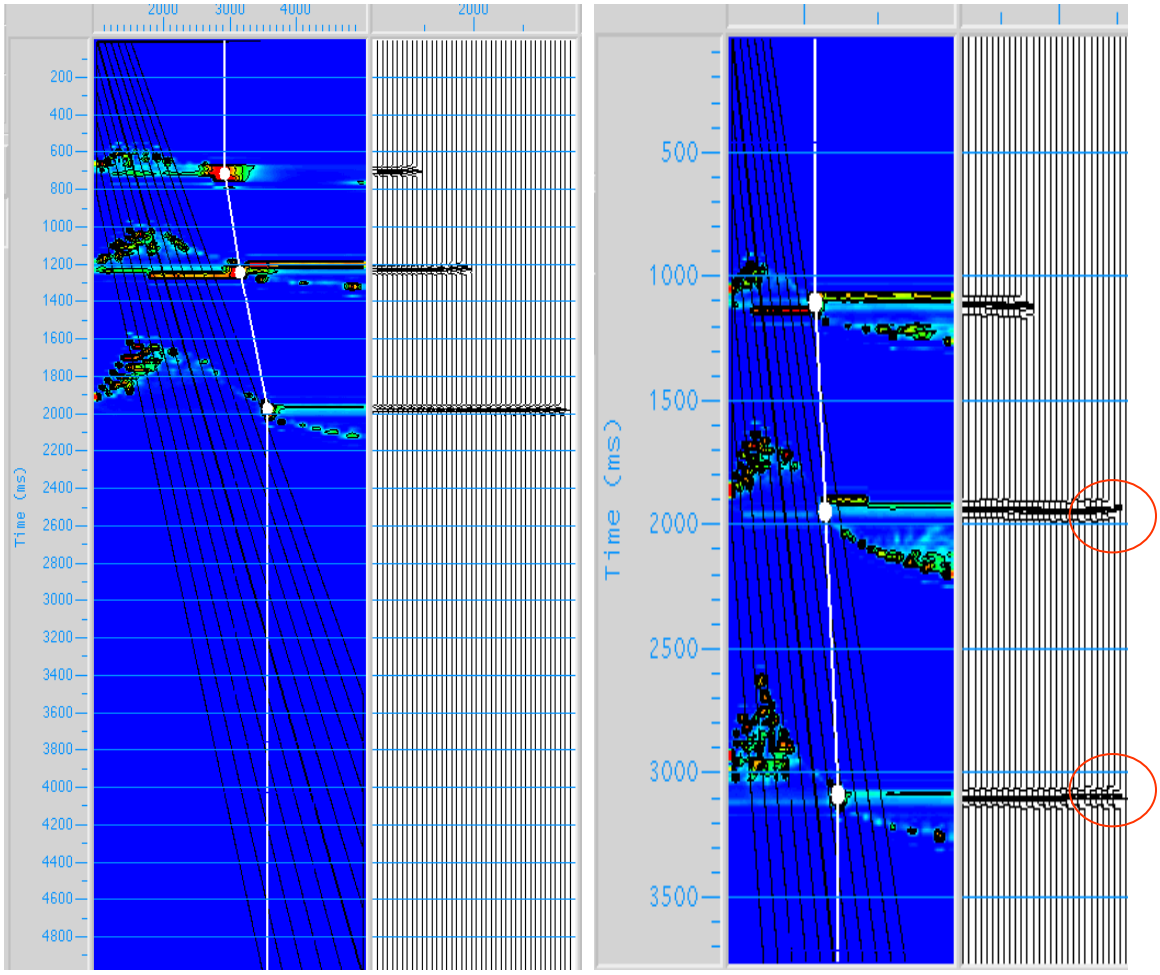

PP semblance

(a)

PS semblance

(b)

Figure. 2.30. PS velocity analysis and NMO correction; (a) before (b) after NMO correction. The events circled in red occurred as a result of the use of the hyperbolic NMO correction; the hyperbolic correction is not adequate for the PS far offset data. However, the near-offset to mid-offset data were stacked to get the stacked section in (Figure 2.31)

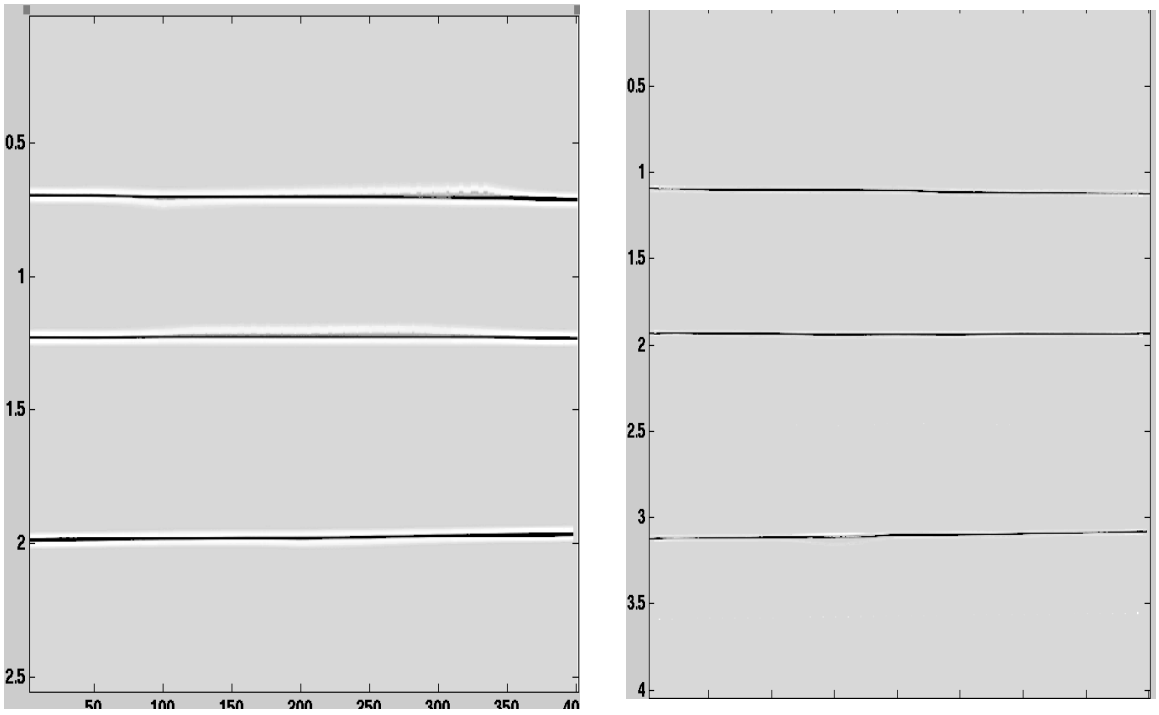

PP stacked data

PS stacked data prior to transformation to PP times

a

b

Figure. 2.31: PP (a) and PS (b) stacked sections. Note the different time scales.

2.8.4.5 PS to PP time mapping

To transform the PS stack data to P-wave times, three steps are involved:

1. Interpolate the γ_0 values obtained from semblance analysis, to generate a γ_0 function. I.E., $\gamma_0(t_{ps0})$.

2. Next, using this function in equation (2.15), compute P-wave times (t_{p0}); the computed P-wave times are shown in Table 2.13.

3. Finally, plot the PS amplitudes from the given PS-times, against the computed P-wave times.

The results of these steps are shown in Figures 2.32 to 2.33. The interpolated γ_0 function is shown in Figure 2.32. Figure 2.33 shows the comparison of the transformed PS stack data and the P-wave stack section. From these figures, it can be seen that the transformed PS data agrees very closely with the P-wave data.

Table 2.13: Computed P-wave times using scanned γ_0 values and equation (2.15)

t_{ps0}	Scanned γ_0	$t_{p0} = (2 * t_{ps0})/(1+\gamma_0)$	t_{p0} from PP data
1.05	2.160	0.6650	0.6667
1.8574	2.230	1.1500	1.1808
3.1877	2.210	1.9861	2.0308

2.8.4.6 Error analysis in PS to PP time mapping

The differences between the computed P-wave times and the actual are shown in Table 2.14. The difference between the actual and computed P-wave times varies from 0.2% to -3%. This shows that the computed results very closely agree with the actual values.

Table 2.14 Differences between actual and derived P-wave times

Horizon	Derived P-wave times	Actual P-wave time	Difference	% Difference
1	0.6650	0.6666	-0.0016	-0.2
2	1.1500	1.1808	-0.0308	-3
3	1.9861	2.0308	-0.0447	-2

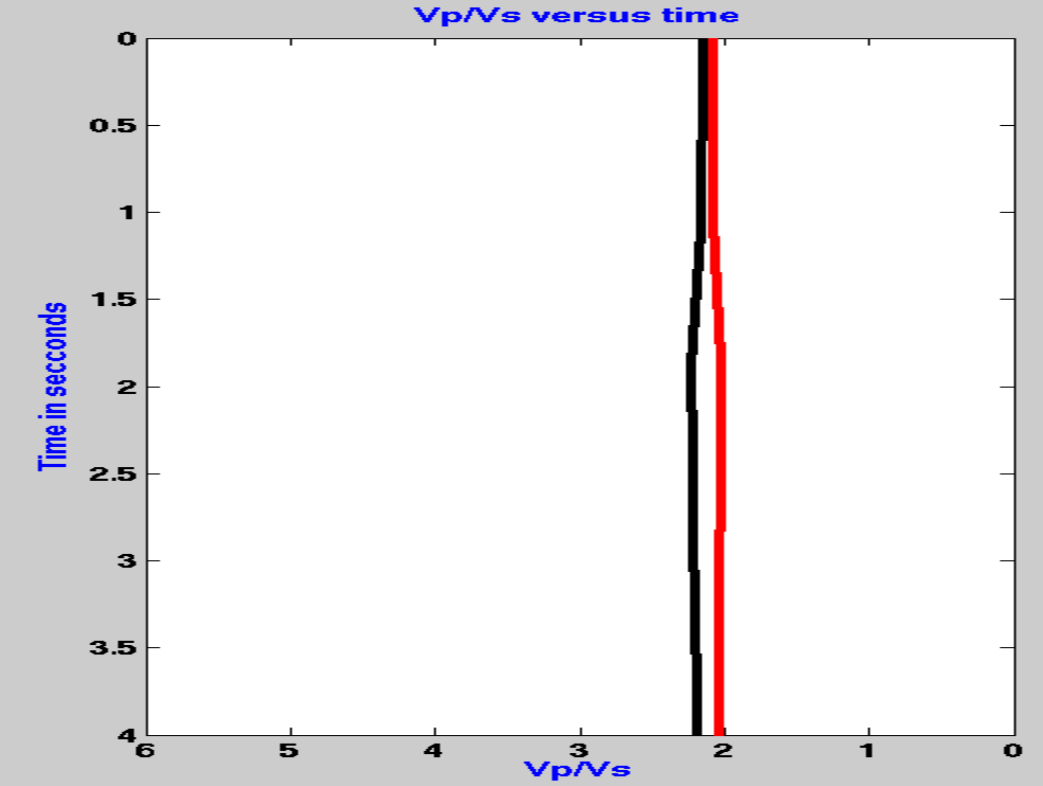

Figure 2.32: γ_0 function from the Timeslice and Log-type Methods after interpolation. The black curve is the function from the Log-type Method, while red curve is the function from the Timeslice Method

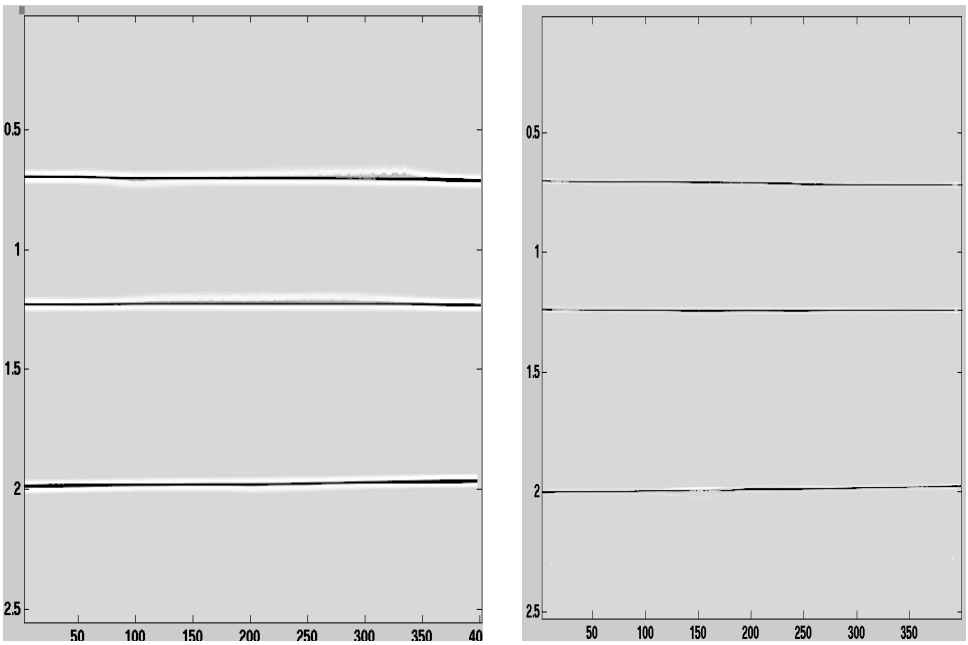

Figure 2.33 Comparison of the transformed PS stacked data with the PP stacked data.

2.9 Summary from chapter 2

In the foregoing Chapter, I discussed the average vertical velocity ratio γ_0 as defined by (Tessmer and Behle, 1988; Garotta, 2000; Thomsen, 1999); and reviewed various mathematical expressions for γ_0. I also discussed the important role it plays in multicomponent seismic exploration. Thereafter, I showed that most VTI parameters can be expressed in terms of γ_0. In addition to this, I reviewed converted-wave traveltime equation in isotropic and homogeneous media as formulated by Tsvankin and Thomsen (1994) and Thomsen (1999). I showed the modification of this expression for the purpose of developing a dual-parameter scanning algorithm. I also discussed the validity of the resultant equation and its sensitivity to the variations of moveout velocities and γ_0; and

concluded that moveout is more sensitive to changes in moveout velocities than it is to changes in γ_0.

Furthermore, I discussed the basic concepts involved in the dual-parameter algorithm development and noted that there are two methods namely, the Timeslice method, so named because it involved timeslicing; and the Log-type method christened as such because, its output is akin to well-log results. These two methods were applied to numerical data sets to scan for γ_0 and stacking velocities. The derived γ_0 function was applied to transform PS to PP times. Results from both methods show that γ_0 can be scanned for from prestack data, by using PS-wave non-hyperbolic traveltime equation. Also, the derived equation is adequate to describe converted-wave (PS-wave). The log-type method scans slightly higher γ_0 values than the Timeslice method. From the Log-type method, the error in γ_0 is less than +/- 5%; while the maximum error in γ_0 from the Timeslice method is 6%. The accuracy increases with increasingly fine sampling of each variable. The Log-type method gives spectacular results that enable us to observe moveout variations with respect to the variations in γ_0.

Chapter 3

Application to real data

3.1 Field data

Having tested the algorithms on numerical data sets, the next stage is to apply the methods to real data. In this regard, I used a 3C seismic line from the Blackfoot Field, Alberta. Described hereunder, are some pertinent information that relate to the area and the seismic acquisition program.

3.2 Location

The Blackfoot Field is location in Township 23, Range 23, West of 4th meridian, in South Central Alberta (Figure 3.1). The Field is operated by EnCana Energy.

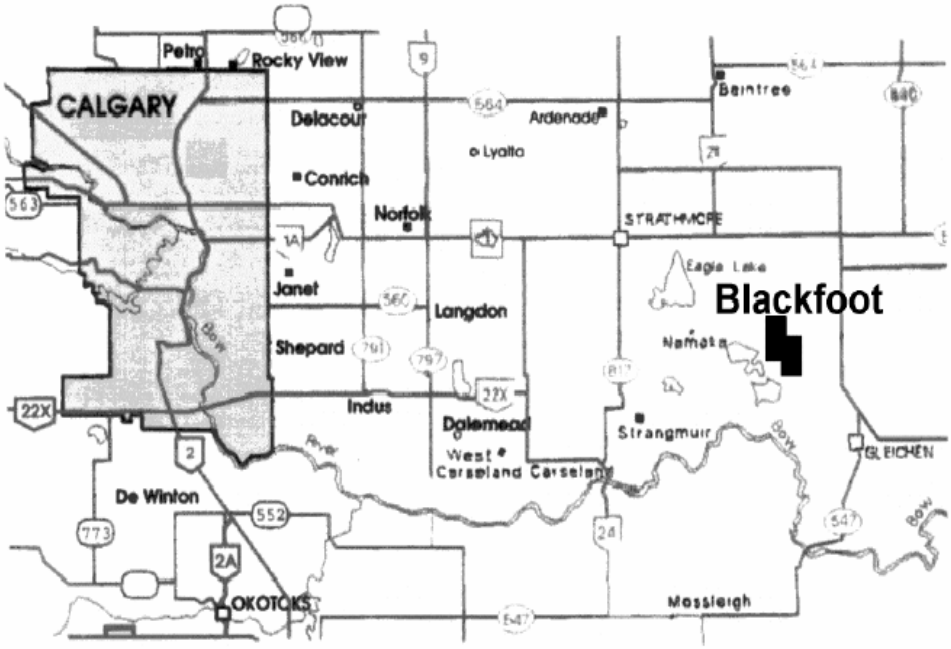

Figure 3.1. Map showing the location of EnCana Blackfoot Field, Alberta

3.3 Geology

The geology of the Blackfoot Field has been described several authors (e.g., Miller, 1996). Stratigraphically, the reservoir region consists of three Formations; these are, in the order of younging, the Mississippian of Mississippian age, the Mannville Group of Lower Cretaceous age and the Colorado Group also of Lower Cretaceous age (Figures 3.2 and 3.3). The Mannville Group is sub-divided into five Members; these are: the Detrital Member, Sunburst Member, Ostracod Beds, Glauconitic Member and the Blairmore (Figure 3.3). The Glauconitic Member is composed of several incised valleys (Figure 3.2); these valleys constitute the reservoir rocks. Capping the reservoir rocks is the Blairmore, which is overlain by the Colorado Group (Figures 3.2 and 3.3).

Structurally, the area is essentially of flat-lying geology and the main structural elements are erosional unconformities. The hydrocarbon trapping mechanism is mostly stratigraphic.

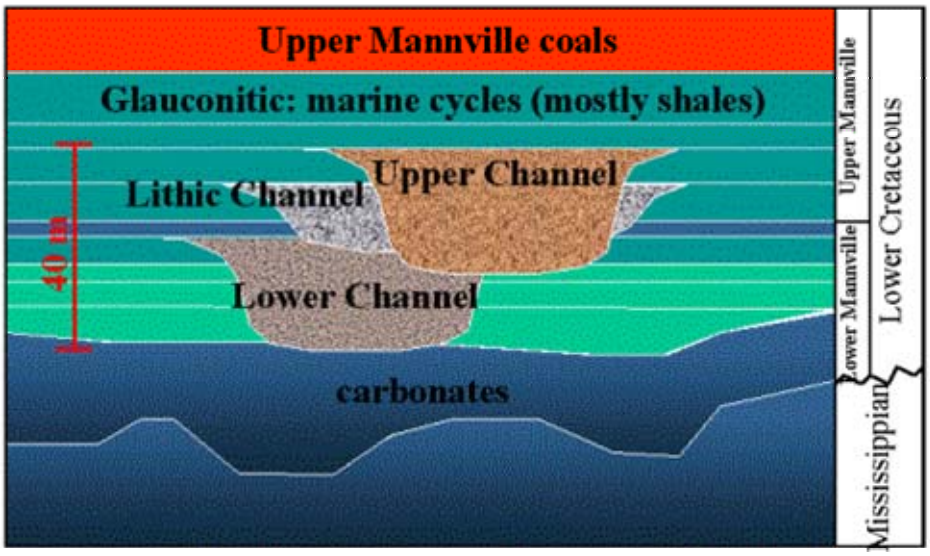

Figure. 3.2. Stratigraphy of the Blackfoot oil field, Alberta (Miller, 1996).

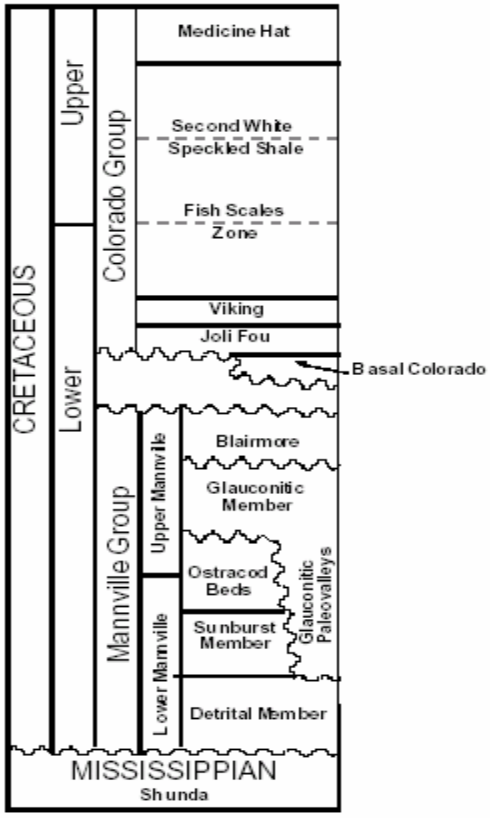

Figure 3.3. Stratigraphic sequence in the Blackfoot oil field, Alberta (Miller, 1996).

3.4 Seismic acquisition program

The seismic data used in this project came from a 2D-3C seismic survey (Blackfoot-97) acquired by the CREWES Project in 1997. The line runs from East to West (Figure 3.4); both the PP and PS data are available for this project. Following are the geometry-related information:

- Method of profiling: split-spread method
- Maximum spread length: 2989.17m
- Receiver interval: 20m
- Shot interval: 20m

- Total number of shots: 142
- Total number of receivers: 151.

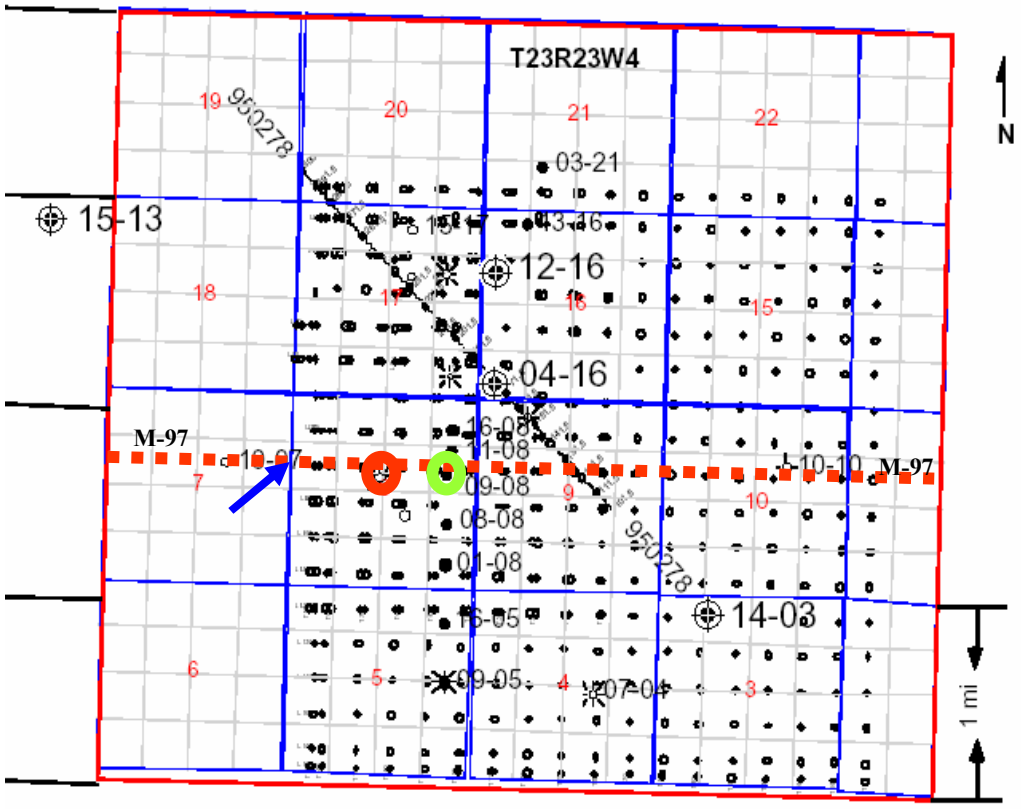

Figure 3.4. Seismic acquisition Base Map. The dashed-red line indicates the Blackfoot-97 survey line; the red circle indicates Well-11-08 location, while the green circle indicates Well-09-08 location. The blue arrow indicates the location of the first shot record. The location of the ACP gather 350 coincides with the Well-09-08 location and it is about 1.484 km (0.905 mi) from the first shot record.

3.5 Available Well data

Several wells have been drilled in this field; two of these, Well-11-08 and Well-09-08 were drilled along the line used in this project (Figure 3.4). Relevant well logs from these wells are shown in Table 3.1.

Table 3.1. Blackfoot available well-logs.

Well	P-Sonic	S-Sonic	Vp/Vs log	Density	Gamma-ray
11-08	Yes	No	No	Yes	Yes
09-08	Yes	No	Yes (VSP data)	Yes	Yes

3.6 Data preparation: processing in Promax

To apply the scanning methods to real data sets, the raw shots have to be processed to obtain the shot record and the ACP gathers needed for the semblance analysis. Processing was carried out in Promax environment and the processing sequences are enumerated below. As in the synthetic case discussed in chapter 2, both PP and PS processing sequence is about the same; the differences lie in the CCP/ACP gathers and the receiver statics applied to the PS-wave data. The following is an outline of the basic processing flow that I applied to the data sets.

1. Geometry definition (applied to both the PP and PS [radial channel] data).
2. First break picking / GLI 3D refraction statics correction (applied onto PP data only)
3. Elevation correction
4. True amplitude recovery (TAR).

5. Surface-wave noise attenuation
6. Surface consistent deconvolution
7. Bandpass filtering
8. Time-variant spectral whitening
9. Trace editing: Kill bad traces / reverse polarity of desired traces
10. Hand statics Receiver statics) applied to PS data only
11. Display shot records and export needed PS shot record to Matlab for semblance analysis.
12. PS- asymptotic binning (only for PS-wave data). Sort data into ACP gathers and export desired ACP gathers to Matlab for semblance analysis.
13. Sort data into CDP gathers only for PP data
14. AGC, bandpass filter, and Velocity analysis
15. NMO correction, Stack and migrate the data sets.

The results from steps 1 to 12 are shown in Figures 3.5 and 3.6.

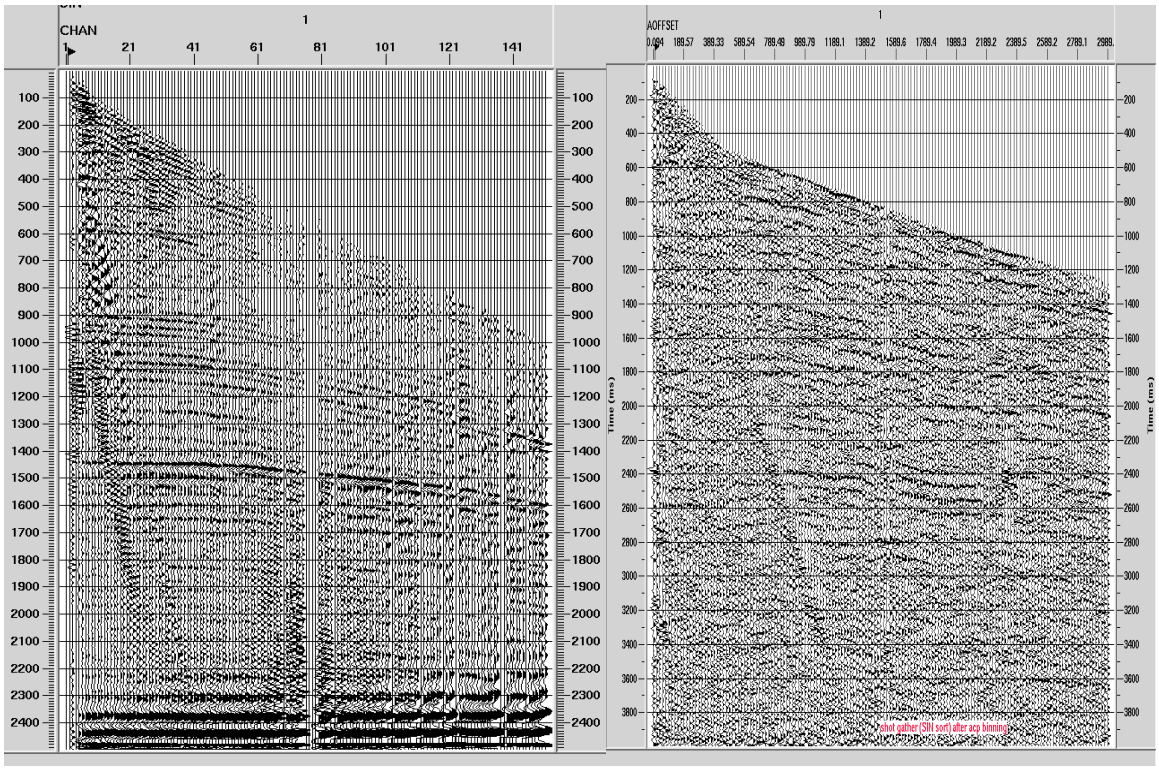

PP shot record PS shot record (Radial channel)

Figure 3.5. PP- and PS-wave shot gather from shot 1.

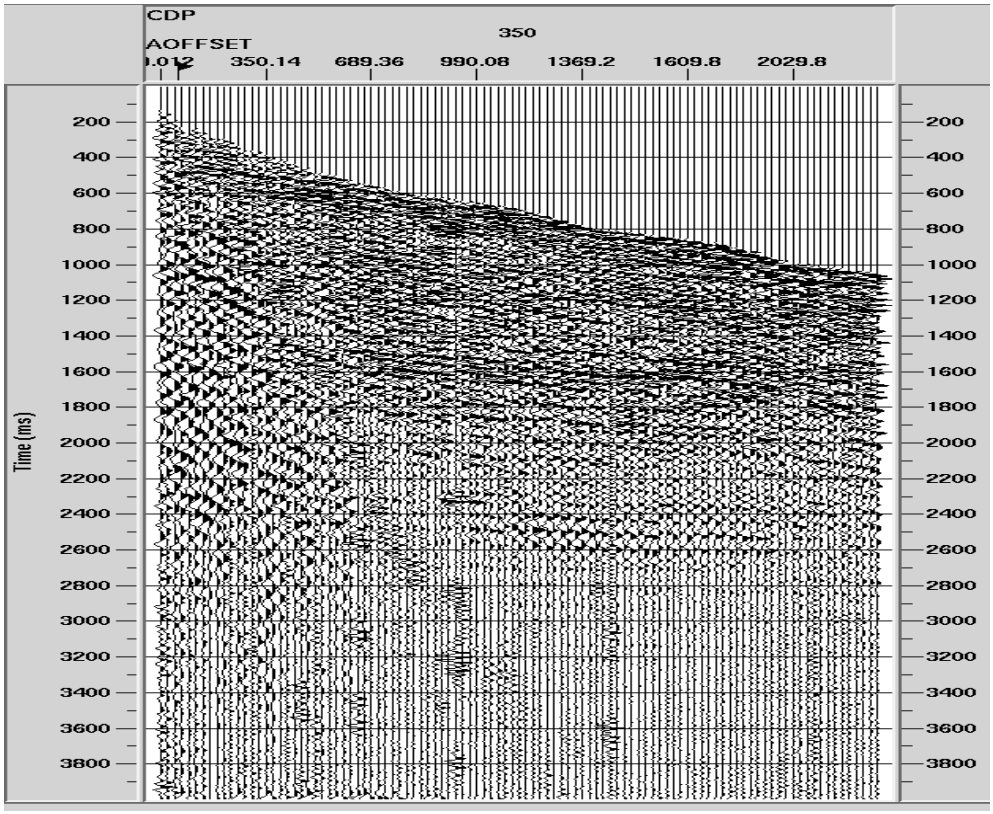

Figure 3.6. Radial channel (PS) ACP gathers from ACP location 350

The shot record and ACP gathers from steps 1 to 12 above were shipped to the Matlab environment where I subjected the data to semblance analysis for the purpose of γ_0 and stacking velocity scaning using the methods described in Chapter 2. The Timeslice Method was applied to the ACP gathers, while the Log-type Method was applied to both the shot and ACP gathers.

3.7 Dual-parameter scan: Timeslice Method

To perform the 3D semblance analysis, I used a range of velocities from 500 to 4500 m/s at intervals of 100 m/s; while the γ_0 values ranged from 1.5 to 3 at intervals of 0.05. The time sampling interval was 20 ms; i.e., semblance computation was performed every 20

ms. As already discussed in Chapter 2, the output from this computation is a 2D semblance display as well as the 3D semblance (volume). From the 2D semblance, I picked the stacking velocities and the corresponding PS two-way times. I then exported the 3D volume to the slicing program; and, at the picked times, timeslices (γ_0-V_{ps}-planes) were generated. Figure 3.7 shows the seismic section, the 2D semblance and the 3D volume displayed side by side. To demonstrate results from real data sets, timeslices from only three horizons are displayed in Figures 3.8 to 3.13. In these Figures, the white circles indicate the location of maximum semblance, while the scanned γ_0 values and stacking velocities are annotated as shown. Table 3.2 summarizes the results from the Timeslice Method.

Table 3.2. Real data example: Summary of results from Timeslice Method

PS-times (seconds)	Scanned PS-velocities (m/s)	Scanned γ_0
0.500	1700	2.15
1.200	2100	1.75
1.400	2300	1.85
1.530	2500	1.80
1.800	2600	1.70
2.400	3050	2.025
3.000	3200	2.22
		Average γ_0 = 1.93

The next step in this method is to generate a γ_0-function; I did this by interpolating the scanned γ_0 values with respect to time and then plotted the result. The output from this is shown in Figure 3.14. To check how valid this result is, the function was converted to depth using the equation derived below.

3.7.1 Depth conversion and comparison of scanned Vp/Vs with Well-09-08 results

From equation (2.15), we have

$$t_{p0} = \frac{2t_{ps0}}{1+\gamma_0}. \tag{2.15}$$

From equation (2.20), we have

$$V_p \cong V_{ps}\gamma_0^{0.5}. \tag{3.1}$$

Since the area of work is essentially of flat-lying geology, I assumed that P-wave stacking velocity is approximately equal to the average velocity (Al Chalabi, 1974). Thus, combining equations (2.15) and (3.1) and dividing the two-way traveltime by 2, we have,

$$Depth = \frac{1}{2}(V_p t_{p0}) = \frac{V_{ps} t_{ps0} \gamma_0^{0.5}}{1+\gamma_0} \tag{3.2}$$

Using equation (3.2), and the PS-wave stacking velocities, the corresponding times were transformed to depths; computed depth values were then plotted against corresponding γ_0 values. The resultant γ_0-log plot is compared with the γ_0-log plot from Well-09-08 in Figure 3.15. Though the scanned γ_0 values are slightly lower than the well results, the function does follow the well trend.

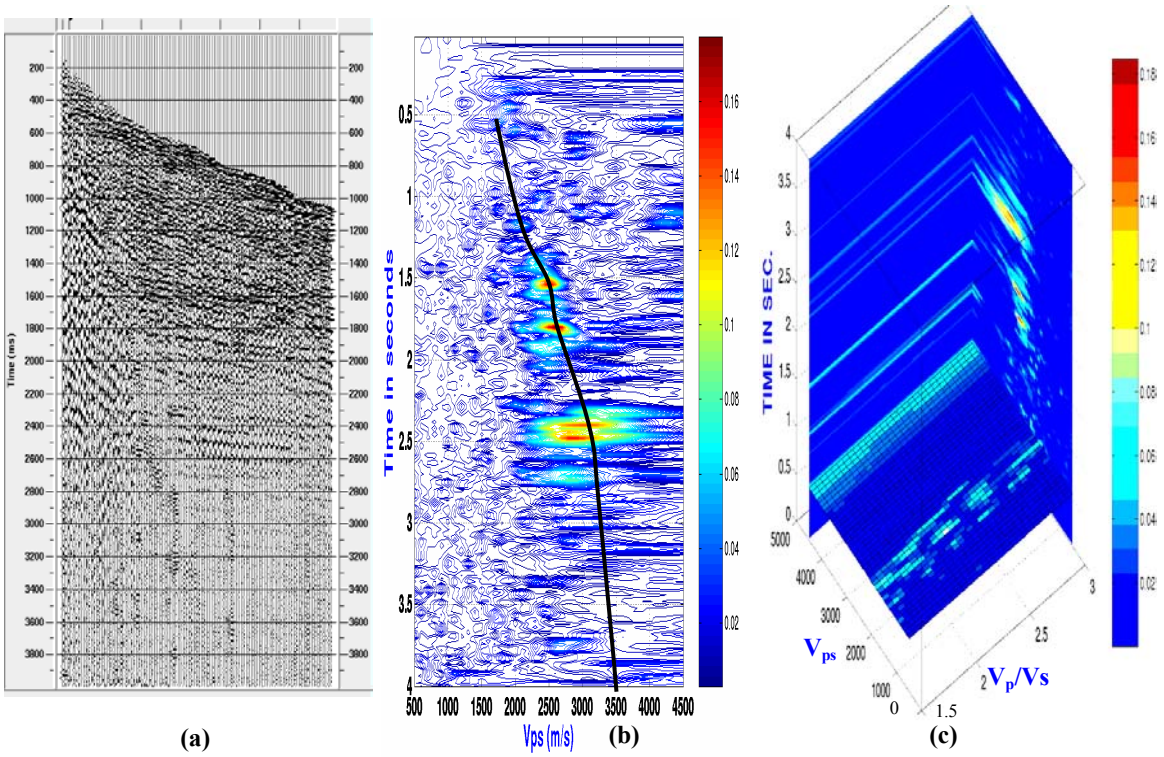

Figure 3.7. Display of the seismic ACP gathers (a), 2D velocity semblance (b), and the 3D semblance volume (c) from real data set.

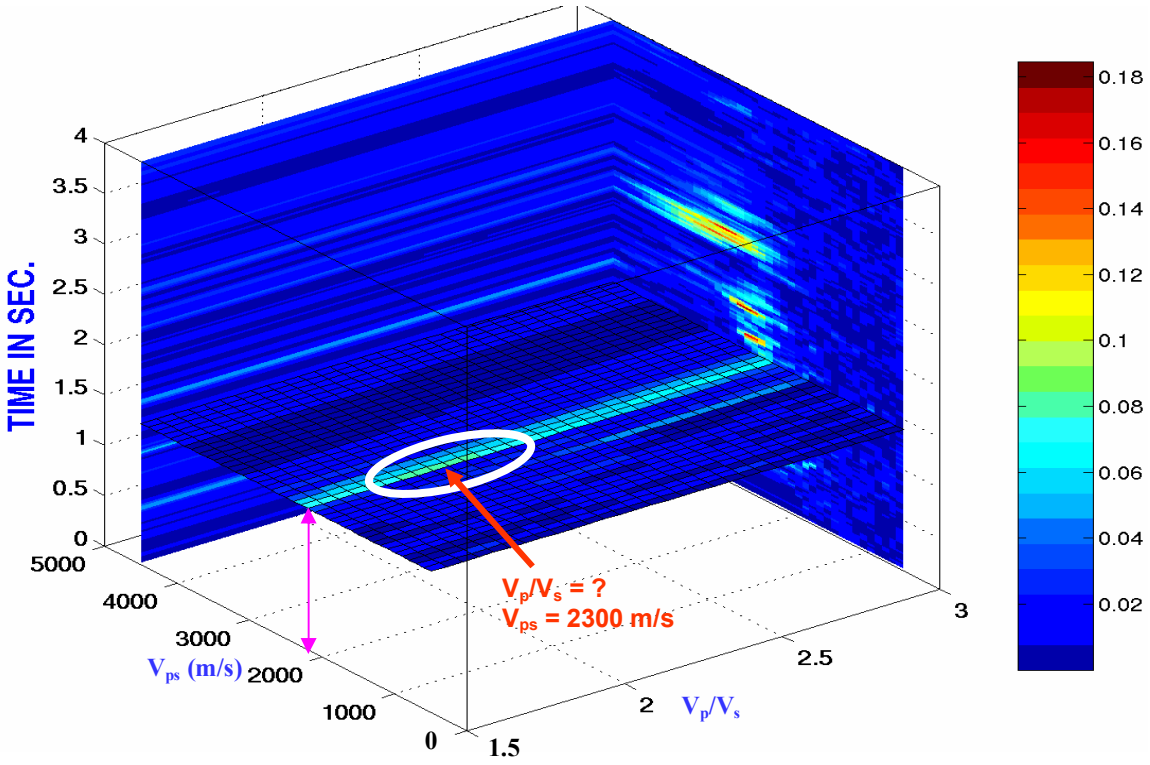

Figure 3.8. Timeslice at 1.4 seconds prior to colorbar scaling; the purple double-headed arrow indicates scanned velocity value along the velocity axis, while the red arrow and white circle show the location of maximum semblance. The scanned γ_0 is not quite clear thus, would require colorbar scaling to isolate it. However, the stacking velocity value is 2300 m/s.

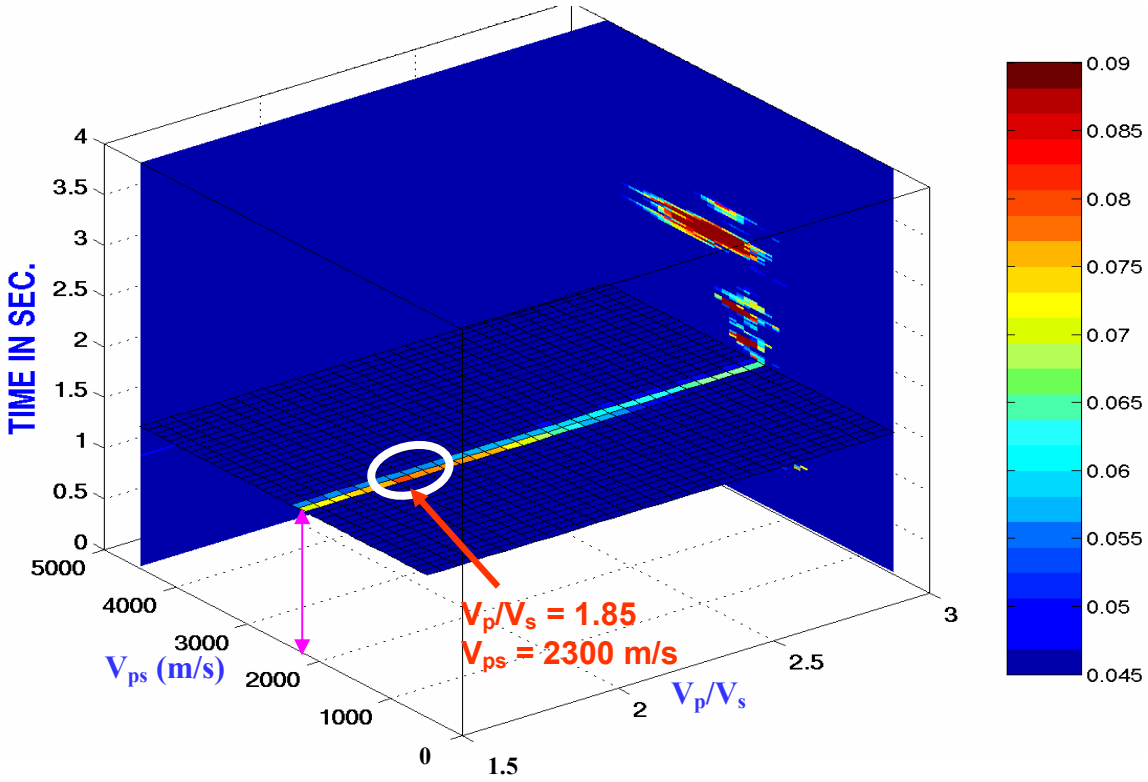

Figure 3.9. Timeslice at 1.4 seconds after colorbar scaling; location of γ_0 is now very visible and the scanned γ_0 value is 1 .85 while the stacking velocity is 2300 m/s.

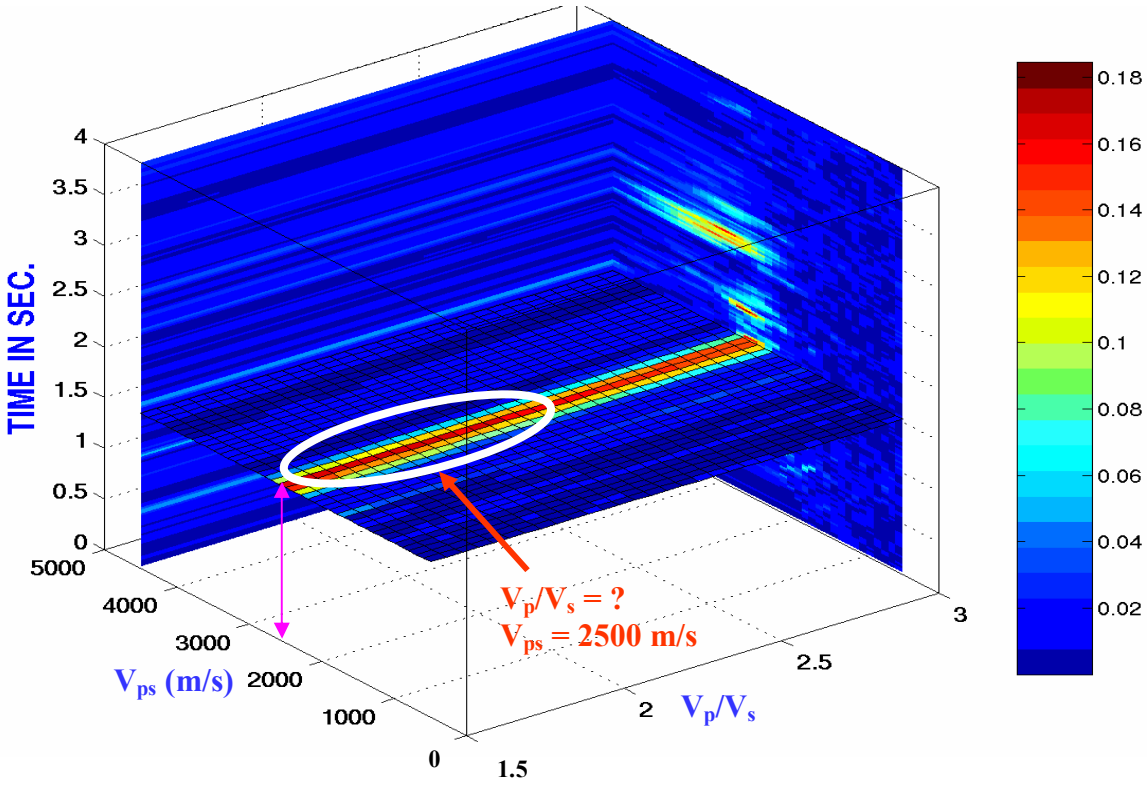

Figure 3.10. Timeslice at 1.5300 seconds prior to colorbar scaling; the purple double-headed arrow indicates scanned velocity value along the velocity axis, while the red arrow and white circle show the location of maximum semblance. The scanned γ_0 is not quite clear thus, would require colorbar scaling to isolate it. However, the stacking velocity value is 2500 m/s.

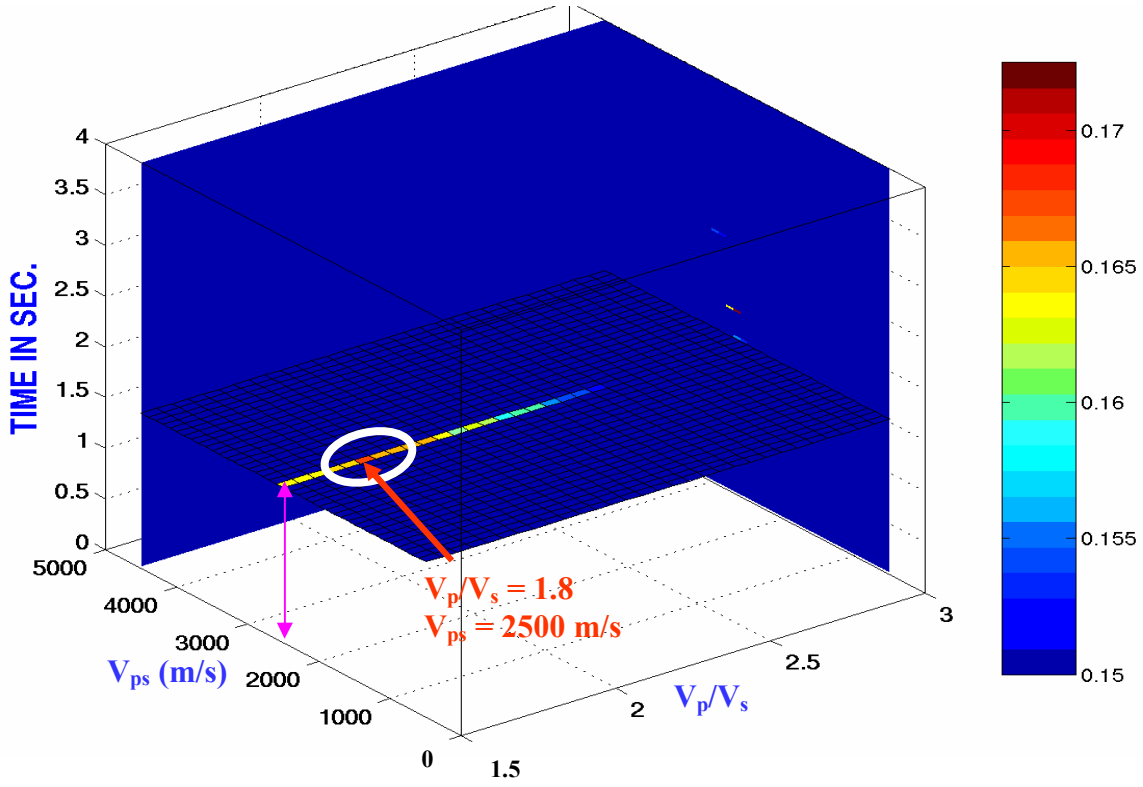

Figure 3.11. Timeslice at 1.5300 seconds after colorbar scaling; location of γ_0 is now very visible and the scanned γ_0 value is 1 .8 while the stacking velocity is 2500 m/s.

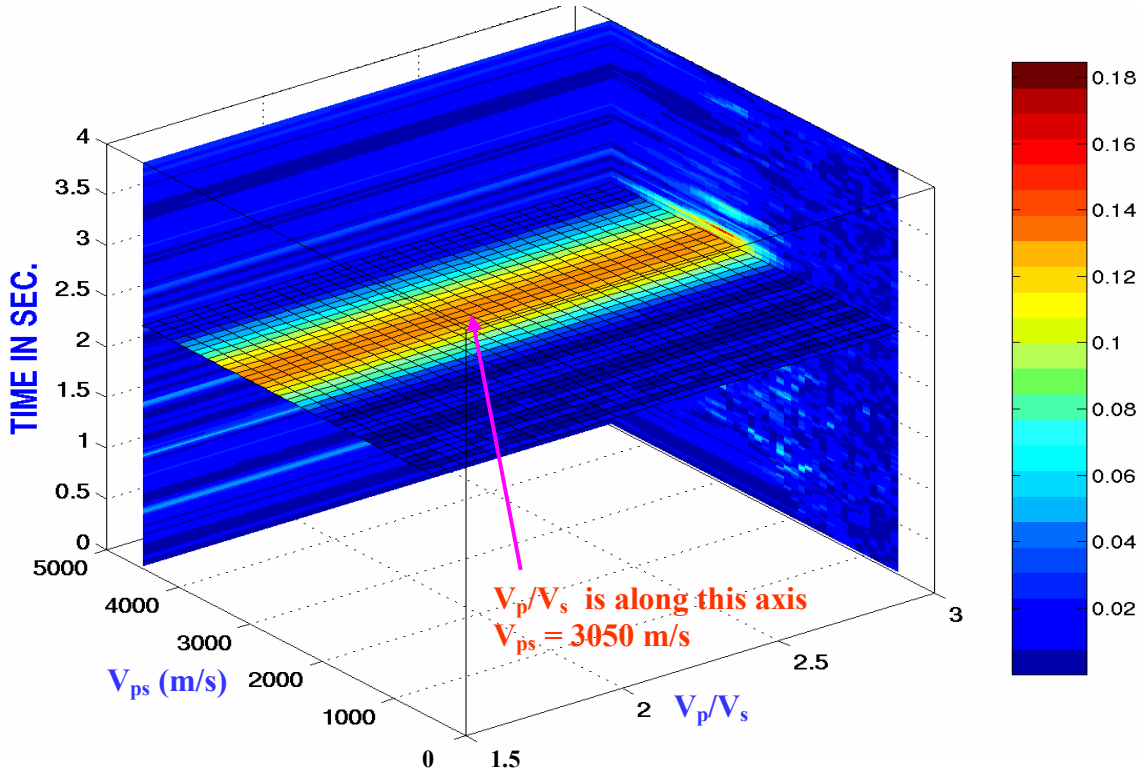

Figure 3.12. Timeslice at 2.400 seconds prior to colorbar scaling; the purple arrow indicates the line along which maximum semblance could be located. It would require some colorbar scaling to identify it. (See Figure 3.19).

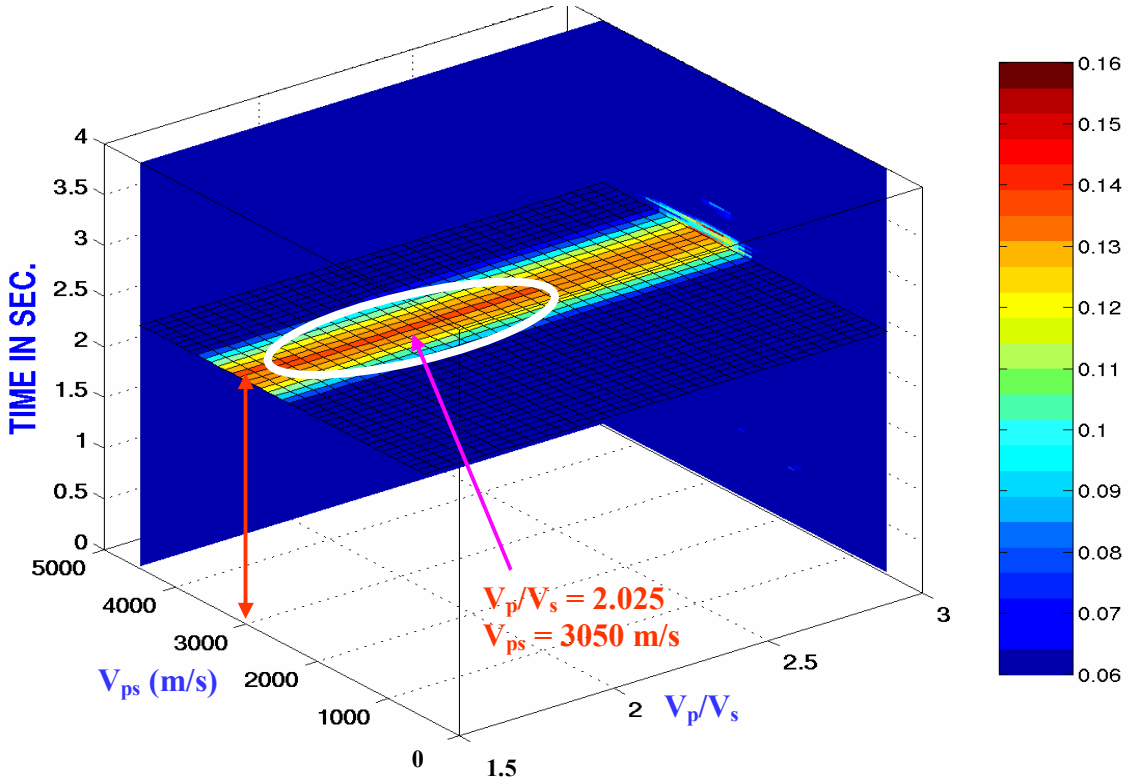

Figure 3.13. Timeslice at 2.400 seconds after colorbar scaling; location of maximum semblance is now visible. The γ_0 value is taken as the midpoint of maximum semblance and its value is 2.025; while the scanned velocity is shown by the red double-headed arrow, at a value of 3050 m/s along the velocity axis.

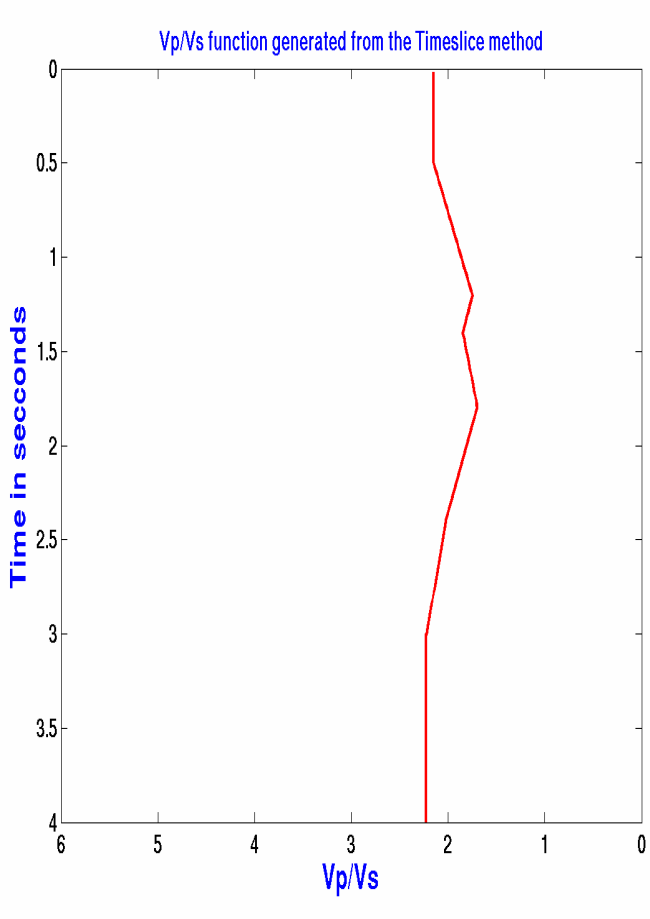

Figure. 3.14. V_p/V_s function from the Timeslice Method: Real data case example.

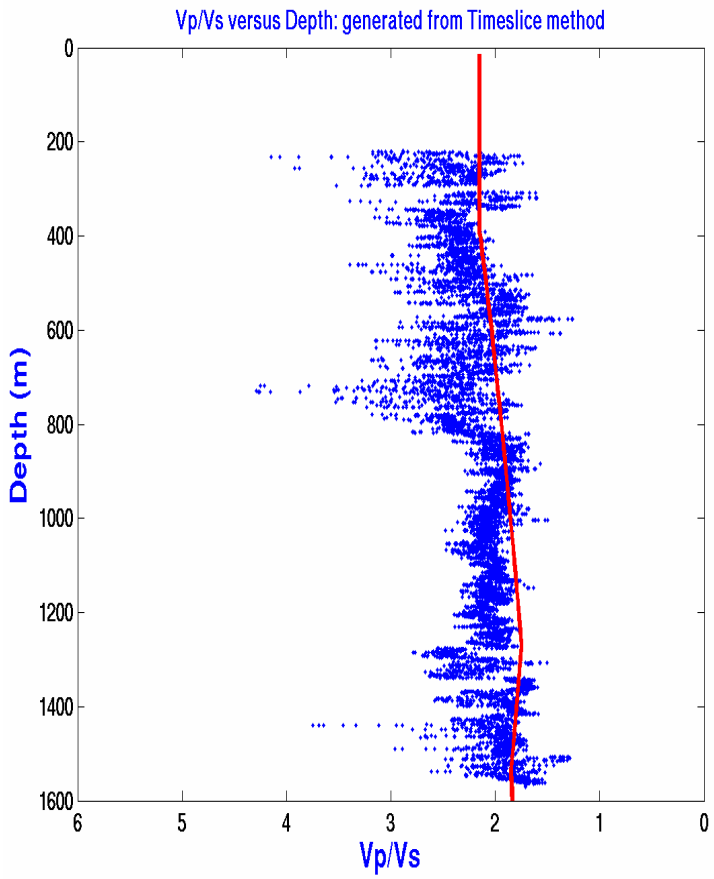

Figure. 3.15. Comparison of the V_p/V_s function from the Timeslice Method (red curve), with V_p/V_s log from Well-09-08 (blue curve). Results from this method consistently show lower Vp/Vs values. The reseon for this is not quite clear. However, an error margin say +10% could be used to correct the scanned Vp/Vs values to the approximate true Vp/Vs values. This error margin can be established after a number of tests.

3.8. Dual-parameter scan: Log-type Method using ACP gathers

In applying this method, I used a range of γ_0 values from 1.5 to 3.0, and sampling at 0.025 intervals. The velocity range is also the same as the one used in the Timeslice Method starting at 500 m/s to 4500 m/s, but sampling at intervals of 25 m/s. The time ranged from 0.02 second to the end of the record time (4.0 seconds) at intervals of 0.02 second. I subdivided the whole volume into 11 sub-volumes to give 11 2D velocity semblance panels. From these, I obtained the final 2D velocity semblance and the 2D γ_0 panels as described in Chapter 2. Using the final 2D semblance display, I picked the stacking velocities and the corresponding two-way times. These time-velocity coordinate pairs were transferred to the 2D γ_0 panel from where associated γ_0 values are automatically picked and plotted. Results from this method are shown in Figures 3.16 to 3.20. Out of the 11 semblance panels, only the 1st and the 11th panels are displayed (Figures 3.16). Figure 3.17 shows the final 2D velocity semblance and the 2D γ_0 panels, while Figure 3.18 shows the 2D semblance, 2D γ_0 panel and the scanned γ_0-time log. In Figure 3.19, I combined the seismic (ACP gathers) with Figure 3.18, to display four panels. After converting to depth, as discussed in (3.6.1.) above, I compared the scanned V_p/V_s log with that from Well-09-08. Figure 3.20 shows this comparison; it can be seen that the scanned results compare very well with the Well-09-08 log data. In this figure, the right panel shows the smoothed V_p/V_s-time log using a 7-point moving average. Overall, this method gives very good results.

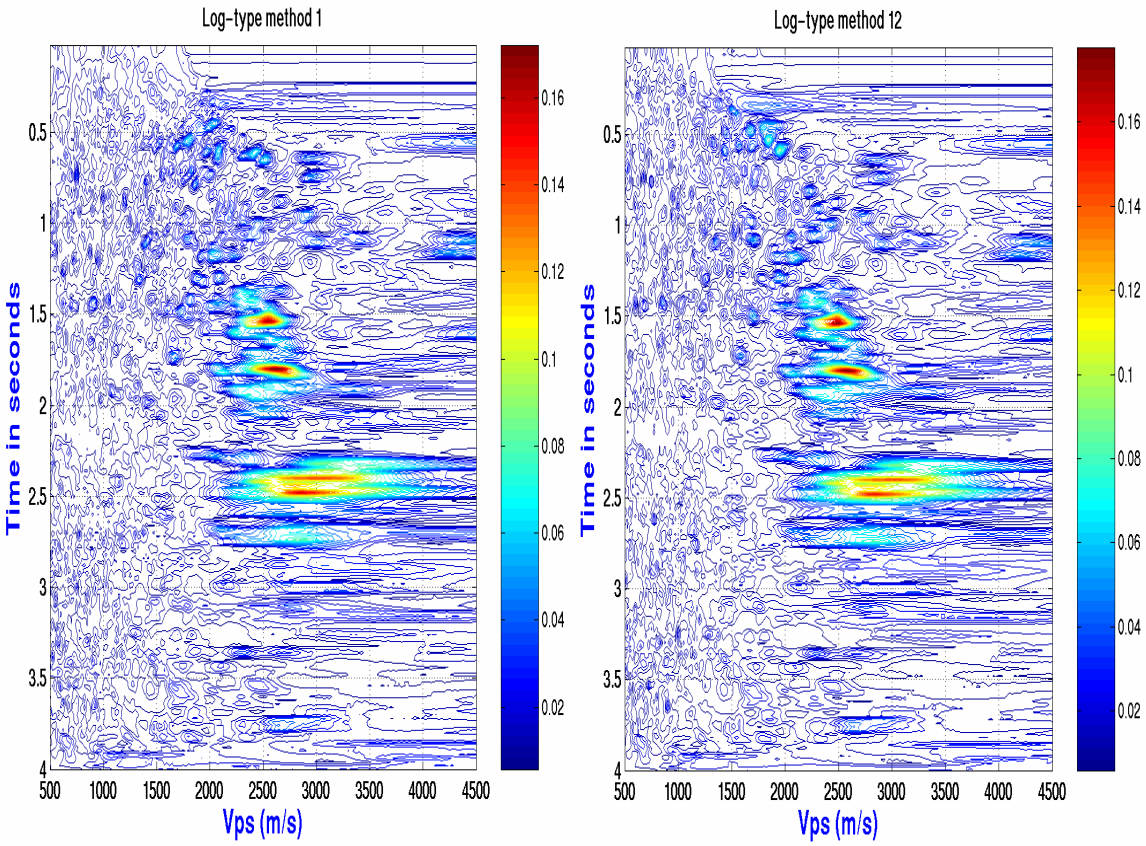

Figure. 3.16. Velocity semblance from panel 1, (left) and panel 11, (right). The V_p/V_s values used in generating these panels are respectively 1.55 and 2.8. Notice the differences in the intensities of maximum semblance at the various horizons. The scale of the colorbar range from 0.0 to 0.18; this indicates that the semblance values lie between 0.0 and 0.18.

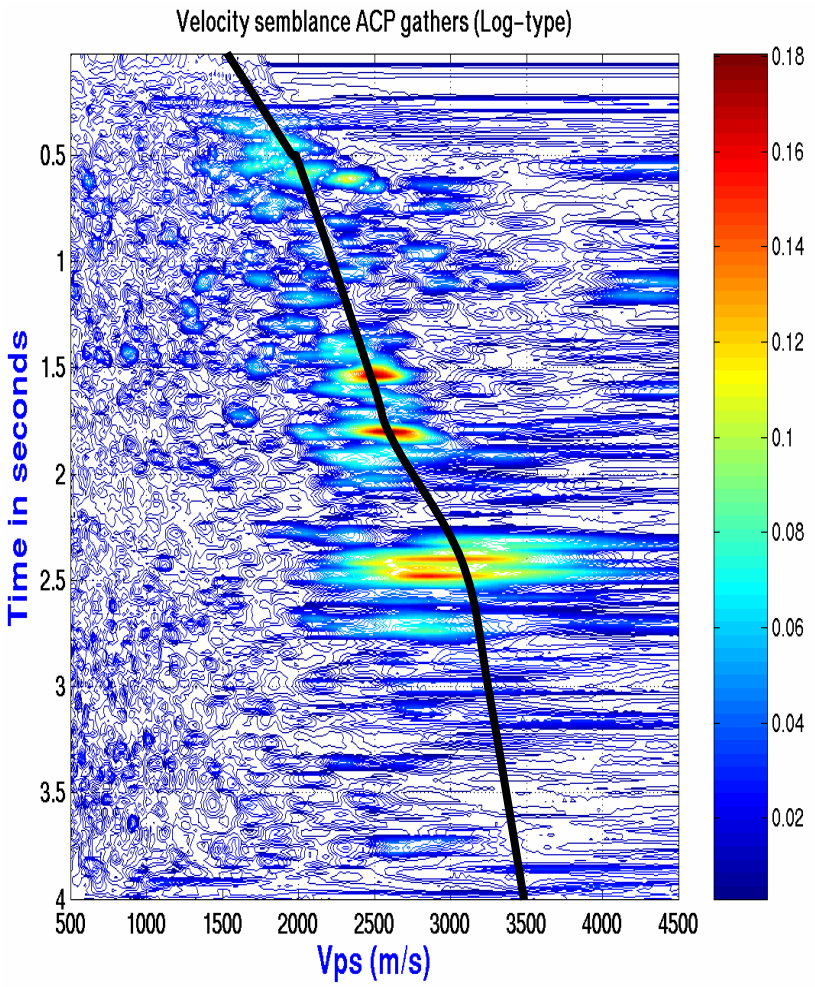

Figure. 3.17. Final 2D velocity semblance panel from the Log-type Method. Superposed on it, is the velocity function picked at the locations of maximum semblance. From the scale of the colorbar, the values of semblance lie between 0.0 and 0.18.

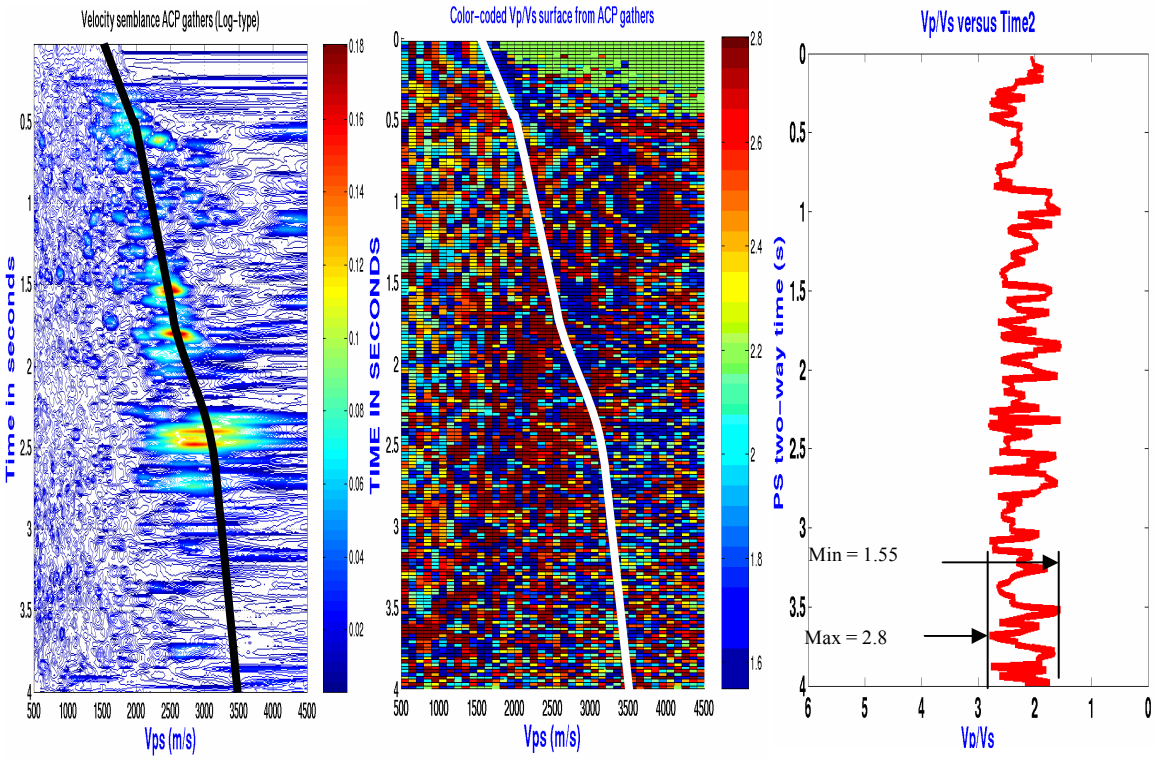

Figure 3.18. 2D velocity semblance panel (left), the 2D γ_0 panel (center), and the scanned γ_0-time log (right). Superposed on the 2D γ_0 panel, is the velocity function (white) derived from the 2D velocity semblance panel (shown in white). The semblance scale range from 0.0 to 0.18, while the scanned γ_0 values range from 1.55 to 2.8. The apparent oscillation that is seen between about 2.9 to 4.0 second could be due to the fact that no true reflection event was pick from the velocity semblance panel since; this can also be seen from the seismic ACP gathers.

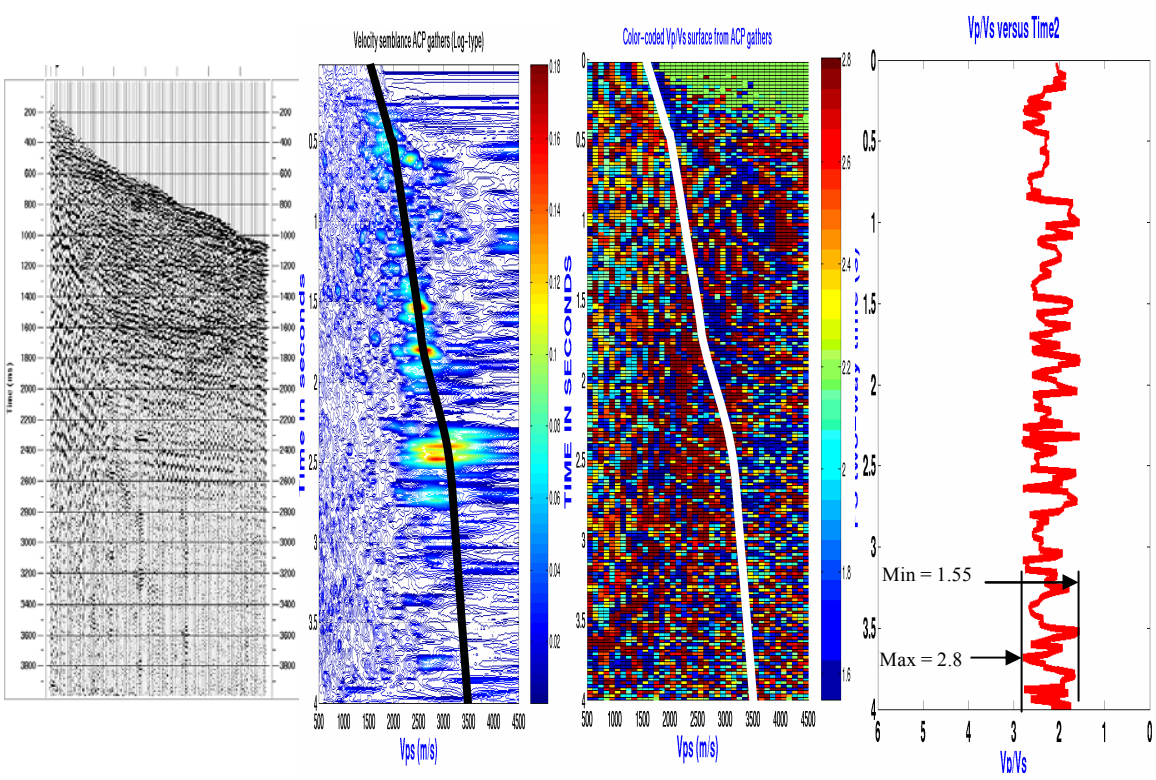

Figure 3.19. In this display, the seismic data (extreme left) is added to Figure 3.18. The seismic ACP gather comes from ACP gather 350 location. This figure is displayed here to demonstrate what the screen will look like when, the program becomes fully automated. That is, as one clicks on the maximum semblance, the event will be seen on the seismic record, and the V_p/V_s-time log will be traced out as well. The semblance scale range from 0.0 to 0.18, while the scanned γ_0 values range from 1.55 to 2.8.

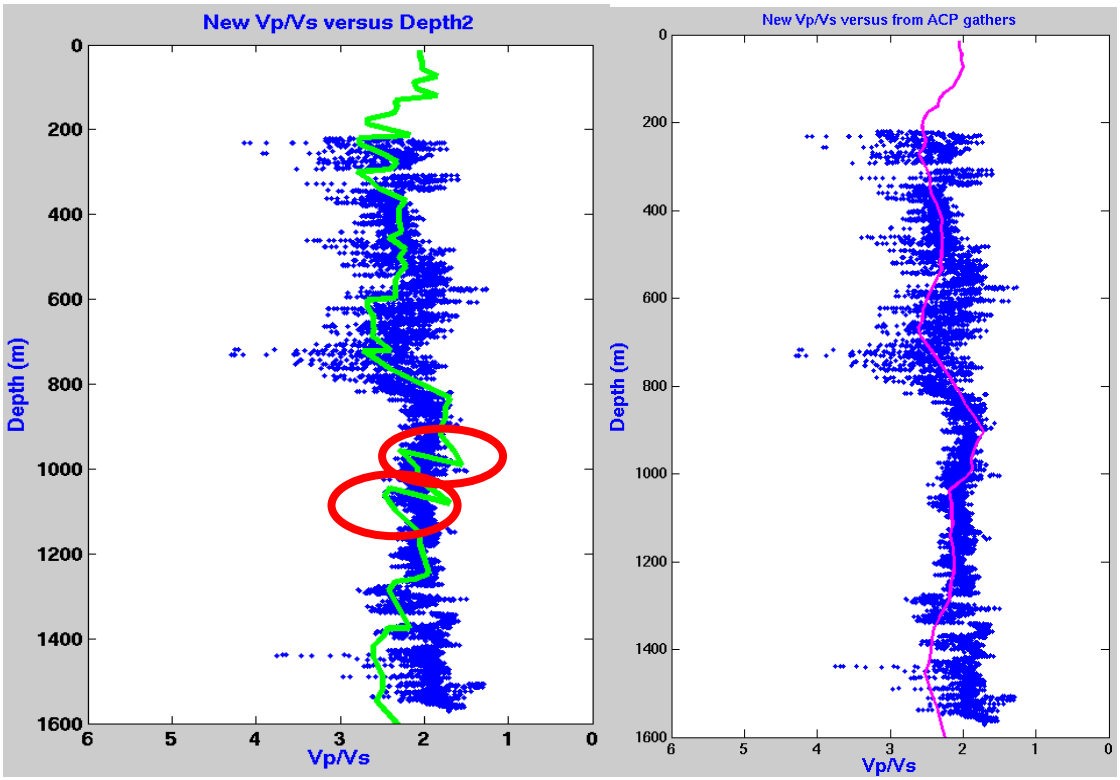

Figure 3.20 (a). Comparison of the V_p/V_s log from the Log-type Method (green curve) with the Vp/Vs log from Well-09-08 (blue curve). The purple curve in the right panel is the smoothed version of the green curve. It was smoothed using a 7-point moving average. The green curve in the left panel comes from the V_p/V_s values that are encountered by the velocity function when transferred on to 2D γ_0-panel. The curve is calculated automatically once the velocity function is transferred to the 2D γ_0-panel. From the right panel it can be seen that the scanned V_p/V_s log (purple curve) matched the Well-09-08 V_p/V_s log reasonably well. The red circled-region are zones where the scanned V_p/V_s value either exceeds or equals the preceding value. In such areas, the calculated depth value is either smaller than or is equal to the preceding depth value. To avoid this problem, it is necessary to smooth the scanned γ_0 values.

3.9. Dual-parameter scan: Log-type Method using Shot gathers

In this test, all variables remain the same as in section (3.7); the only difference lies in the input data. A shot gather from the first shot record was used as the input instead of ACP gathers. Results are shown in Figures 3.21 to 3.25. From Figure 3.25, it can be seen that this also gives very good results.

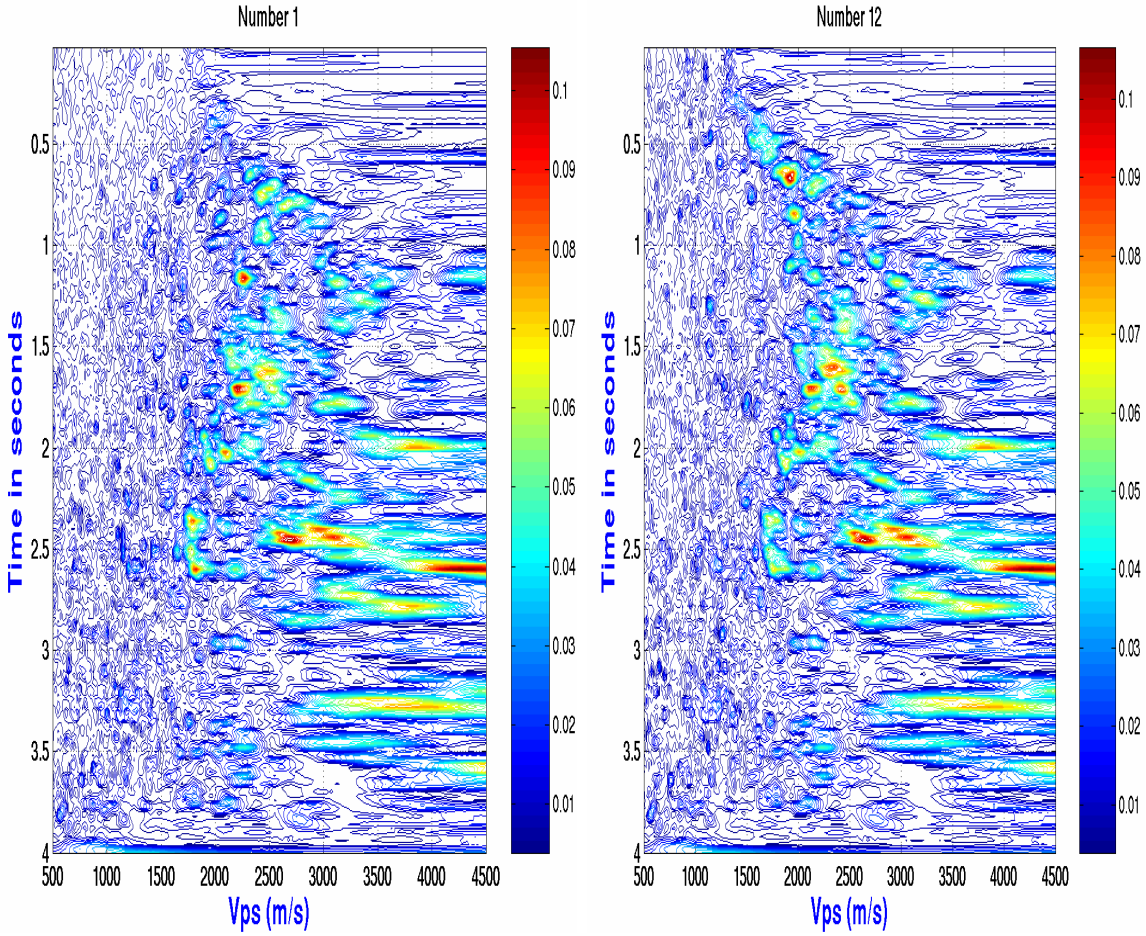

Figure 3.21. Velocity semblance from panel 1, (left) and panel 11, (right). The V_p/V_s values used in generating these panels are respectively 1.55 and 2.8. Notice the differences in the intensities of maximum semblance at the various horizons. The scale of the colorbar range from 0.0 to 0.11; this indicates that the semblance values lie between 0.0 and 0.11.

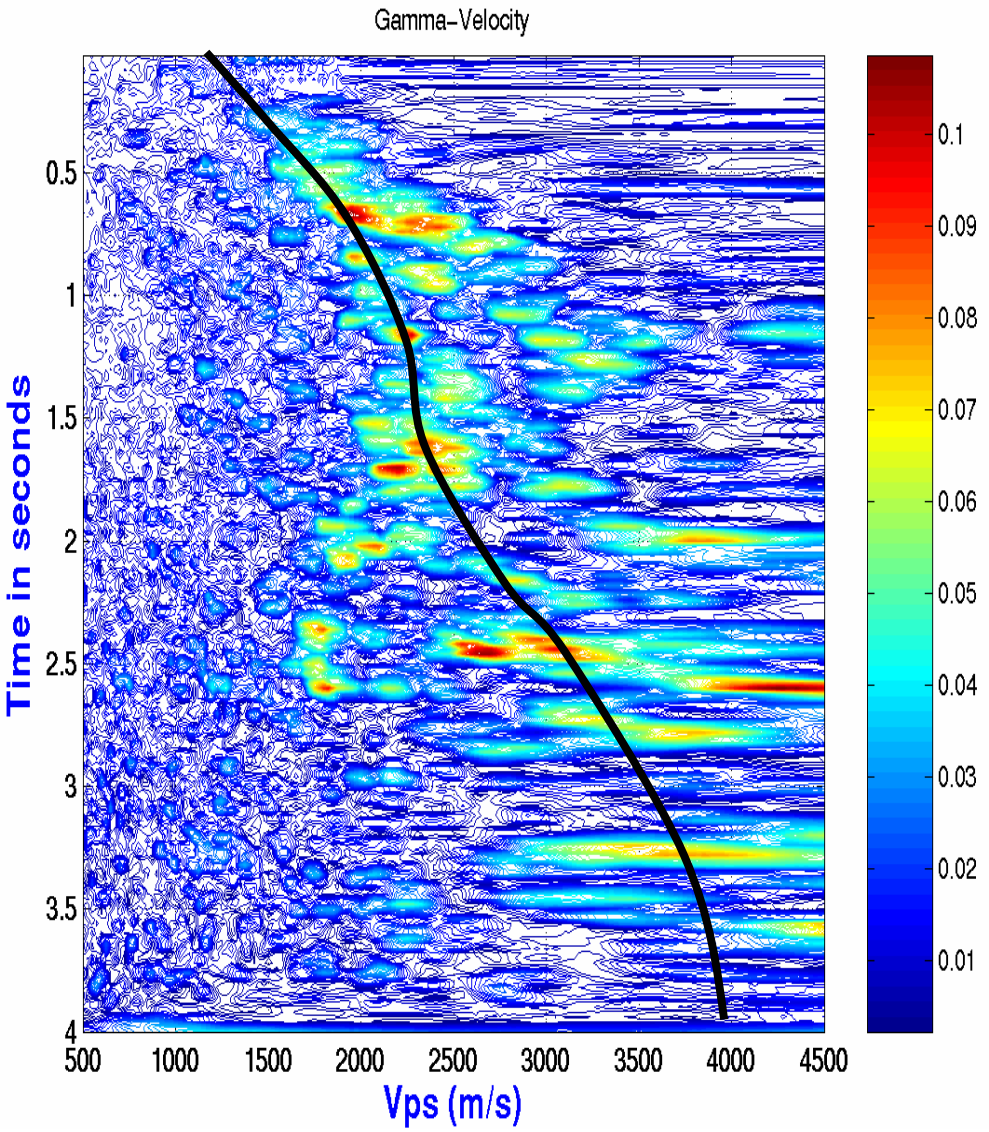

Figure 3.22. Final 2D velocity semblance panel from the Log-type Method. Superposed on it, is the velocity function through the locations of maximum semblance (From shot gathers). The scale of the colorbar range from 0.0 to 0.11; this indicates that the semblance values lie between 0.0 and 0.11.

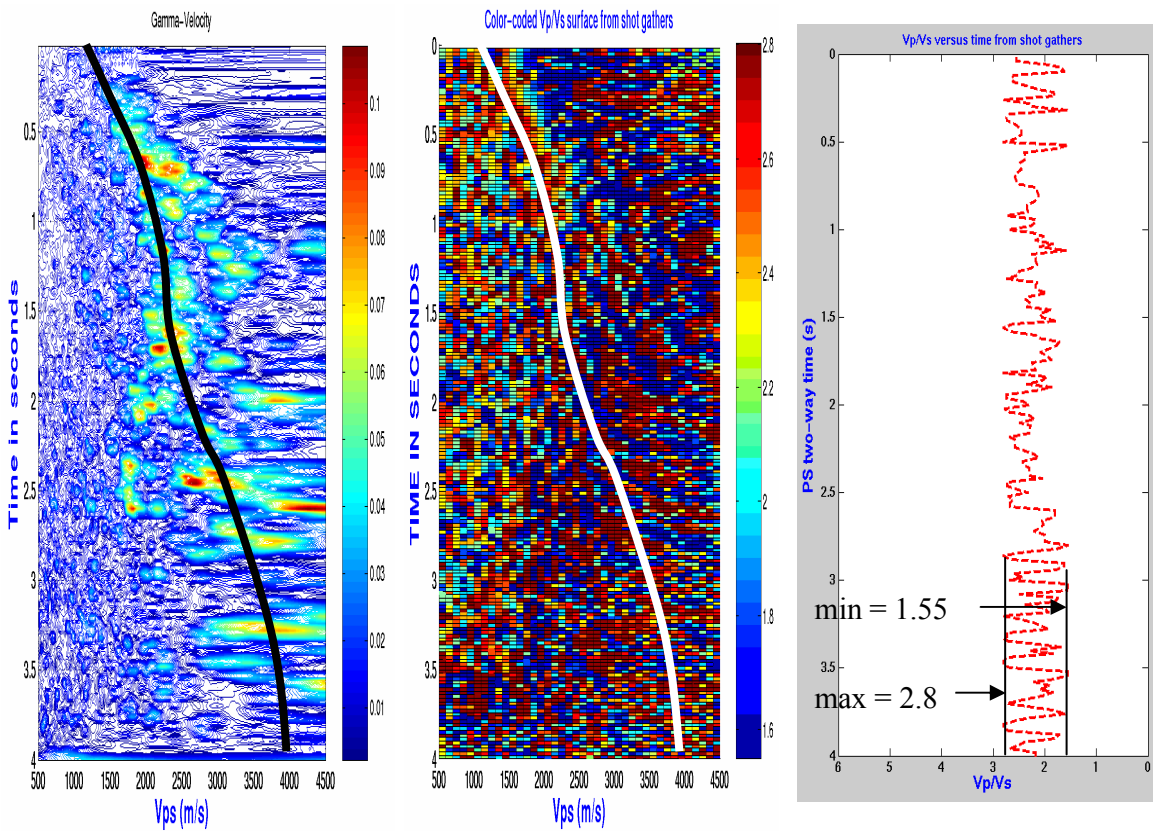

Figure 3.23. 2D velocity semblance panel (left), the 2D γ_0 panel (center), and the scanned γ_0-time log (right). Superposed on the 2D γ_0 panel, is the velocity function (white) derived from the 2D velocity semblance panel (shown in white). The semblance scale range from 0.0 to 0.11, while the scanned γ_0 values range from 1.55 to 2.8.

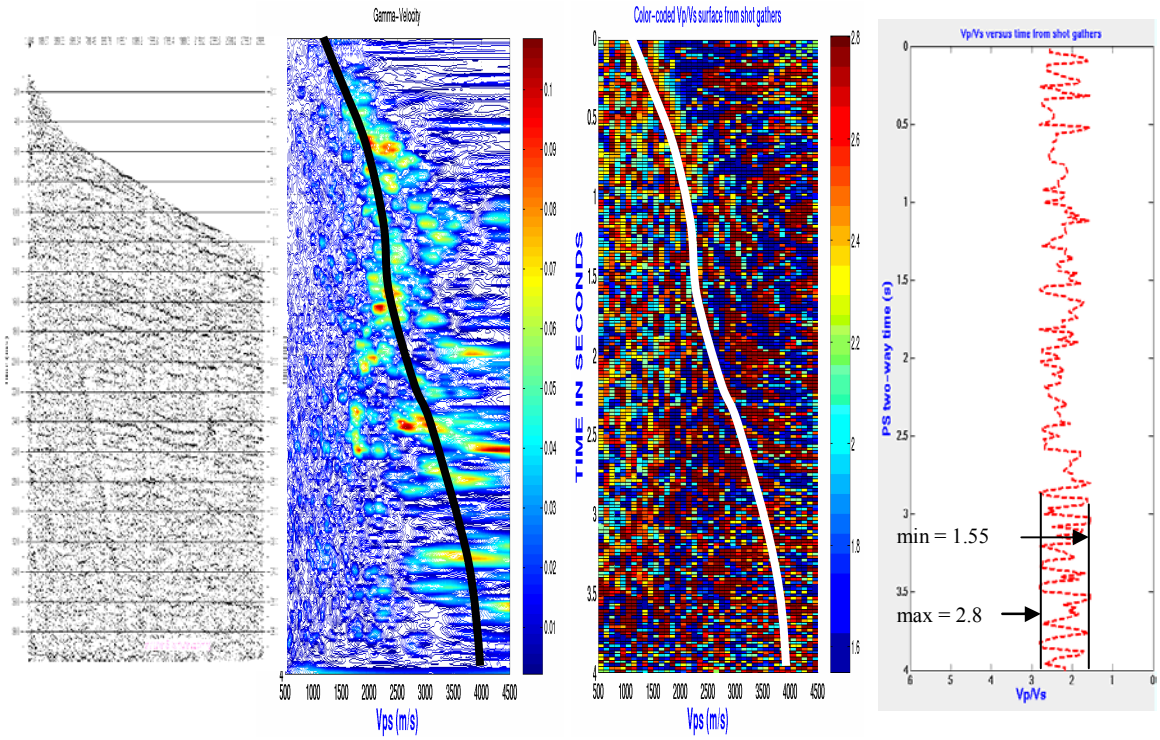

Figure 3.24. In this display, the seismic data (extreme left), is added to Figure 3.23. The seismic shot gather comes from shot record number 1. This figure is displayed here to demonstrate what the screen will look like when, the program becomes fully automated. That is, as one clicks on the maximum semblance, the event will be seen on the seismic record, and the V_p/V_s-time log will be traced out as well. The semblance scale range from 0.0 to 0.11, while the scanned γ_0 values range from 1.55 to 2.8.

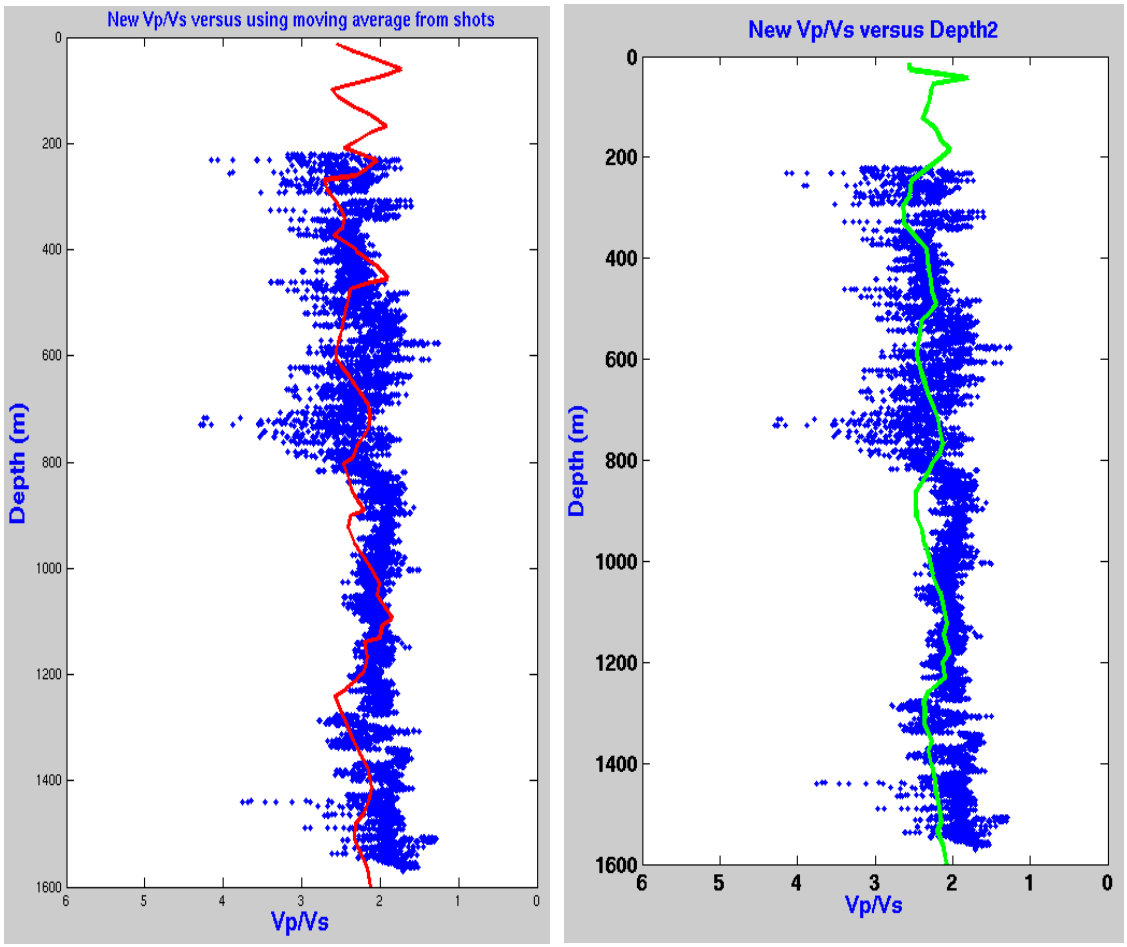

Figure 3.25 (a). Comparison of the Vp/Vs log from the Log-type Method (red curve) with the Vp/Vs log from Well-09-08 (blue curve). The green curve in the right panel is the smoothed version of the red curve. It was smoothed using a 7-point moving average. The red curve in the left panel comes from the V_p/V_s values that are encountered by the velocity function when transferred on to 2D γ_0-panel. The curve is spilled out automatically once the velocity function is transferred to the 2D γ_0-panel. From the right panel it can be seen that the scanned V_p/V_s log (green curve) matched the Well-09-08 V_p/V_s log reasonably well.

3.10. Dual-parameter scan: Comparison of the Timeslice and the Log-type Methods.

Scanned V_p/V_s logs obtained by the different methods within the interval logged by Well-09-08 were plotted together with Well-09-08 V_p/V_s log (Figure 3.26). The purpose is to determine the curve that best tracks the well. From this figure, it can be seen that the Log-type Method using -ACP gathers tracks the well results better than the others. This is because the ACP gather 350 location almost coincides with the Well-09-08 location; whereas, the shot record (first shot record) data location is 1.484 km (0.905 mi) from the well location (Figure 3.4). Thus there exist some lateral variations in V_p/V_s values between the Well-09-08 location and that of the first shot record.

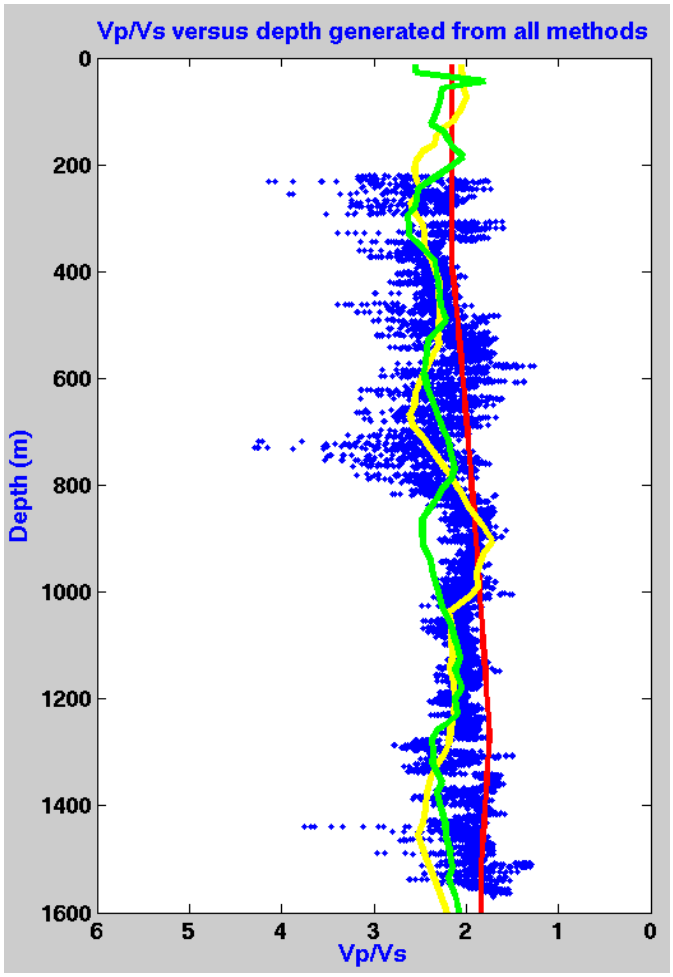

Figure 3.26. Comparison of the Vp/Vs-time-log from the Timeslice Method (red curve) and the Vp/Vs-time-logs from the Log-type Method using ACP and Shot gathers (yellow curve and green curve respectively). The yellow curve trends along the blue curve better than the others. This is because there are some lateral V_p/V_s variation between the Well-09-08 location, and the location of the first shot record. Overall, the three curves matched the well results reasonably well in the sense that the scanned V_p/V_s logs do not deviate significantly from the well results.

3.11. PS to PP time mapping

Having obtained a γ_0 function, the next step is to use the function to transform PS-times to PP-times. To do this, the Promax processing steps 12 to 15 in section (3.5) were performed; from whence I obtained the migrated stacked sections shown in Figures 3.27 and 3.28. The PS to PP time mapping was carried out using the steps already described in section (2.8.4.5.), and the three γ_0 functions obtained above. However, before using the V_p/V_s-time-logs obtained from the Log-type Method, I applied a 15-point moving average to the curves to derive γ_0-functions shown in Figure 3.29. These latter curves were used to transform the PS stacked data to P-wave times. Figures 3.30 to 3.32 display the transformed data sets. Figure 3.30 shows the transformed data using Timeslice function; while Figures 3.31 and 3.32 respectively show the transformed data using the Log-type functions from ACP and Shot gathers. Figure 3.33 shows the untransformed PS data, while Figure 3.34 compares the PP section with the untransformed PS section. The transformed data sets are compared with the PP stacked data in Figures 3.35 to 3.37. In Figure 3.38, the untransformed PS section is compared with the transformed section obtained from the Log-type Method using the Shot gathers as input data. The match is a perfect one; the only obvious difference between them is in time.

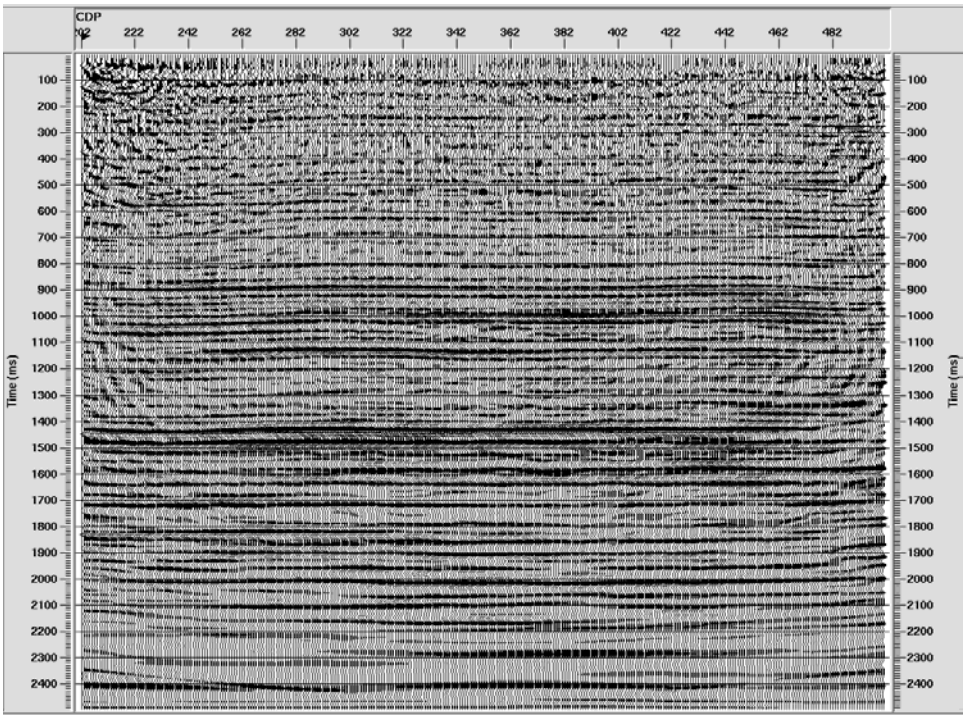

Figure.3.27. Blackfoot PP migrated stacked section from Promax

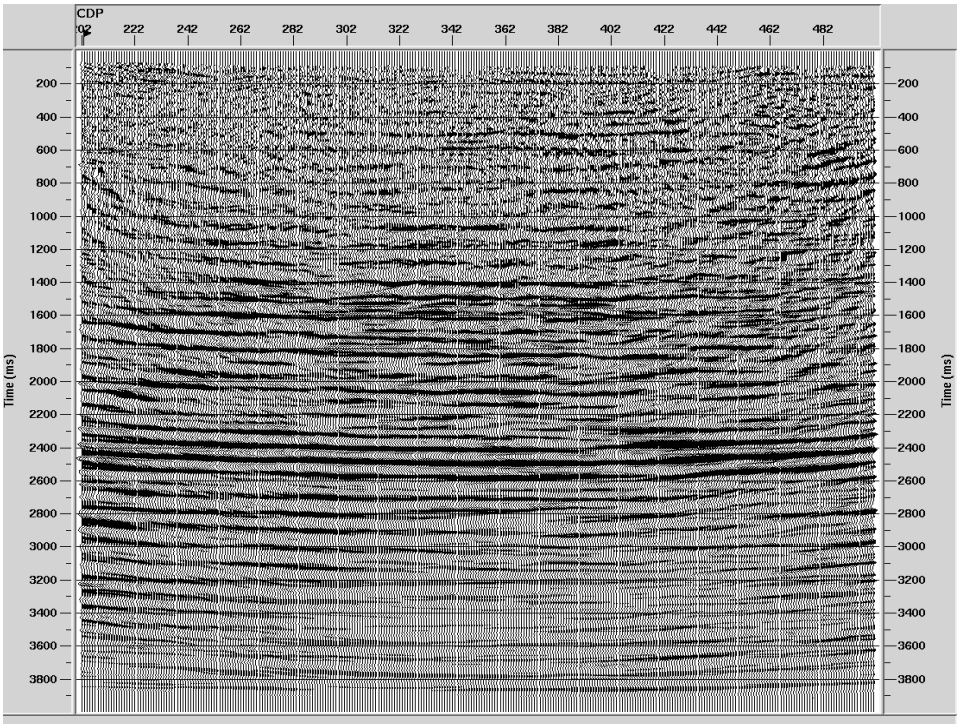

Figure 3.28. Blackfoot PS migrated stacked section from Promax

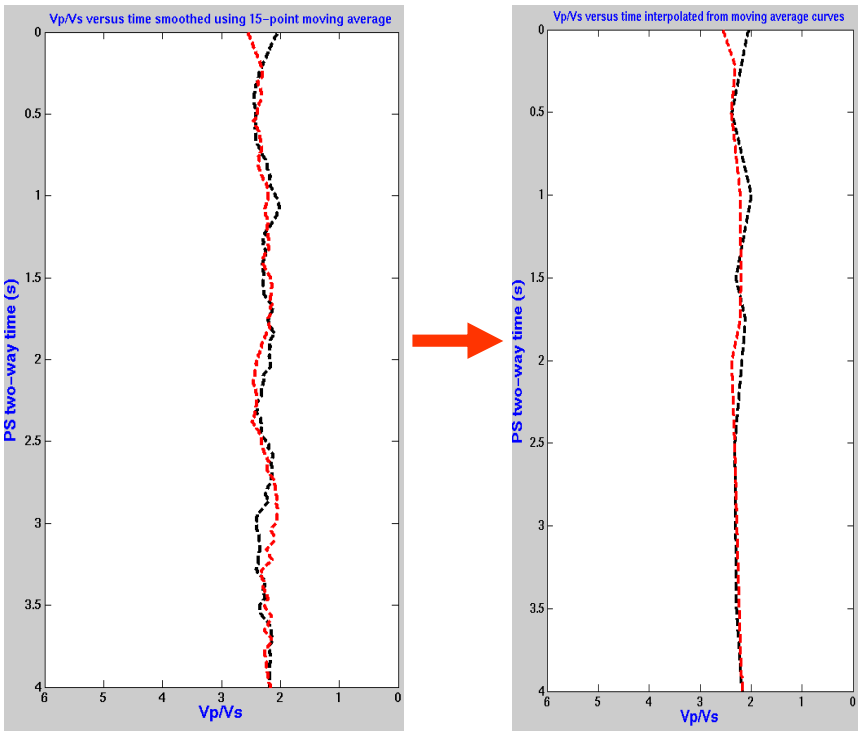

a b

Figure. 3.29. V_p/V_s functions from the Log-type Method. The plot to the left (a) was obtained by applying a 15-point moving average to the original curves. The resultant curves were then sampled every 500ms; V_p/V_s values obtained at these points were then interpolated every 1ms and plotted against time giving the curves shown in plot (b) to the right. The black curve came from the ACP gathers , while the red curve came from the Shot gathers.

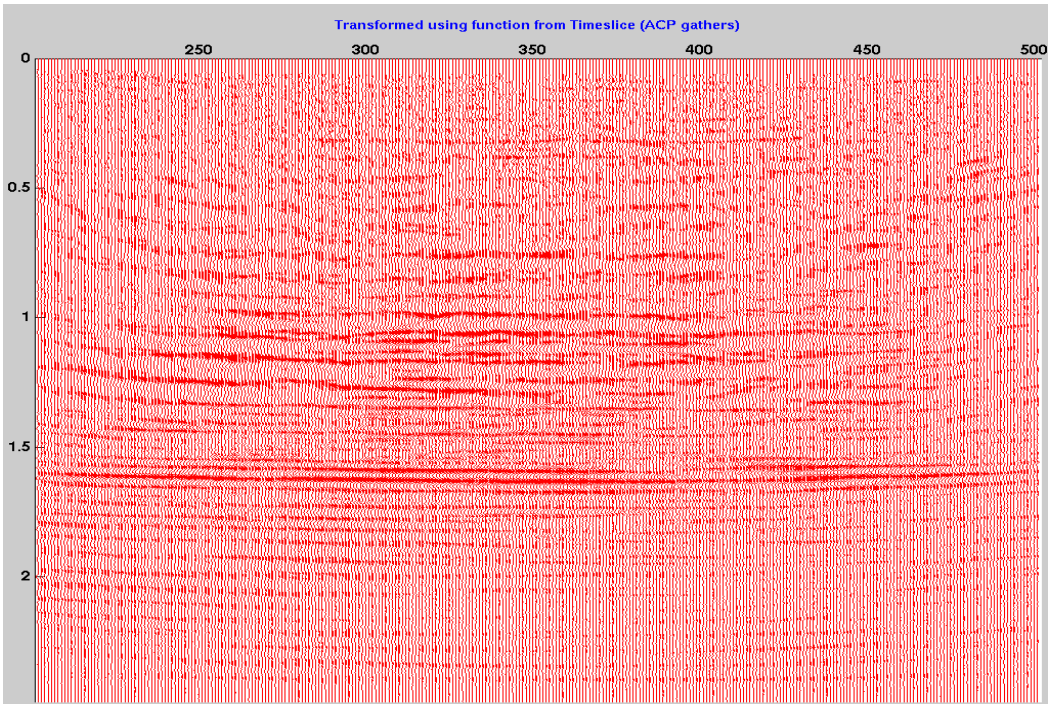

Figure. 3.30. Transformed PS migrated stacked data using γ_0 function from Timeslice.

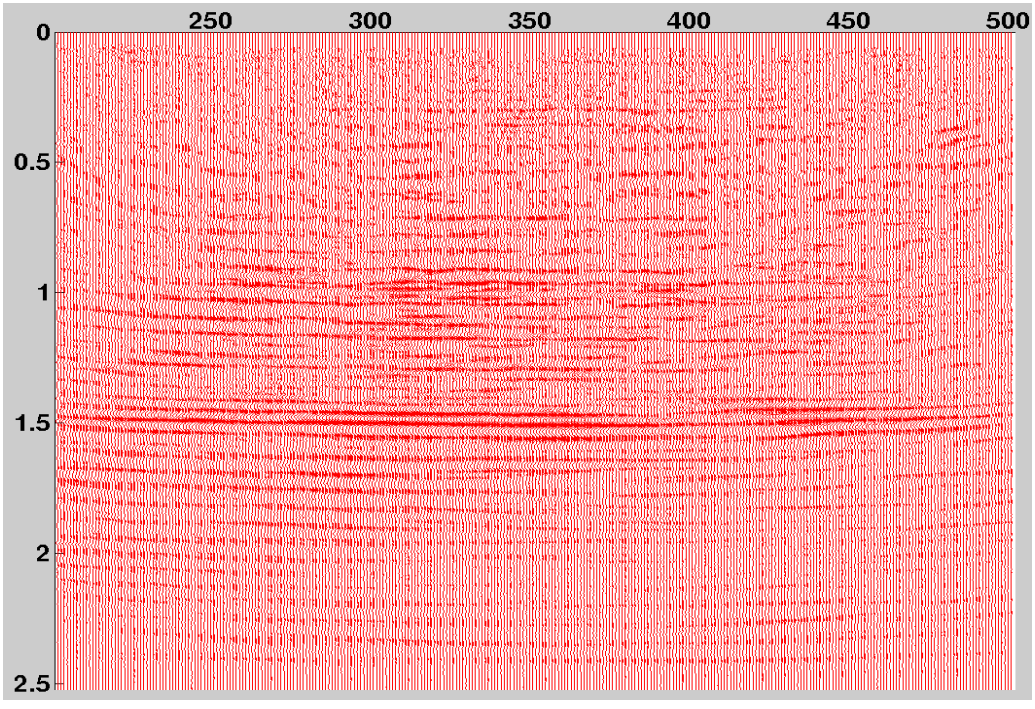

Figure. 3.31. Transformed PS migrated stacked data using γ_0 function from ACP gathers.

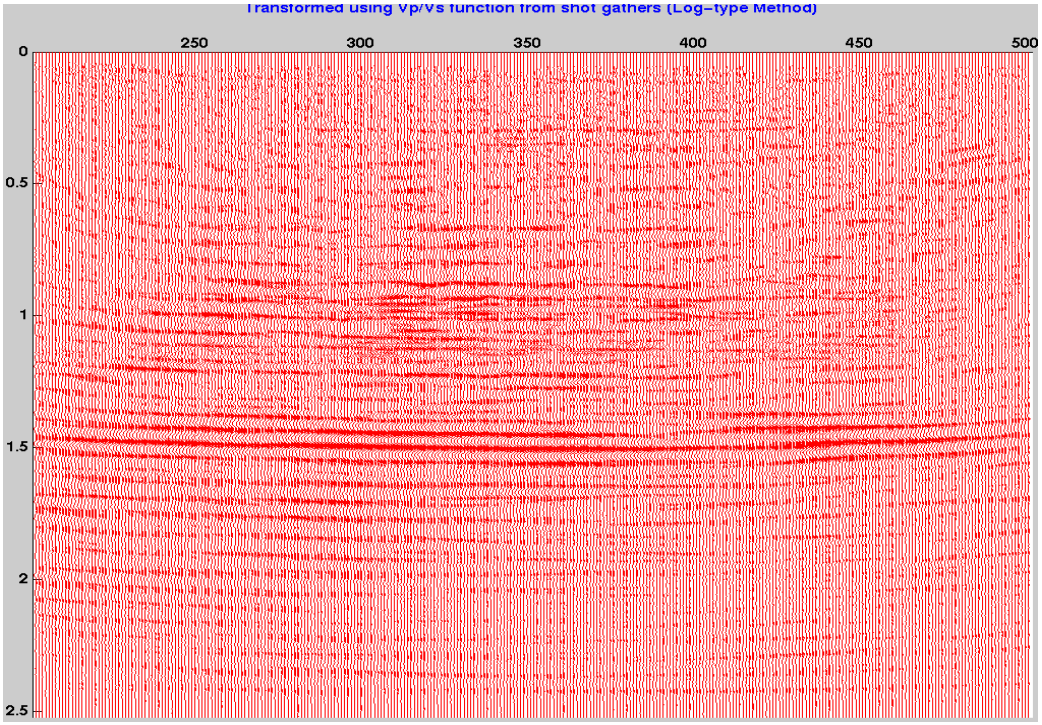

Figure. 3.32. Transformed PS migrated stacked data using γ_0 function from Shot gathers.

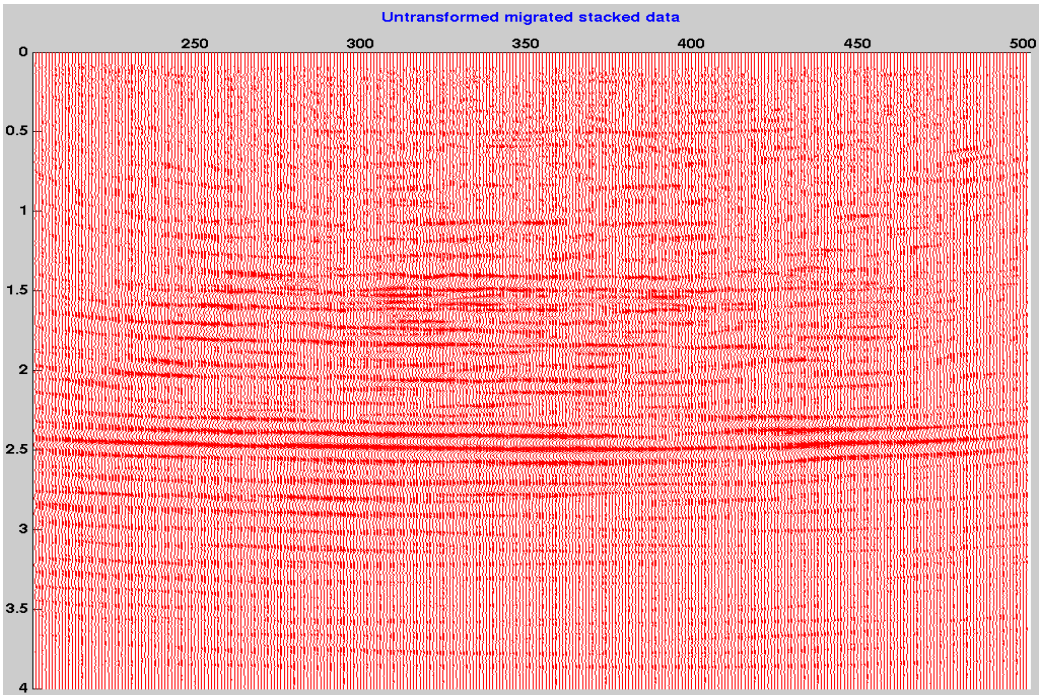

Figure. 3.33. Original PS migrated stacked data from Matlab

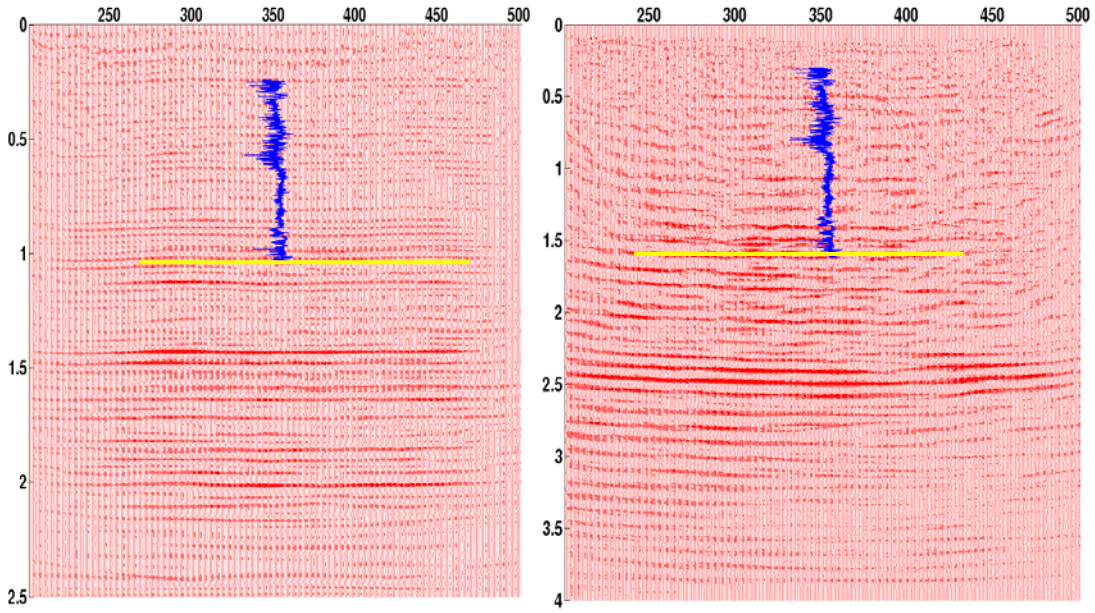

Figure.3.34. PP migrated stacked (left) and PS migrated stacked (right) data sets in their original (raw) times

In 1998, the Crewes Project carried a multicomponent seismic interpretation of the Blackfoot Oil Field; the top of the Viking channel was interpreted to be at about 1.050 seconds P-wave time on the PP stacked section, while it was interpreted to be at about 1.550 seconds PS-wave time on the PS stacked section. These picks are indicated by the yellow lines in Figure 3.34. The seismic events at which the channel top was picked on the PS stacked section will be used as a guide for picking the channel top on the transformed PS sections. Thus the error between the transformed and the P-wave times will be determined.

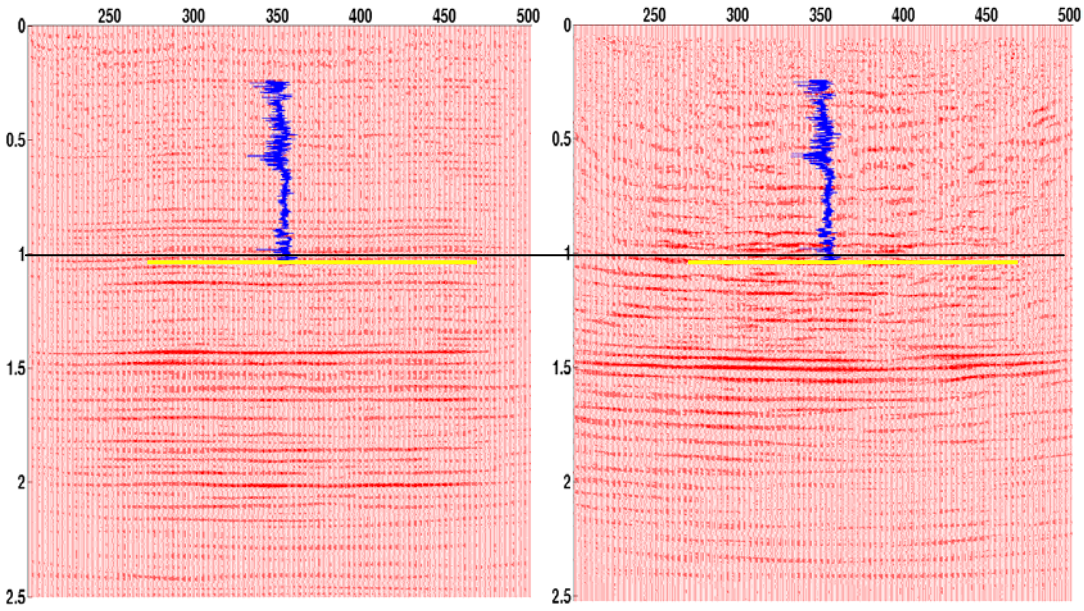

Figure.3.35. PP migrated stacked (left) and Transformed PS migrated stacked (right) data. The PS was transformed using γ_0-function from Log-type Method with ACP gathers.

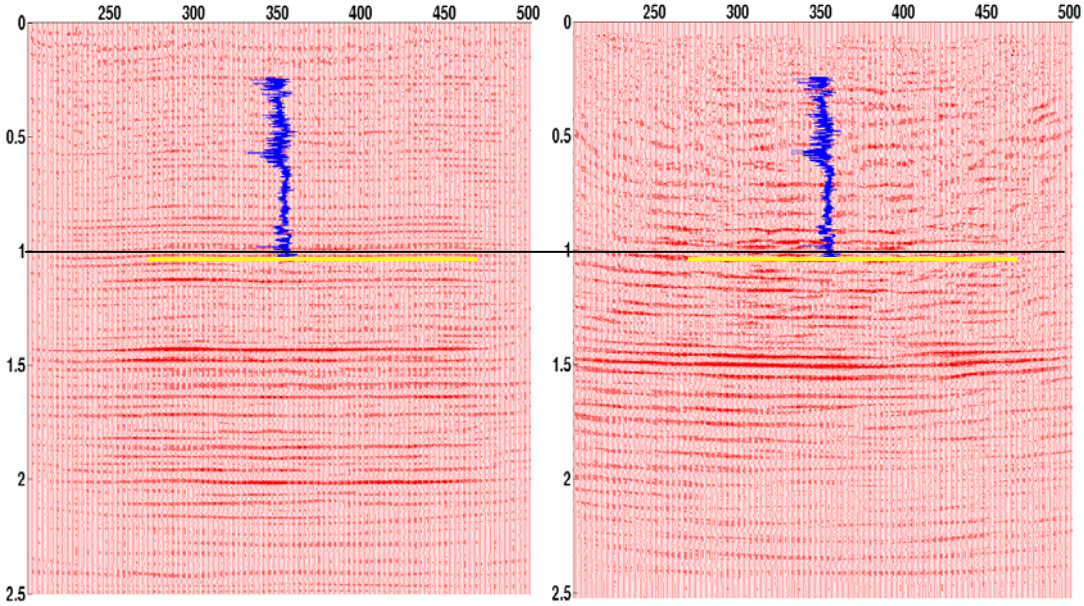

Figure.3.36. PP migrated stacked (left) and Transformed PS migrated stacked (right) data. The PS was transformed using γ_0-function from Log-type Method with Shot gathers.

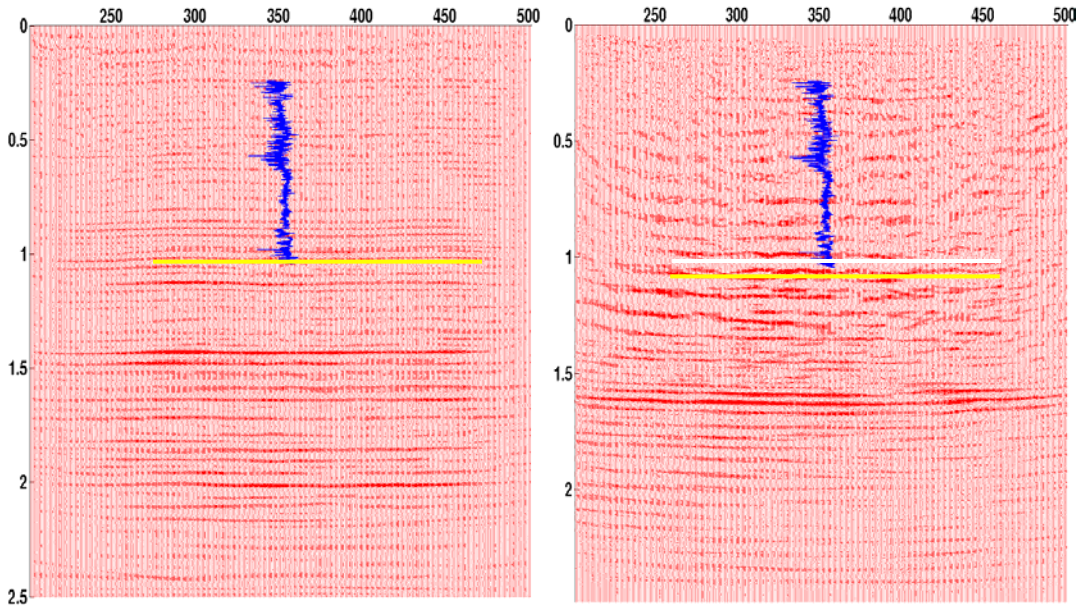

Figure.3.37. PP migrated stacked (left) and Transformed PS migrated stacked (right) data. The PS was transformed using γ_0-function from Timeslice Method with ACP gathers.

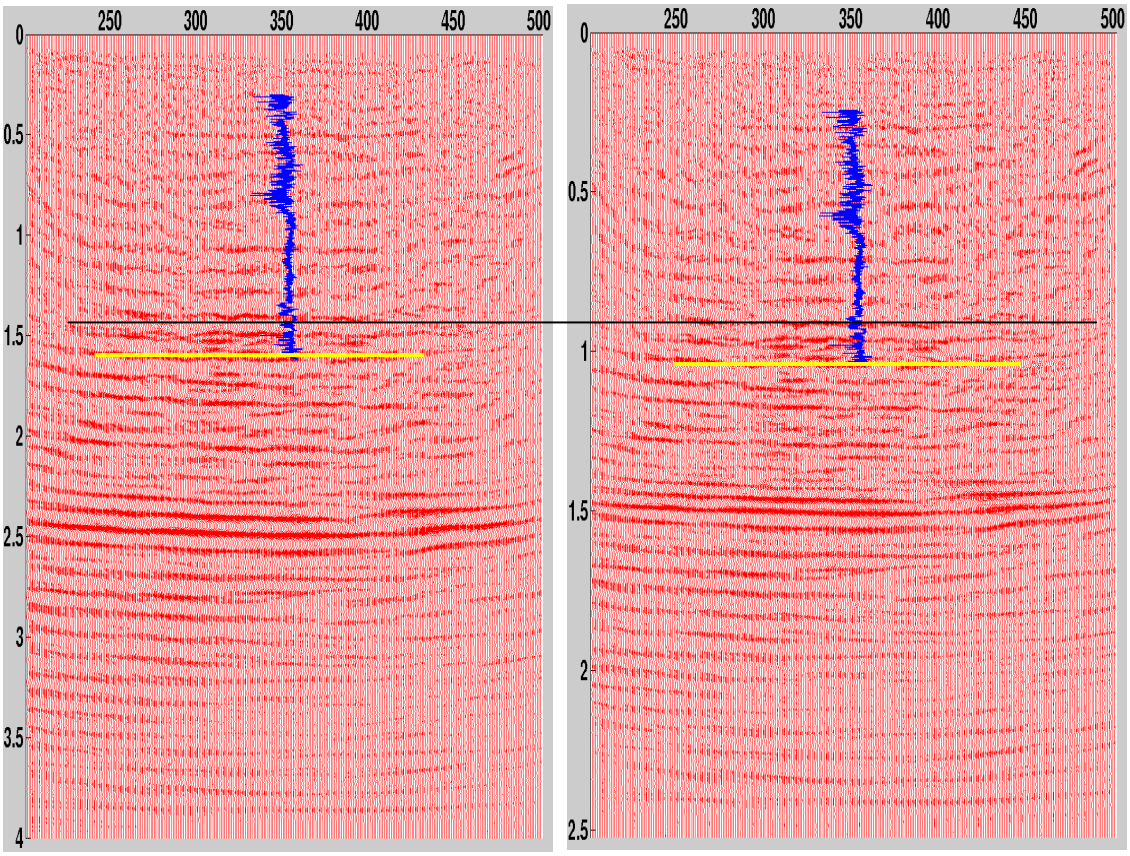

(a) (b)

Figure.3.38. Comparison of the untransformed (a) and the transformed (b) PS migrated stacked sections. The PS data were transformed using V_p/V_s function derived from the Log-type Method. In this figure, the differences between the transformed and the untransformed data are hardly noticeable. The only obvious difference is in the time scale. This signifies the accuracy of the derived V_p/V_s function and the methodology. The error in times between the top of the channel (yellow lines)on the raw PS section and the transformed PS section is about 10 to 15 milliseconds. This translates to a maximum error of about 2%.

3.12 Comparison of PP and PS stacked data sets

From Figures 3.30 to 3.37, it can be seen that the PP and PS stacked data sets appear to be different even though both went through about the same processing sequence. Therefore trying to correlate the two sections visually or otherwise will be an uphill task. Between about 0.9 to 1.050 second PP-time, there is a unique seismic package on the PS section (Figures 3.35 and 3.36). It is characterized by mounded, discontinuous and hummocky seismic facies; which in sequence stratigraphic context, is representative of channel environment and its deposits. Overlying this package is a strong amplitude and continuous seismic facies characteristic of transgressive facies and shales deposition. This interpretation agrees with the geology of the area (See Figures 3.2 and 3.3). On the PP section, a channel cut can be seen at about 1.050 seconds and at CDP location 350. To interpret this section will require the experience of an adept interpreter. From the foregoing, one can see that the PS section can help in delineating environments.

The γ_0-functions derived from the Log-type Method transformed the PS data to 2.520 seconds as against the PP section of 2.5 seconds; the difference being only +20ms. Previous multicomponent seismic interpretation carried out by the Crewes Project showed the top of the channel (the Viking Channel) to be at about 1.050 seconds P-wave time, while the corresponding PS time was picked at 1.550 seconds. These picks are indicated by the yellow lines in Figure 3.34. The seismic event on which the channel top was picked is also shown in the transformed PS sections by yellow lines (Figures 3.35 to 3.36). The difference in time between the channel pick in the transformed sections (using the Log-type Method) and the PP section is about 10 to 15 milliseconds. This translates to an error of less than 2%. In the case of the Timeslice Method, the difference between the

pick of the channel top in the transformed section (white line) and the pick in PP section (yellow line) is about 50 milliseconds (Figure 3.37). This translates to an error of about 5%. Overall the error in transformation is less than 6%.

3.13 Lithology identification using γ_0-log

From Figure 3.39, it can be seen that the low V_p/V_s values correspond to sand-prone interval while the high V_p/V_s values correspond to the shale zones. In Figure 3.40, the sand-prone zone lies between about 0.6 and 1.050 second (PP time). In PS times, this interval lies between about 0.8 and 1.6 seconds (Figure 3.41). The interpreted channel environment falls within the low V_p/V_s values. This sand-prone interval is confirmed by the gamma-ray log (Figures 3.39 to 3.41).

Without prior well information, it is possible to deduce sand-prone zone from the PS seismic section using the scanned V_p/V_s-log (Figure 3.42). The interval of low V_p/V_s values (circled in white) corresponds to the sand-prone zone. This agrees with the gamma-ray log shown to right in Figure 3.42.

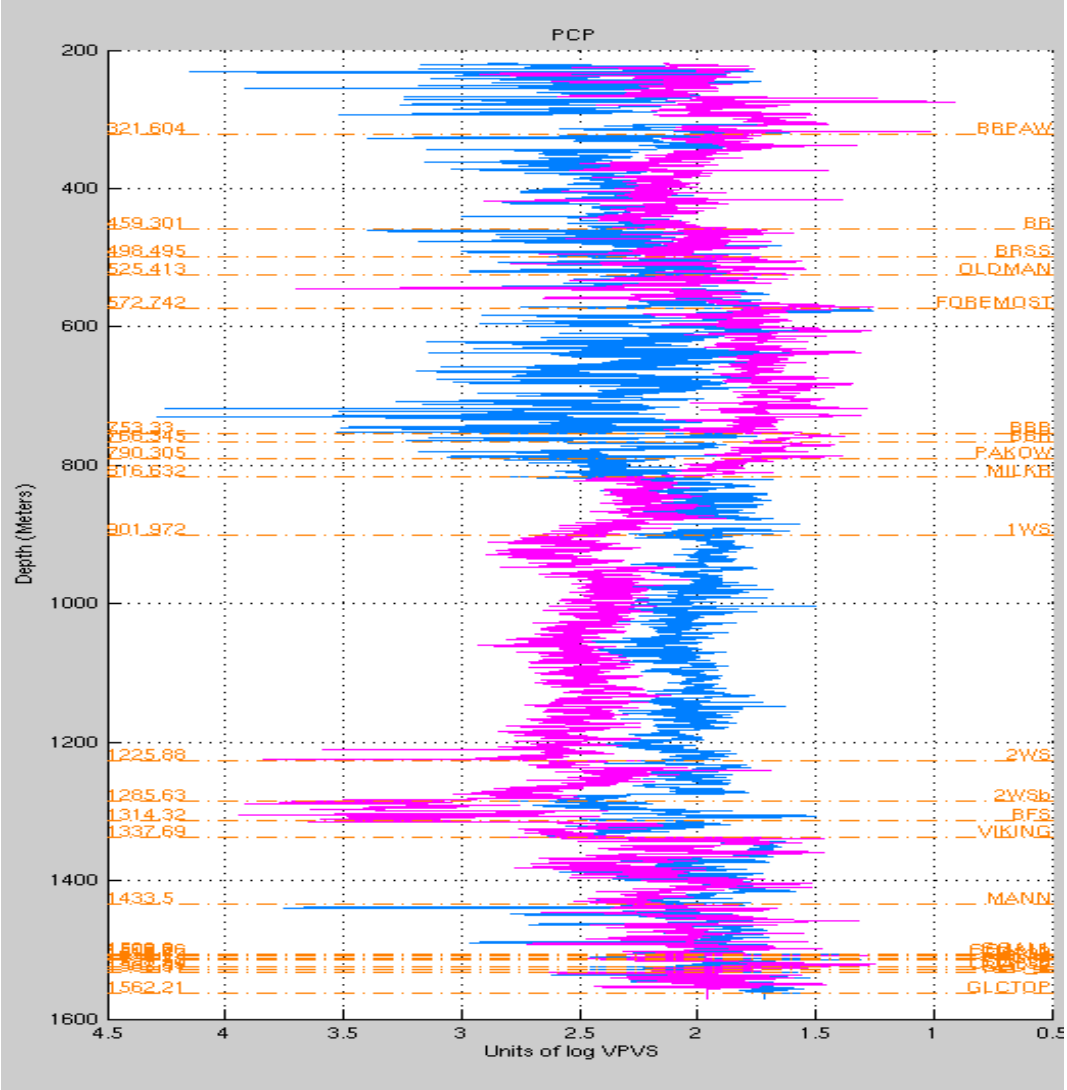

Figure 3.39. Well-09-08 V_p/V_s Log (blue curve) and Gamma-ray Log (purple curve)

The top of sand-prone interval is at about 816.632 m corresponding to the MILKB.

The V_p/V_s values at this depth range from about 2.1 to 1.75

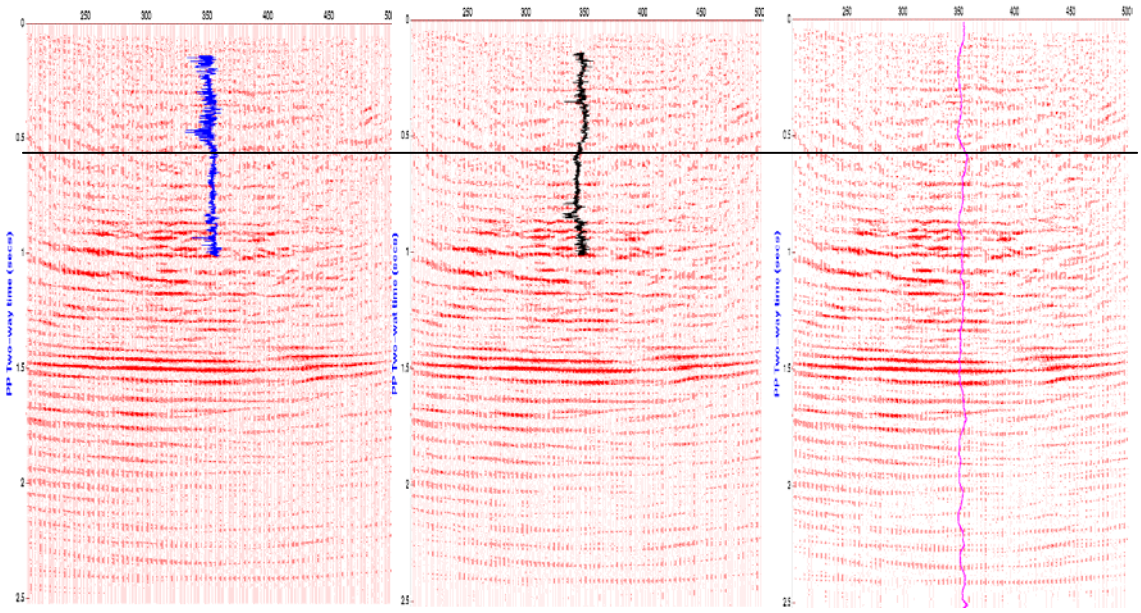

Figure 3.40. V_p/V_s log from Well-09-08 superposed on the transformed PS section (left), Gamma-ray-log from Well-09-08 superposed on the transformed PS section (center), Scanned V_p/V_s-log from the Log-type Method superposed on the transformed PS section (right). Interpretation of the gamma-ray log shows that the sand-prone interval is between about 0.6 and 1.0 This sand-prone zone corresponds to low Vp/Vs values also starting from 0.6 to about 1.0 second.

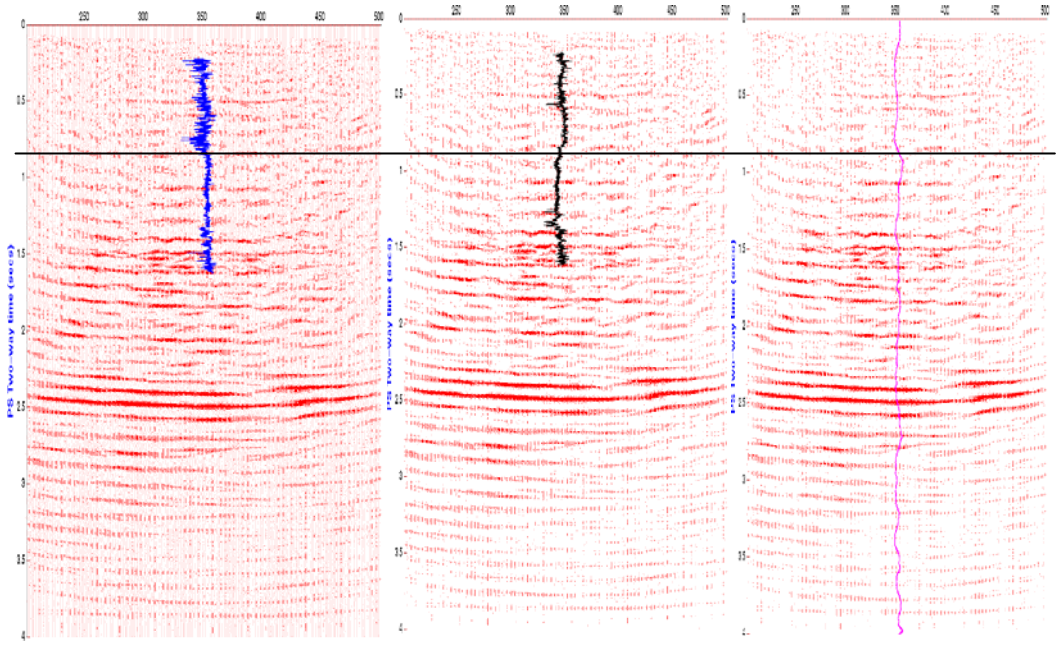

Figure 3.41. V_p/V_s log from Well-09-08 superposed on the untransformed PS section (left), Gamma-ray-log from Well-09-08 superposed on untransformed PS section (center), Scanned V_p/V_s -log from the Log-type Method superposed on untransformed PS section (right). The sand-prone interval is between about 0.8 and 1.6 seconds.

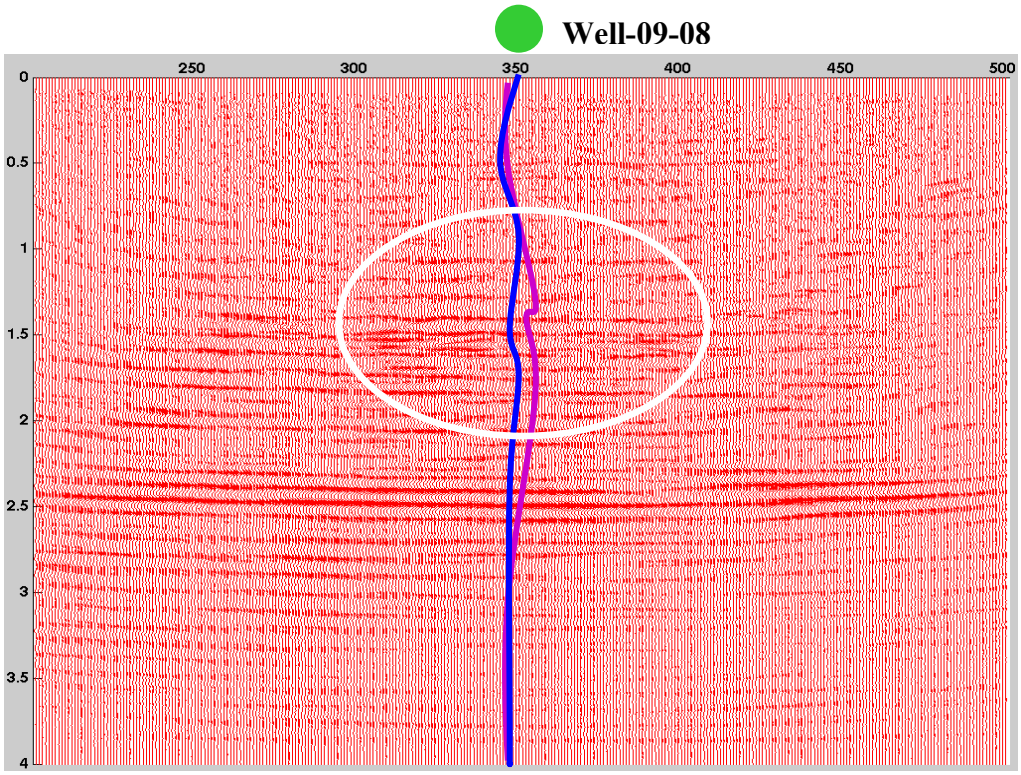

Figure 3.42. Interpreting sand-prone interval using scanned V_p/V_s -log information. The Figure shows the scanned V_p/V_s -function from the Timslice Method (purple curve), while the blue curve is the function from the Log-type Method. The low V_p/V_s values interval circled in white, is interpreted as the sand-prone interval. This agrees with the gamma-ray log which shows the sand-prone interval; also circled in white (Figure 3.43).

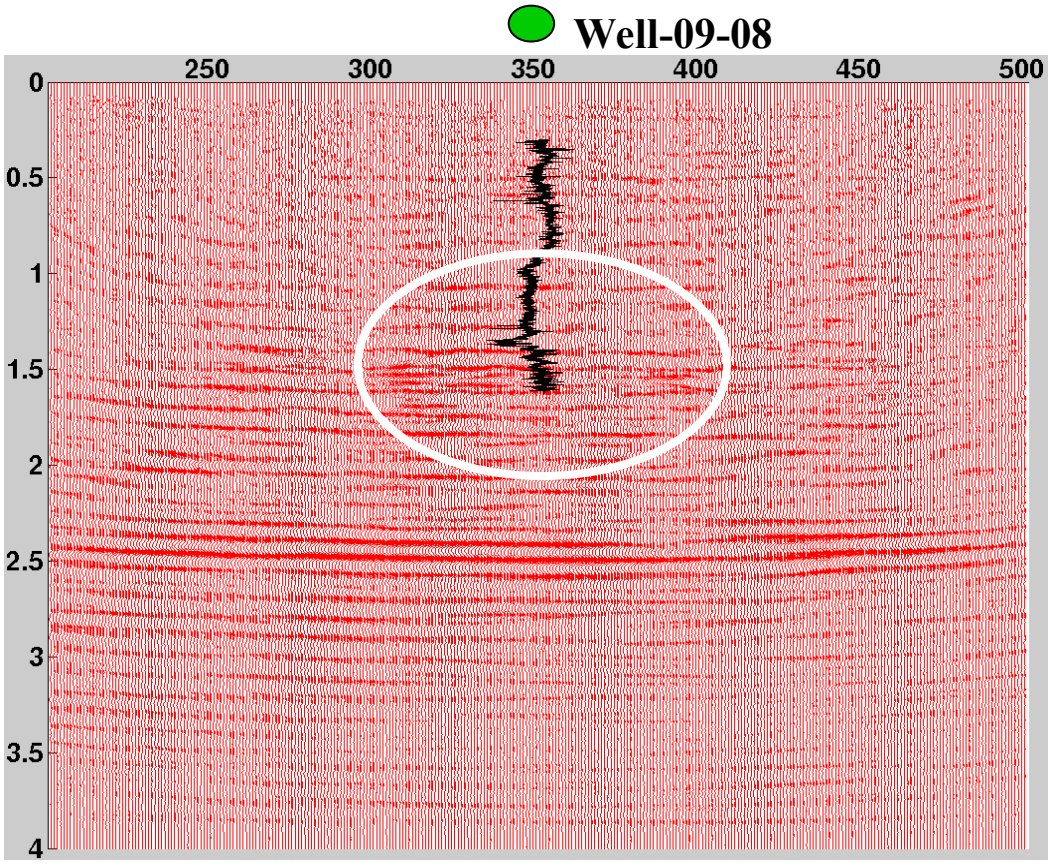

Figure 3.43. Gamma-ray log superposed on the original PS data.

The white-circled interval interpreted as the sand-prone interval.

3.14 Conclusions from Chapter 3.

From the foregoing, it can be seen that the scanned V_p/V_s log using the Log-type Method matched the V_p/V_s log obtained from the Well-09-08 thereby proving the robustness of the methods.

The Log-type Method is faster and more accurate than the Timeslice Method.

V_p/V_s log derived from the Log-type Method needs to be smoothed before using it to transform PS to PP times.

Though the Timeslice Method scans slightly less V_p/V_s values compared to the Log-type Method, results from both methods when used for PS to PP time transformation, gave an error of less than 2% for the Log-Type Method, and 5% for the Timeslice Method.

In applying this scanning technique, either the shot gathers or the ACP gathers can be used as input data.

The PS section gives additional stratigraphic insights as compared to the PP section.

Chapter 4

Discussion, Conclusions and Future work

4.1 Discussion

In Chapter 1, I discussed the many benefits that can be derived from PS exploration and noted that, part of what stands between us and these benefits is the γ_0 (There are many problems yet to resolve with PS data; e.g., acquisition, statics, anisotropy attenuation, etc). Furthermore, I stressed that unless we are able to determine this parameter, these several advantages offered by PS-wave will remain partially unrealized. In this regard, I touched on the fundamentals of PS exploration to elucidate the importance of γ_0.

This discussion was carried on in Chapter 2 where this parameter was formally defined; and I highlighted the various mathematical expressions used to represent it. Briefly, I noted that most VTI parameters depend on this same parameter γ_0, and hence its, crucial role in multicomponent seismic exploration. Because of its strategic role in PS exploration, how to determine it robustly from moveout data became the focus of this chapter. In search of a prestack method to determine γ_0, the PS non-hyperbolic traveltime equation that would facilitate the determination of this parameter via velocity analysis was derived. The equation was validated using a single layer isotropic model, and moveout sensitivity to the variations of γ_0 and stacking velocity in this equation was investigated. I concluded that moveout is more sensitive to stacking velocity variations than γ_0, but that moveout sensitivity to the variations of γ_0 is such that would enable us to determine γ_0 from moveout analysis. Upon this premise, I developed two dual-parameter scanning algorithms which, for want of better names, I christened (a) The Timeslice Method, and (b) The Log-type Method. I tested the two algorithms using single layer and

multi-layer synthetic data sets. Results were found to be accurate within experimental error; the error being less than +/-5%. The Log-type Method is found to be faster than the Timeslice Method and is more accurate. The usage of the Timeslice Method depends on the user's ability to scale the colorbar in order to accentuate maximum semblance location on the velocity-γ_0-plane. On the other hand, the Log-type Method does not require colorbar scaling; the process is automatic. Both methods depend on the velocity and time pairs picked from the velocity semblance panel. Thus, if there is error in picking stacking velocities, then there will be error in the γ_0 output. In this regard, care must be exercised when picking velocity and time pairs. To avoid problems due to multiples, the input data set needs to be appropriately deconvolved. I do not advise full automation of the process at this stage because velocity analysis requires the intervention of the interpreters.

In Chapter 3, these methods were applied to real data sets from the Blackfoot Field in southwestern Alberta. Results from field data demonstrated the robustness of these algorithms. The γ_0-time log derived from these methods matched the well results reasonably well; and when used to transform the PS data to P-wave times, the error is found to be less than 6%. The comparison of the scanned γ_0-log with the Well-09-08 γ_0-log shows that scanned the γ_0-log depends on the location. This implies that scanned γ_0-log at one particular location will apply to that location, but may vary laterally away from it. Despite the good results obtained by these methods, further improvements would be achieved by improving the traveltime equation so as to be able to utilize the far-offsets.

4.2 Conclusions

In conclusion, contrary to earlier opinion, it is possible to determine γ_0 from moveout analysis though with some errors as has been demonstrated in this thesis. Traveltime equation to facilitate this process has been developed; equation is based on the assumption of horizontally layered earth model. Using the derived equation, two dual-parameter scanning algorithms namely the Timeslice and the Log-type Methods have been developed. The accuracy increases with increasingly fine sampling of each variable. The Log-type Method is found to be faster and more accurate than the Timeslice Method. In both methods, the source of error is in picking the stacking velocities and the corresponding times from the velocity semblance display. Currently, the Log-type Method is more automatic though the Timeslice Method can be upgraded to be fully automatic as well. Both Methods need to be upgraded so that velocity-time pairs can be picked interactively at the touch of the cursor. Also, there is need to link all the displays as is currently done in velocity analysis.

In applying the γ_0-time log derived from the Log-type Method to transform PS data to P-wave times, it is necessary to smooth the curve. This can be done by applying a moving average to the curve.

To use the algorithms, it is not necessary to form ACP or CCP gathers. Either the ACP/CCP gathers or the Shot gathers can act as input data; though, using ACP data as input appears to give better results in this case of tested data.

Finally, a prestack method that can automatically scan for γ_0-function has been developed and transformation of PS to P-wave times can be implemented without P-wave information.

4.3 Future work

Improve the algorithms so that V_p/V_s log and stacking velocities can be scanned interactively.

Extend the methods to scan for the effective anisotropic parameter η, by developing PS traveltime equation in anisotropic media. Also, the present equation can be modified by using the exact PS-wave stacking velocity; in this regard, the S-wave stacking velocity term in the equation would have to be substituted for; so as to have a PS-wave traveltime equation that depends on the PS stacking velocity only. This development is already ongoing. Furthermore, I plan to apply the same concepts to search for η-function using the P-wave non-hyperbolic traveltime equation developed by Alkhalifah, and Tsvankin (1994). In addition to the above, subject the algorithms to further tests, by using noisy synthetic shot records and real data sets from complex geologic environments. This will involve dipping beds as well. Results from these tests will prove the robustness or otherwise of the algorithms.

References

Al Chalabi, M., 1974, An analysis of stacking, RMS, average and interval velocities over a horizontally layered ground: Geophys. Prosp., **22**, 458-475

Alford, R. M., 1986, Shear data in the presence of azimuhtal anisotropy: Dilly Texas: 56th Ann. Internat. Mtg., Soc. Expl. Geophys., Expanded Abstracts, 476-479.

Alkhalifah, T. and Tsvankin, I., 1994, Velocity analysis for transversely isotropic media: Geophysics, **60**, 5, 1550-1566.

Anno, P.D., 1987, Two critical aspects of shear-wave analysis: Static solutions and reflection correlations, in Danbom, S.H. and Domenico, S.N., Eds., Shear Wave Exploration: Soc. Expl. Geophys., 48-61.

Banik, N.C., 1984, Velocity anisotropy of shales and depth estimation in the North Sea Basin: Geophysics, **49**, 1411-1419.

Behle, A. and Dohr, G., 1985, Converted waves in exploration seismic, in Seismic Shear Waves, G. Dohr (ed.), 178-220. Handbook of Geophysical Exploration, vol. 15b, Geophysical Press.

Chung, W.Y. and Corrigan, D., 1985, Gathering mode-converted shear waves: a model study: 55th SEG meeting, Washington, Expanded Abstracts, 602-604.

Corbin, R.J., Bell, D.W. and Danbom, S.H., 1987, Shear- and compressional-wave surface and downhole tests in southern Louisiana, in Danbom, S.H. and Domenico, S.N., Eds., Shear Wave Exploration: Soc. Expl. Geophys., 62-75.

Corrigan, D., Justice, J.D. and Neitzel. E.B., 1986, Estimation of shear-wave anisotropy using multicomponent seismic data: 56th Ann. Internat. Mtg., Soc. Expl. Geophysics, Expanded Abstracts, 389-391.

Ensley, R.A., 1984, Comparison of P- and S-wave seismic data: A new method for detecting gas reservoirs: Geophysics, **49**, 1420-1431.

Frasier, C.W. and Winterstein, D.F., 1986, Analysis of conventional and converted mode reflections at Putah Sink, California, using three-component data: 56th SEG meeting, Houston, Expanded Abstracts, 396-400.

Fromm, G., Krey, Th. and Wiest, B., 1985, Static and dynamic corrections. In: Seismic Shear Waves, G. Dohr, (ed.), 191-225, Handbook of Geophysical Exploration, vol. 15a, Geophysical Press.

Gaiser, J.E., 1996, Multicomponent Vp/Vs correlation analysis: Geophysics, **61**, 4, 1137-1149.

Gardner, G.H.F. and Harris, M.H., 1968, Velocity and attenuation of elastic waves in sands: Soc. Prof. Well Log Analysts, 9th Ann. Logging Symp., M1-M19.

Garotta, R., 1985, Observation of shear waves and correlation with P-events. In: Seismic Shear Waves, G. Dohr, (ed.), 1-86, Handbook of Geophysical Exploration, vol. 15b, Geophysical Press.

Garotta, R. 2000, Shear waves from acquisition to interpretation: Distinguished instructor short course, SEG Publications.

Jolly, R.N., 1956, Investigations of shear waves: Geophysics, 21, 905-938.

Kendall, R.R. and Davis, T.L., 1996, The cost of acquiring shear waves: The Leading Edge, **15**, 8, 943-949.

Kristiansen, P., 2000, 4 years experience with 4C seismic: what we have learned: Presented at the SEG/EAGE Summer Research Workshop, Boise, Idaho.

Lash, C.C., 1980, Shear waves, multiple reflections, and converted waves found by a deep vertical wave test (Vertical Seismic Profiling): Geophysics, **45**, 1373-1411.

Li, X. and Yuan, J., 1999, Converted-wave moveout and parameter estimation for transverse isotropy: EAGE, 61st Conference and Technical Exhibition, Helsinki, Finland.

Li, X. and Yuan, J., 2001, Converted-wave imaging in inhomogeneous, anisotropic media: EAGE, 63rd Conference and Technical Exhibition, Amsterdam, The Netherlands.

MacLeod, M.K., Hanson, R.A., Bell, C.R., and McHugo, S., 1999b, The Alba field ocean bottom cable seismic survey: Impact on development, Off. Euro. Conf., Aberdeen, SPE 56977.

McCormack, M.D., Dunbar, J.A. and Sharp, W.W., 1984, A case study of stratigraphic interpretation using shear and compressional seismic data: Geophysics, **49**, 409-520.

McCormack, M.D., Justice, M.G. and Sharp, W.W., 1985, A stratigraphic interpretation of shear and compressional wave seismic data for the Pennsylvanian Morrow formation of southeastern New Mexico: Am. Ass. Petr. Geologists, Memoir 39, Seismic stratigraphy II, An integrated approach, 224-239.

Miller, S., 1996, Multicomponent seismic data interpretation: M.Sc. thesis, University of Calgary.

Nefedkina, T.V., 1980, Detection of transformed reflected PS waves by the CDP method with nonsymmetrical sampling, Soviet Geology and Geophysics, **21**, 93-101.

Neidell, N.S. and Taner, M.T., 1971, Semblance and other coherency measures for multichannel data: Geophysics, **36**, 3, 482-497.

Pardus, Y., Conner, J., Schuler, N., and Tatham, R., 1990, Vp/Vs lithology in carbonate rocks: A case history in the Scipio trend in southern Michigan: 60th Ann. Intert. Mtg., Soc. Expl. Geophys., Expanded Abstracts, 169-172.

Pickett, G.R., 1963, Acoustic character logs and their applications in formation evaluation: J. Petr. Tech., 659-667.

Robertson, J.D. and Pritchett, W.C., 1985, Direct hydrocarbon detection using comparative P-wave and S-wave seismic sections: Geophysics, **50**, 383-393.

Robertson, J.D., 1987, Carbonate porosity from S/P traveltime ratios: Geophysics, **52**, 1346-1354.

Stewart, R.R., Gaiser, J.E., Brown, R.J. and Lawton, D.C., 2003, Converted-wave seismic exploration: Applications: Geophysics, **68**, 1, 40-57.

Tatham, R.H., 1985, Shear wave and lithology: in, G. Dohr, Ed., Seismic shear waves, Part B: Applications: Geophysical Press, 87-133.

Tatham, R.H. and Krug, E.H., 1985, V_p/V_s interpretation: in, A.A. Fitch, Ed., Developments in geophysics-6: Elsevier Appl. Sci. Publ., 139-188.

Taner, M.T. and Koehler, F., 1969, Velocity spectral-digital computer derivation and application of velocity functions: Geophysics, **34**, 6, 859-881.

Tatham, R.H. and McCormack, M.D., 1991, Multicomponent seismology in petroleum exploration: SEG Publications.

Tessmer, G. and Behle, A., 1988, Common reflection point data-stacking technique for converted waves: Geophysical Prospecting, **36**, 671-688.

Thomsen, L., 1999, Converted-wave reflection seismology over inhomogeneous, anisotropic media: Geophysics, **64**, 678-690.

Tsvankin, I. and Thomsen, L., 1994, Nonhyperbolic reflection moveout in anisotropic media: Geophysics, **59**, 1290-1304.

Winterstein, D.F. and Hanten, J.B., 1985, Supercritical reflections observed in P- and S-wave data: Geophysics, **50**, 185-195.

Winterstein, D.F., 1986, Anisotropy effects in P-wave and SH-wave stacking velocities contain information on lithology: Geophysics, **51**, 661-672.

Yang, J. and Lawton, D.C., 2001, Mapping the conversion point in transverse isotropic (VTI) media: CREWES Annual Research Report, **13**, 491-507.

Yilmaz, O., 2001, Seismic data analysis: processing, inversion, and interpretation of seismic data: SEG Publications.

Zhang, Y. and Robinson, E.A., 1992, Stacking P-SV converted wave data with raypath velocity: 62nd Ann. Internat. Mtg., Soc. Expl. Geophys., Explanded Abstracts, 1214-1217.

Appendix

Conversion point determination:

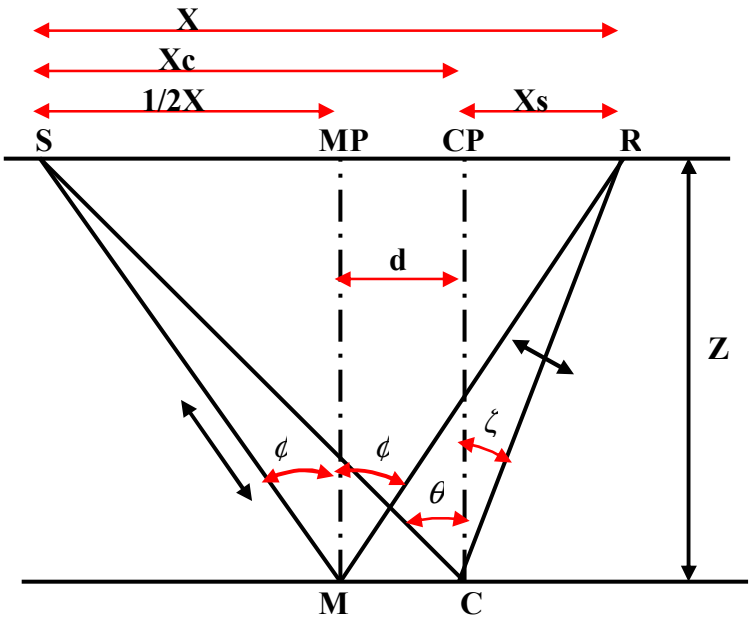

FIGURE A.1

Tessmer and Behle (1988) first derived the expressions for the P-S-wave conversion point and the corresponding traveltimes. Thomsen (1999) provided a Taylor's series expansion and extended it to cover anisotropic and inhomogeneous media. Yilmaz (2001) gave another version of the derivation for the P-S-wave traveltimes. We review here these equations using Figure A1. But first, the annotations used in the Figure are defined.

M = the midpoint depth at which the P-wave is reflected for pure P-mode propagation.

MP = midpoint coordinate between the source S and the receiver R at the surface.

C = the point at which the P-wave is converted to S-wave for PS-wave propagation,

Xc = the conversion point coordinate distance from the source,

Xs = the distance of the conversion point from the receiver R

1/2X = Half the offset distance between the source S and the receiver R,

CP = the conversion point coordinate at the surface,

Z = Depth from surface to the reflector,

X = Source-receiver distance SR,

d = Distance between the conversion point and the common midpoint

ϕ = Incident and reflected angles for pure P-mode propagation,

θ = Incident angle for PS-wave propagation, and

ζ = Angle of reflection for PS-wave propagation.

Having defined the terms used in figure 1, we are now ready to review the derivations.

From Figure A1, we have:

$$Sin\theta = \frac{X_c}{SC} = \frac{X_c}{\sqrt{X_c^{\,2} + Z^2}} \tag{A1}$$

Also,
$$Sin\zeta = \frac{X_s}{CR} = \frac{X_s}{\sqrt{X_s^{\,2} + Z^2}} \tag{A2}$$

Now from Snell's law, we know that for a single layer,

$$\frac{Sin\theta}{V_p} = \frac{Sin\zeta}{V_s} \; ; \tag{A3}$$

where V_p and V_s are respectively the P-wave and S-wave velocities.

Now using (A1) and (A2), in (A3) we have:

$$\frac{X_c}{V_p\sqrt{X_c^{\,2} + Z^2}} = \frac{X_s}{V_s\sqrt{X_S^{\,2} + Z^2}} \tag{A4}$$

Squaring both sides of equation (A4), we obtain:

$$\frac{X_c^{\,2}}{V_p^{\,2}(X_c^{\,2}+Z^2)} = \frac{X_s^{\,2}}{V_s^{\,2}(X_s^{\,2}+Z^2)} \tag{A5}$$

$$\Rightarrow X_s^{\,2}V_p^{\,2}(X_c^{\,2}+Z^2) = X_c^{\,2}V_s^{\,2}(X_s^{\,2}+Z^2)$$

$$\Rightarrow X_s^{\,2}\left[V_p^{\,2}(X_c^{\,2}+Z^2) - X_c^{\,2}V_s^{\,2}\right] = X_c^{\,2}V_s^{\,2}Z^2$$

$$\Rightarrow X_s^{\,2} = \frac{X_c^{\,2}V_s^{\,2}Z^2}{V_p^{\,2}X_c^{\,2} + V_p^{\,2}Z^2 - X_c^{\,2}V_s^{\,2}}$$

$$\Rightarrow X_s^{\,2} = \frac{X_c^{\,2}}{\dfrac{V_p^{\,2}X_c^{\,2}}{Z^2V_s^{\,2}} + \dfrac{V_p^{\,2}Z^2}{V_s^{\,2}Z^2} - \dfrac{V_s^{\,2}X_c^{\,2}}{V_s^{\,2}Z^2}}$$

$$\Rightarrow X_s^{\,2} = \frac{X_c^{\,2}}{\gamma_0^{\,2} + (\gamma_0^{\,2}-1)\dfrac{X_c^{\,2}}{Z^2}} \quad \text{where } \gamma_0 \text{ is velocity ratio } V_p/V_s$$

$$\Rightarrow X_s = \frac{X_c}{\sqrt{\gamma_0^{\,2} + (\gamma_0^{\,2}-1)\dfrac{X_c^{\,2}}{Z^2}}} \tag{A6}$$

Now from Figure A1 we know that:

$$X_s = X - X_c \tag{A7}$$

Using (A7) in (A6) we have:

$$X - X_c = \frac{X_c}{\sqrt{\gamma_0^{\,2} + (\gamma_0^{\,2}-1)\dfrac{X_c^{\,2}}{Z^2}}} \tag{A8}$$

From equation (A8), we can see that:

$$X_c = \frac{\left(\gamma_0^{\,2} + (\gamma_0^{\,2}-1)\dfrac{X_c^{\,2}}{Z^2}\right)^{1/2}}{1 + \left(\gamma_0^{\,2} + (\gamma_0^{\,2}-1)\dfrac{X_c^{\,2}}{Z^2}\right)^{1/2}} X \tag{A9}$$

Equation (A9) is the conversion point CP equation needed to form gathers for velocity analysis and stacking. But it is a complex equation and contains unknown depth Z. To use this equation one needs an iterative process (Yilmaz, 2001). Figure A.2 explains what happens to equation (A9) as the depth Z approaches infinity. With increasing depth Z, X/Z approaches zero so that equation (A9) reduces to (Tessmer and Behle, 1988,):

$$X_c \cong \frac{\gamma_0}{1+\gamma_0} X \qquad \text{(A10)}$$

Equation (A10) is the asymptotic common conversion point expression for performing ACP data gathering for velocity analysis and stacking. In both equations (A9) and (A10), it can be seen that the conversion point depends on the velocity ratio. This dependence is very critical in CCP and ACP gathers formation and stacking.

CCP from CMP

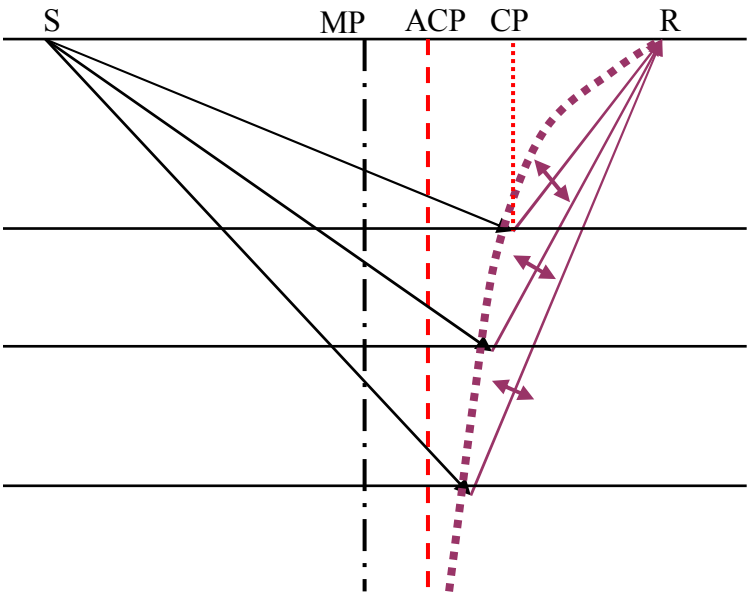

FIGURE A.2

Figure A.2 shows that, as the depth increases, the conversion point follows a curve, which tends towards an asymptotic line. This line intersects the surface at ACP the asymptotic conversion point.

Subtracting the CMP distance from the CCP distance in Figure A1, we have:

$$d = X_c - X/2 \qquad \text{(A11)}$$

Substituting (A10) into (A11), and simplifying we have:

$$d = \frac{(\gamma_0 - 1)}{2(\gamma_0 + 1)} X \qquad \text{(A12)}$$

Equation (A12) indicates the CCP displacement away from the CMP location.

Therefore, if γ_0 = 1, d = 0 (CMP). As γ_0 increases, d = ½, and CCP moves towards the receiver.

Traveltime equation and velocity analysis

From Figure A1, the total time taken for P-wave energy to travel from the source S to the conversion point C, and for the S-wave energy to travel from point C to the receiver R, is given by (Yilmaz, 2001),

$$t_{ps}(x) = \frac{1}{V_p}\sqrt{X_c^{\,2} + Z^2} + \frac{1}{V_s}\sqrt{(X - X_c)^2 + Z^2} \qquad \text{(A13)}$$

where $t_{ps}(X)$ is the P-S-wave total traveltime, and V_s is the shear wave velocity. To obtain the zero-offset, two-way traveltime, set $X = X_c = 0$ in equation (A13). Doing so, we obtain,

$$t_{ps}(X) = t_{ps0} = \frac{Z}{V_p} + \frac{Z}{V_s} = (\frac{V_p + V_s}{V_p V_s})Z \qquad \text{(A14)}$$

$$\Rightarrow Z = t_{ps0}(\frac{V_p V_s}{V_p + V_s}) \qquad \text{(A15)}$$

where t_{c0} is the zero offset two-way traveltime.

Combining (A13) and (A15), we obtain the expression for total traveltime as:

$$t_{ps}(X) = \frac{1}{V_p}\sqrt{X_c^{\,2} + \frac{t_{ps0}^{\,2} V_p^{\,2} V_s^{\,2}}{(V_p + V_s)^2}} + \frac{1}{V_s}\sqrt{(X - X_c)^2 + \frac{t_{ps0}^{\,2} V_p^{\,2} V_s^{\,2}}{(V_p + V_s)^2}} \qquad \text{(A16)}$$

Equation (A16) is the desired non-hyperbolic traveltime expression for performing velocity analysis. Though this equation is for a single layer reflector, it can be used for multi-layer case; in which case, the velocities will be RMS velocities (Yilmaz, 2001). However, it contains the unknown term for the conversion point. Added to this, it does

not contain the velocity ratio γ_0 that controls the point at which conversion takes place. To introduce the velocity ratio into the equation, we do the following:

Divide the numerator and denominator in (A15) by V_s:

$$Z = t_{ps0}\left(\frac{\frac{V_p V_s}{V_s}}{\frac{V_p}{V_s}+\frac{V_s}{V_s}}\right) = \left(\frac{V_p}{\gamma_0+1}\right)t_{pso}$$

$$\Rightarrow Z^2 = \frac{t_{ps0}{}^2 V_p{}^2}{(\gamma_0+1)^2} \qquad \text{(A17)}$$

Using (A17) in (A13), we obtain:

$$t_{ps}(X) = \frac{1}{V_p}\sqrt{X_c{}^2 + \frac{t_{ps0}{}^2 V_p{}^2}{(\gamma_0+1)^2}} + \frac{1}{V_s}\sqrt{(X-X_c)^2 + \frac{t_{ps0}{}^2 V_p{}^2}{(\gamma_0+1)^2}} \qquad \text{(A18)}$$

We can rewrite (A18) as:

$$t_{ps}(x) = \frac{1}{V_p}\sqrt{X_c{}^2 + \frac{t_{ps0}{}^2 V_p{}^2}{(\gamma_0+1)^2}} + \frac{\gamma_0}{V_p}\sqrt{(X-X_c)^2 + \frac{t_{ps0}{}^2 V_p{}^2}{(\gamma_0+1)^2}} \qquad \text{(A18a)}$$

Equation (A18a) is the sort for non-hyperbolic moveout expression to iterate for the velocity ratio during velocity analysis. The derived velocity ratios by this method can then be used for stacking.

By substituting (A10) in (A16), i.e., making use of ACP assumption, we obtain:

$$t_{ps}(X) = \frac{1}{V_p}\sqrt{\left(\frac{\gamma_0}{1+\gamma_0}\right)^2 X^2 + \frac{v_p{}^2 V_s{}^2 t_{ps0}{}^2}{(V_p+V_s)^2}} + \frac{1}{V_s}\sqrt{\frac{X^2}{(1+\gamma_0)^2} + \frac{V_p{}^2 V_s{}^2 t_{ps0}{}^2}{(V_p+V_s)^2}}$$

(A16a)

Similarly, by substituting (A10) in (A18a), we get:

$$t_c(X) = \frac{1}{V_p}\sqrt{(\frac{\gamma_0}{1+\gamma_0})^2 X^2 + \frac{{V_p}^2 {t_{c0}}^2}{(1+\gamma_0)^2}} + \frac{\gamma_0}{V_p}\sqrt{\frac{X^2}{(1+\gamma_0)^2} + \frac{{V_p}^2 {t_{c0}}^2}{(1+\gamma_0)^2}}$$

(A18c)

Equation (16a) has its own merits. If used to perform velocity analysis, semblance can be computed as a volume, which depends on three variables thus: $V = SC(V_p, V_s, t_{ps0})$ or $V = SC(V_p, \gamma_0, t_{ps0})$. If equation (18c) is used in velocity analysis, semblance can only be found as $SC(V_p, \gamma_0, t_{ps0})$. However, in both cases, the stacking velocity for the converted wave cannot be determined from these equations.

Transformation of PS-wave to P-wave section and verse versa

After stacking we need to be able to correlate the P-S-wave stack section to the P-wave stack section. To do this, we need an expression, which ties the sections at their zero offset time. Tessmer and Behle (1988) derived this expression. Consider the case of the P-S-wave in Figure A1. From (A15), depth to the reflector is expressed as:

$$Z = t_{ps0}(V_p V_s / (V_p + V_s)), \qquad \text{(A19)}$$

Also, for the p-wave mode propagation, the depth to the same reflector (Figure 1), can be expressed in terms of the two-way zero offset traveltime as:

$$Z = \frac{V_p t_{p0}}{2} \qquad \text{(A20)}$$

Combining (A19) and (A20), gives:

$$t_{ps0} = \frac{1}{2}(1+\gamma_0) t_{p0} \qquad \text{(A21)}$$

Equation (A21) is the expression we need to transform the P-S-wave stack section to p-wave times. But this can only be applied after correlation has been established.